-

Politecnico di Torino

Politecnico di Torino

Master's degree Program in
Digital Skills for Sustainable Societal Transitions

A.Y. 2023/2024

Graduation Session – July 2024

Application of an automated procedure for Solar Radiation estimation for the City of Turin

A pilot application in a portion of District 6

Supervisor:
Sara Torabi Moghadam

Candidate:
Ali Safaeianpour

Co-Supervisors:
Maria Ferrara
Sebastiano Anselmo

Table of Contents

List of Figures

List of Tables

Acronyms

ASR	Area Solar Radiation
AI	Artificial Intelligence
CM SAF	Climate Monitoring Satellite Application Facility
DHI	Diffuse Horizontal Irradiance
DG	Diffuse to Global radiation
DEM	Digital Elevation Model
DM	Digital Model
DS	Digital Shadow
DSM	Digital Surface Model
DTM	Digital Terrain Model
DT	Digital Twin
DNI	Direct Normal Irradiance
DWD	German Weather Service
EPBD	Energy Performance of Buildings Directive
ESRA	European Solar Radiation Atlas
EU	European Union
GIS	Geographic Information Systems
DWD	German Weather Service
GEBA	Global Energy Balance Archive
GHI	Global Horizontal Irradiation
GHG	Greenhouse Gases
IoT	Internet of Things
T_L	Linke Turbidity
ML	Machine Learning
NCDC	National Climatic Data Center
PV	Photovoltaic
Polito	Polytechnic University of Turin
RES	Renewable Energy Source
SR	Solar Radiation
SoDa	Solar radiation Data
SDG	Sustainable Development Goal
UN	United Nations
UHC	Urban Heat Canyon
UHI	Urban Heat Island

Acknowledgement

I am deeply grateful for the completion of this research project, and I extend my heartfelt gratitude to everyone who has supported and inspired me on this incredible journey. Firstly, I want to express my sincere appreciation to my thesis advisors, Sara Torabi Moghadam, Maria Ferrara, and Sebastiano Anselmo. Their unwavering guidance, patience, and insightful feedback have been instrumental in shaping my research and fostering my academic growth.

I am grateful to the faculty members of the Inter-university Department of Regional & Urban Studies and Planning (DIST) at Politecnico di Torino for their dedication and for opening the doors to the world of digitalization, enriching my understanding of the subject matter and providing me with a solid foundation for my research.

A special thanks to the members of the SDG11 Lab. whose support made it possible for me to undertake this research and pursue my academic goals.

To my family and friends, your constant encouragement and belief in my abilities have been my driving force and a source of strength, especially during challenging times.

Lastly, I want to acknowledge all those who may not be named here but have played a part in my academic journey; your influence, no matter how small, has contributed to my growth and achievements.

Completing this thesis has been both challenging and rewarding, and I am humbled by the collective effort that has made it possible. Thank you all, from the bottom of my heart. I sincerely hope that this work contributes to building a more sustainable future and sparks positive transformations within our field.

Ali Safaeianpour
July 2024

Abstract

Cities represent dynamic symbols of human progress and creativity, continuously shaped by evolving urban planning influenced by technological advancements aimed at enhancing governance efficiency. Embracing digital tools becomes crucial in fostering sustainable urban development. This transformation underscores the synergy between technology and effective management, facilitating the evolution of cities into adaptable, future-ready environments.

Aligned with this transformative vision, this thesis aims to offer valuable insights into advancing urban sustainability through sophisticated simulation techniques, focusing specifically on estimating solar radiation within Turin's urban area focusing on four reference buildings with diverse orientations and characteristics in the district 6. This research contributes to the broader goal of enhancing digital twin applications in the energy sector, illustrating their potential to revolutionize urban planning and environmental management practices.

The study aims to gather reliable inputs data to build a supporting database and estimate solar radiation on an urban scale with GIS-based tools; the precision of GIS-based is assessed by observing variations connected to the input parameters, and the procedure automated using the Graphical Modeler tool in QGIS software. This methodology facilitates achieving research objectives and allows for a comprehensive analysis of the findings.

Evaluation commences by comparing two commonly used GIS tools for solar radiation estimation, followed by gathering data from open-source datasets, including a high-resolution DSM file, monthly Linke turbidity (T_L) factor, monthly Diffuse to Global radiation (DG) ratio values, and global horizontal irradiance (GHI). By organizing these parameters into 28 plans of test, and and evaluating the results, the study highlights the significance of selecting appropriate inputs influenced by geographic and architectural factors.

Utilizing the Graphical Modeler tool in QGIS, the study develops three models for solar radiation estimation using monthly, seasonal, and annual parameters. These models utilize digital elevation models and building-specific information to derive median, maximum, and minimum monthly solar radiation values.

It could be concluded that using aggregated seasonal parameters strikes a balance between efficiency and accuracy in solar radiation estimation, requiring fewer inputs than monthly data while maintaining reasonable precision, with the differences between results obtained from seasonal parameters and monthly data averaging +2.1% in monthly solar irradiation and +0.3% in yearly solar irradiation. This approach supports more effective solar energy production and environmental monitoring in urban contexts.

Chapter 1 - Introduction

1.1 - Problem Statement and Background

In the grand vision of urban development, cities appear as living legacies of humanity's pursuit of progress and efficiency. Within the corridors of urban governance resonate the echoes of technological strides, each innovation a stroke on the vast canvas of local administration. Building upon this foundation, the implementation of digital frameworks becomes imperative for driving sustainable urban development. This mosaic of transformation reveals the fusion of cutting-edge technology and governance as the linchpin driving cities' metamorphosis into agile, adaptable entities. As this narrative of collaboration and ingenuity unfolds, it offers a glimpse into a future where cities transcend mere habitats, becoming thriving ecosystems of innovation and sustainability. In the contemporary landscape of local administrations, integrating technological advancements and digital frameworks is a cornerstone for effective urban governance.

The transformation of cities into smart cities is strongly dependent on the integration of technical, scientific, and digital knowledge inside administrative frameworks. The initial step towards this evolution is to examine the fundamental changes occurring in municipal management, which are motivated by the need to adopt innovative tools and techniques.

With a focus on enhancing city management across diverse domains, from infrastructure maintenance to educational strategies, incorporating tools like the Digital Twin (DT) emerges as a pivotal step. There are many transformative potentials for technological integration within local administrations, illustrating these advancements' broader context and significance in modern urban governance.

Several cities lead the charge toward sustainable development, integrating new technologies for progress. In particular, European cities stand out, embracing innovation and eco-friendly urban planning. They employ digital frameworks and smart solutions to enhance transportation, cut emissions, and prioritize renewable energy. With ambitious sustainability goals and collaborations between administrations, universities, and tech hubs, these cities pioneer resilient, eco-conscious urban landscapes, marking a path toward a sustainable global future.

In order to achieve advanced urban development, the City of Turin began the execution of an urban DT in collaboration with the Polytechnic University of Turin (Polito). This strategic plan is a concentrated and organized effort to use contemporary technological frameworks to create, assess, and improve energy-related strategies within the city's urban landscape. It represents a significant advancement towards achieving sustainable urban growth. The main goals are to cultivate a culture that embraces cutting-edge digital and information technology, with specific focuses on energy efficiency, sustainable transportation, urban planning, creative infrastructure, and the broader imperatives of ecological and digital transformation. The DT, a thorough 3D digital model created by Polito, is the central component of this collaborative project. Its purpose is to provide guidance for various efforts, such as intricate maintenance plans and strategic updates to the city's master plan. Through this partnership, a connection is established between the local government and the academic community, allowing them to integrate their resources and ambitions to work towards a common objective. There is an opportunity for this partnership to have significant effects on both the regional and national levels.

Understanding the reasons behind this initiative provides further insight into its strategic importance and potential impact.

As stated by Leopold et al. [1], the DT simplifies scenario modelling, incorporates open-source tools for assessing energy transitions, promotes the adoption of renewable energy sources (RES), and offers seamless support to stakeholders in urban planning. The motivations for implementing the DT in Turin are multifaceted and align with broader energy and sustainability goals. The strategic importance of the energy sector, one of the major DT themes for the City, is due to the current global scenario. The worldwide energy consumption is experiencing a significant increase caused by the rapid growth of the economy. Considering the current rate of urbanization, it is undeniable that cities have a significant impact on the rise in energy consumption, affecting both the global and national levels in Europe. Various European Union regulations [2, 3, 4, 5] encourage member states to implement policies that enhance building energy efficiency and promote the development of RESs. These policies aim to transform national energy systems towards greater environmental friendliness and sustainability.

Recently, geopolitical conflicts and the problems posed by the COVID-19 pandemic have altered the worldwide energy supply networks, resulting in significant difficulties in supplying the growing global energy demand [6]. In light of the energy issues that countries are confronting, each member state of the European Union needs to establish its own strategy to achieve renewable energy objectives. This underscores the crucial importance of local initiatives in transitioning to RESs, necessitating assistance for cities to evaluate their energy strategies to align with broader sustainability objectives [7].

With initiatives like the European Green Deal [3] and the REPowerEU plan [8], the EU has led in the direction of the region's shift toward clean energy and renders solar energy a pivotal contributor to shielding consumers from unpredictable energy price fluctuations. In May 2022, the Commission introduced the EU solar energy strategy [9] as a part of a comprehensive approach aimed at targeting existing barriers in the industry and devising a roadmap for surmounting them. The strategy aims for over 320 gigawatts (GW) of solar photovoltaic (PV) capacity by 2025 and approximately 600 GW by 2030, introducing amendments to the Renewable Energy Directive (EU/2023/2413) [10] and measures facilitating the authorization of renewable energy projects, promising to expedite the EU's embrace and assimilation of solar energy.

Recent European legislation, such as the Renewable Energy Directive (RED) [11], which was recast in 2023 as part of the Green Deal and the 'Fit for 55' package, introduces new directives aimed at achieving climate neutrality by 2050; and exemplifies the continent's dedication to promoting renewable energy adoption and reducing dependency on fossil fuels [12]. Formulated within the broader legislative framework, directives like the RED seek to harmonize regional policies with global sustainability objectives articulated in initiatives like the European Green Deal [13]. The RED mandates the development of supportive mechanisms at both local and national levels to facilitate the integration of renewable energy sources into the energy matrix [12]. This directive, alongside others like the Energy Performance of Buildings Directive (EPBD), holds significance in reshaping the energy landscape, with a specific emphasis on fostering the utilization of renewable energy in urban settings [14].

The 20-20-20 Program [15] targeted a 20% cut in greenhouse gas (GHG) emissions, a 20% surge in renewable energy, and a 20% progress in energy efficiency by 2020, and the EU's 2030 Climate Targets Plans sought a 55% reduction of GHG [16].

These commitments significantly align with SDG 7 - Affordable and Clean Energy - one of the 17 Sustainable Development Goals (SDGs) set in the United Nations (UN) Agenda 2030 [17]. Furthermore, they interlink seamlessly with SDG 11 – Sustainable Cities and Communities – and numerous other goals; for instance, SDG 13 – Climate Action – specifically indicator 13.2.2, underscores the crucial need to reduce GHG emissions, emphasizing their pivotal role in achieving decarbonization. Reforms to the Renewable Energy Directives and supportive measures for renewable energy projects promise to expedite the EU's adoption of solar energy, contributing to the global goal

of ensuring access to affordable and clean energy for all. The City of Turin's efforts are a practical manifestation of these broader policies, reflecting local implementation of global and regional initiatives.

Turin's implementation of the DT is a significant example of local action contributing to national and EU energy goals. Italy has seen a rapid rise in renewable energy over the last decade, propelled by governmental policies, EU initiatives, and substantial public and private investments despite facing a slower rate than neighbouring countries [18]. This country has concentrated on creating infrastructure to support sustainable clean generation, aiming for carbon neutrality by 2050, yet enduring path dependency in the energy system poses substantial barriers, impacting sustainable policy responses [19]. Additionally, Italy's geographical position offers a chance for energy self-sufficiency by improving infrastructure and embracing new methods [20].

While Italy grapples with its energy policy goals, Turin's initiative aligns with international policies for renewable energy and sustainable urban development, aligning local action with global and European initiatives. Turin reflects Italy's dedication to sustainability and achieving energy policy goals by 2050 in taking steps forward. In this framework, Turin is also part of a set of ten thousand cities which signed the EU Covenant of Mayors for Climate and Energy [21], targeting climate neutrality by 2030. Exploring Turin's role in Italy's energy progress will provide insights into overcoming significant challenges in the system. In order to improve Turin's energy assessment and planning policies, a part of District 6 is selected as a study area to present a pilot application as a precursor to city-wide implementation. This initiative aims to pave the way for broader policy integration and enhancement across Turin. The study area, corresponding to the Barriera di Milano district, shows manifestations of social distress and physical degradation. The study area, corresponding to the *Barriera di Milano* district, shows manifestations of social distress and physical degradation. This area, which includes various types of buildings and historical ties to industry (such as an abandoned railway branch), faced challenges due to the increased demand for housing after the war, as there wasn't sufficient construction to meet this need. Despite industrial decay and attempts at revitalization, remnants of historic structures have been preserved for cultural heritage. The complexity of this area comes from the combination of residential and industrial spaces and forms a distinct urban structure defined by functional diversity. The impact of past renovations and ongoing regeneration efforts affects its physical and social fabric, creating a unique but marginal urban space characterized by diverse functional areas and historical remains. Moreover, fostering community engagement and awareness programs in these areas can vitalize public participation and support for sustainable energy initiatives.

While the strategic integration of PV systems into urban environments is widely recognized as instrumental in advancing the global shift towards sustainable energy, given the advantageous proximity of building rooftops to energy consumption hubs and the spatial constraints inherent in urban landscapes [22], Geographic Information Systems (GIS) can serve as a helpful tool for optimizing PV system placements, and play a pivotal role in advancing the efficacy of simulation and modelling tools for distributed energy systems. GIS is defined by the Environmental Systems Research Institute (ESRI) as a comprehensive collection of computer hardware, software, humans, and geographic data that is purposefully designed to effectively capture, store, update, modify, analyze, and display any data that is geographically related [23].

GIS is a framework that enables spatial analysis, mapping, and visualization of energy infrastructure and facilitates the precision required for simulations and modelling. Moreover, GIS can contribute to analyzing energy infrastructure, enabling precise simulations for RES in specific regions. Incorporating data on population, buildings, energy resources, and sensors facilitates accurate planning for electricity generation. Moreover, the creation of thematic maps using GIS helps with data visualization, which in

turn facilitates better decision-making by utilizing easily accessible geographic data. By incorporating Geographic Information System (GIS) technology, urban planners and policymakers can improve their study of energy infrastructure and demonstrate the wider impact that technology has on the formation of resilient and sustainable urban landscapes.

1.2 - Research Questions

This thesis investigates urban PV potential evaluation, focusing on precise input parameters, tool assessment, and automation. The ultimate goal is to enhance understanding, accelerate the processes, and promote solar energy integration in Turin's urban environment.
Within the context of solar energy in Turin, two essential aspects come into play. First, accurately assessing PV energy potential relies on weather, topography, and system features. These elements, incorporating meteorological and geographical data alongside technical specifics, inform how solar energy integrates into the city's construction. In addition, the use of GIS techniques provides an opportunity to gain essential insights into the evaluation of Turin's urban PV potential. This investigation achieves a better understanding of the interdependence and sensitivity of the various tool settings and configurations. This understanding paves the way for enhancing assessment methods, thereby enhancing the precision of evaluations in urban settings. In order to advance the endeavour towards comprehensive solar energy integration in Turin's urban landscape, this thesis is going to address these crucial questions concerning computational parameters and process automation:

Question 1. What is the impact of weather, geography and geometry parameters on the accuracy of GIS-based solar radiation estimation in complex urban settings?

Question 2. How does integrating the automation of solar radiation estimation in PV potential evaluation as part of DT enhance process efficiency and boost accuracy levels?

1.3 - Objectives

Various methods have been proposed using GIS to integrate and evaluate PV systems in urban contexts, and applied to various research areas and spatiotemporal resolutions [24, 25, 26, 27].
The main objective of this thesis is to measure and analyze precisely and accurately the potential of PV energy production in Turin's urban environment, thus determining the capacity and ability to integrate PV systems into the city's infrastructure and built environment.

1.3.1 - Goal I – Parameters Accuracy

The primary purpose of the thesis is to have the correct parameters so as to ensure that the calculation of the solar radiation is appropriately carried out in assessing urban solar radiation for PV potential in Turin. This process involves meticulously selecting factors like atmospheric conditions, geographic characteristics, and specific technological aspects essential for solar radiation estimation for solar irradiation in the PV systems. Achieving accurate parameterization entails relying on various data sources such as meteorological records, geographic information, and system specifications for thorough calibration. Integrating these parameters aims to enhance the accuracy and reliability of subsequent analyses significantly. This foundational step provides a robust framework for precisely evaluating urban PV potential and facilitating informed decision-making processes in this domain.

1.3.2 - Goal II – Tools Precision

The subsequent goal involves evaluating tools precision to clarify how variations in settings and properties, influenced by different inputs, affect outcomes in solar radiation estimation for PV potential assessments. This task entails systematically examining differing processes and configurations employed in the evaluation process, aiming to discern the slight effects of altering settings, parameters, and input variables. By comprehensively exploring these variations, this aspect of the study attempts to demonstrate the multifaceted consequence of diverse configurations on the outcomes of solar radiation estimation in PV potential assessments. This analysis contributes to a deeper understanding of the sensitivity and dependencies inherent in the tools and configurations, enriching the methodologies for accurate and robust evaluation of solar radiation for PV potentials in urban environments.

1.3.3 - Goal III – Automation

The final objective of the thesis is to automate this assessment procedure through computer programming, utilizing Python-based algorithms and workflows to streamline and expedite the assessment of solar radiation in PV potential. Integrating these computational techniques allows AI and ML algorithms to enhance predictive capabilities, enabling the anticipation of potential outcomes based on varied parameters and scenarios. Furthermore, this automation endeavor recognizes the seamless connection between computer programming, particularly Python, and tools within software. This linkage aims to facilitate a more efficient and integrated workflow, enabling the utilization of Python's programming capabilities alongside the functionalities present in software for enhanced analysis and predictive modeling in assessing solar radiation in PV potential within urban landscapes.

1.4 - Thesis Structure

The thesis structure unfolds comprehensively, commencing with:
After the introduction, the literature review delves into existing research, elucidating various perspectives and findings relevant to the field, focusing on the numerous viewpoints and discoveries that are associated with digital twins, particularly in PV systems, as well as the various factors that are used in solar radiation models.
In the third section, the methodology of the study is broken down in detail, with an emphasis placed on the utilization of the case study approach in the estimation process. Sections within the methodology chapter provide an overview of the procedures that were followed in order to carry out the research, addressing both the research questions and the objectives.
The results are described in the following chapter, which is broken up into subsections that examine the theoretical obtained results, the instruments that were utilized in the assessment, and the outcomes that are obtained using the study approach. In this chapter, a critical assessment of the findings is presented, with a connection made between those findings and the aims of the study as well as the theoretical framework.
The findings are summarized and critically analyzed in the Conclusions chapter, which also provides a summary of the findings. The purpose of this part is to investigate how the findings correspond to the primary research challenge and to make suggestions for possible directions that future study could go. It presents a full conclusion to the research and analysis that was conducted during the study, indicating chances for additional development and improvements in the past and future.
Lastly, the References chapter provides a list of all sources cited and consulted throughout the study, ensuring transparency and scholarly rigor in the research process.

Chapter 2 - Literature Review

The notion of energetic transition is based on the concept of sustainable development, described in the Brundtland report [28], following major energy and environmental disasters in the 1970s and 1980s, including the oil crisis and the Chernobyl disaster. Sustainable development is defined as «development that meets the needs of the present generation without compromising the ability of future generations to meet their own needs» [28].

This paradigm evolved through UN frameworks such as the Kyoto Protocol in 1997 and the Rio de Janeiro Conference in 1992, aiming to reduce polluting emissions caused by human activities and establish global standards for environmental protection. These global frameworks laid the groundwork for renewable energy strategies. The development of renewable energy strategies is influenced by various aspects, including technological innovation and international cooperation [29].

Several studies [30, 31, 32, 33, 34] establish a bidirectional relationship between technological innovation and renewable energy, emphasizing technology's significant impact on renewable energy consumption. This notion is further supported by other research, highlighting the critical role of renewable energy in future electricity generation and addressing environmental challenges during the ongoing energy transition [35, 36].

Once broad frameworks for energy transition and renewable solutions have been established, it is crucial to explore particular applications in sustainable urban development. An essential aspect of this transition involves integrating PV technology into the urban environment. Assessing PV potential faces numerous challenges due to existing barriers, including architectural restrictions, visibility assessment, and computational demands [22].Evaluating urban-scale PV potential requires considering factors like high temporal-resolution simulations and the solar energy potential of rooftops to accurately estimate overall PV potential [37]. Moreover, beyond fluctuating meteorological conditions, different building types, complex urban structures, and barriers to incident sunlight in metropolitan areas all contribute to limiting the potential of PV systems [38, 39].

In line with these efforts, while numerous studies have been conducted to quantify the PV potential of buildings and enhance solar evaluation through the development of software and algorithms, the full release of 3D city models into the public domain remains pending [39]. Quantification of energy demand and renewable generation for a vast array of buildings is made possible through the combination of 3D city models and simulation functionalities [40].

In assessing solar radiation availability for PV potential in a city context, the integration of GIS technologies with numerical radiation methodologies can be beneficial. This combination enables a more precise simulation of topography and building structures, facilitating the accurate prediction of solar radiation patterns, although achieving detailed findings necessitates balancing computation time and accuracy, particularly concerning spatial and temporal resolutions [38]. In the broader energy transition framework, solar radiation emerges as a critical element in calculating PV potential; a study by Anselmo and Ferrara [41] highlights diverse methods for estimating solar energy, primarily utilizing tools like ArcGIS and QGIS. These methods heavily rely on weather data input. However, despite the accuracy of the formula used for determining PV potential, there is a need for comprehensive validation of the input parameters. This gap in validation underscores the importance of shifting towards advanced 3D models that consider temporal variations for more accurate estimation. This synthesis integrates findings from previous research while emphasizing the ongoing evolution in solar energy estimation methodologies, underscoring the importance of rigorous validation and the adoption of advanced

modelling techniques to accurately assess PV potential and facilitate informed decisions in urban energy planning.

2.1 - Digital Twins

In the age of advanced technology, Digital Twins have transformed how digital and physical worlds interact. This evolution, driven by digitization, seamlessly integrates modern energy systems with virtual models, data, and their real-world applications.

As mentioned by Negri et al. [42], despite the term Digital Twins being used increasingly in business and research ventures, there is a conspicuous lack of a generally accepted description for the notion in the scientific literature. Additionally, they presented several definitions of Digital Twins available in scholarly sources [42]. While debates surround the exact terminology (Figure 1), a common thread unites these definitions. In general, Digital Twins can be defined as sophisticated, technology-driven three-dimensional representations of physical objects or systems. These representations integrate multi-physics and multi-scale simulations with real-time data and historical information. These complex models make it possible to carry out predictive analysis, which implies that they can anticipate future states or behaviours in reality that represent them [43, 44, 45].

Figure 1 - The Digital Twins definitions word group cloud [46]

Three primary elements make up the Digital Twins idea [47]:1) A real-world physical object, 2) A virtual object in the digital space, and 3) A collection of links between the digital and the real world. The idea of digital twins covers every stage of a system's lifecycle, indicating that it can be applied in many different ways. During the design phase, activities such as optimization, produce and receive data, and virtual evaluation are prominent; in the operational phase, the focus shifts towards monitoring,

production control, process forecasting, and optimization, alongside planning activities; and finally, in the maintenance phase, applications extend to predictive maintenance, fault detection and diagnosis, as well as virtual testing procedures [46].

By means of data and advanced models, Digital Twins can be helpful in monitoring, simulating, predicting, optimizing, and performing various tasks in a system; additionally, the core of Digital Twins functionality lies in its accurate representation of real-world objects, enabling it to deliver specific services and meet application needs effectively [48].

Based on the level of data integration from both the digital and real worlds (Figure 2), different levels of a digital twin are mentioned by Jeddoub et al. [49]:

- Digital model (DM): a simple abstraction of a physical object requiring manual updates in both directions.
- Digital shadow (DS): refers to system that allows automatic data flow from the physical object to the digital copy but requires manual updates from the digital to the physical.
- Digital twin (DT): a system that enables automatic data updates in both directions without human intervention, facilitated by artificial intelligence and actuators.

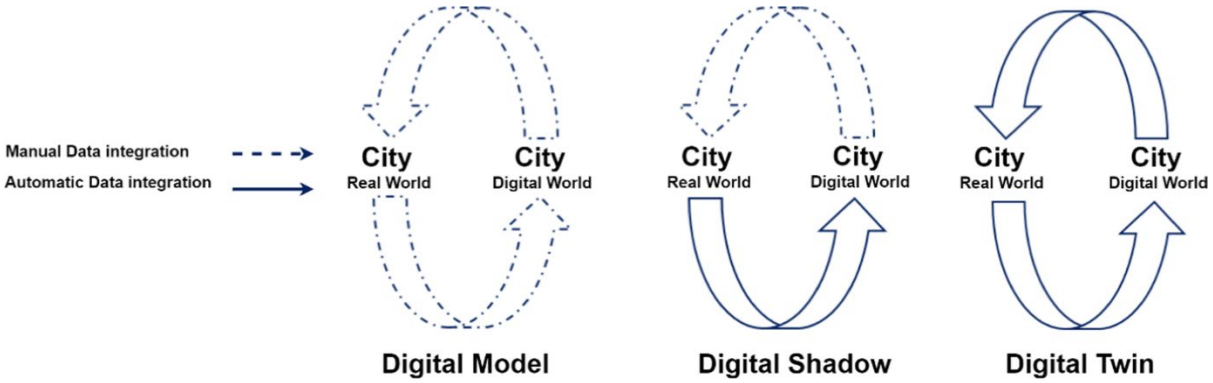

Figure 2 - Digital Twin concept: Stages of maturity based on data integration levels [49]

It is critical to comprehend the differences between Digital Twins and existing technologies. The Table 1 shows how Digital Twins differentiate themselves by seamlessly integrating big data, cybersecurity, machine learning, and other technologies with their necessary Internet of Things (IoT) counterparts [44].

Table 1 - How Digital Twins varies from current technology [44]

Technology	How the technology differs from DT
Simulation	No real-time twinning
Machine Learning	No twinning
Digital Prototype	No IoT components necessarily
Optimization	No simulation and real-time tests
Autonomous Systems	No self-learning (learning from its past outcomes) necessarily
Agent-based modelling	No real-time twinning

The virtual model's parameters and dynamics are continuously refined, ensuring an accurate representation of the actual entities being modelled using real-time data from the physical system [47, 50]. This process is depicted in Figure 3.

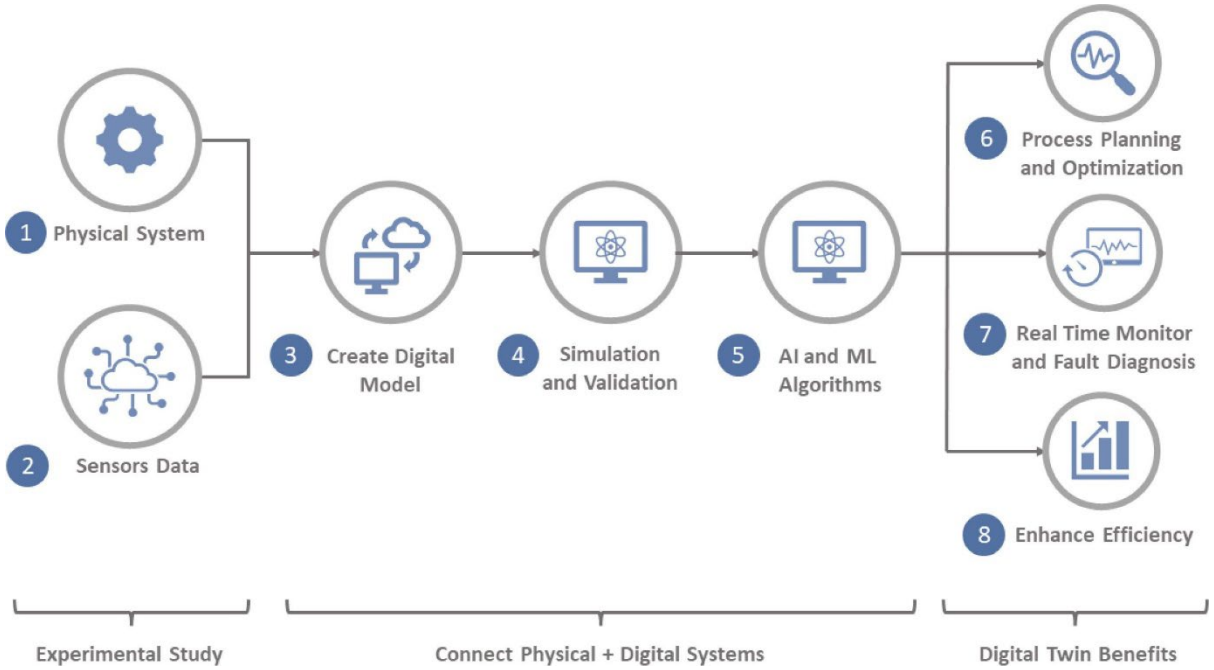

Figure 3 - The stages of a digital twin [51]

2.1.1 - Photovoltaic Digital Twins

Digital Twins can play a crucial role in multiple applications to increase the sustainability of the energy sector, ranging from identifying faults in a PV system [52] to larger scales, facilitating citizen engagement in urban planning decisions [53]. Specific use cases of digital twins in the sustainable energy solution sector include managing energy consumption by leveraging smart meter data to optimize energy usage patterns [54], and assessing urban heat dynamics to inform strategies for mitigating heat island effects and enhancing urban resilience [55].

Since solar energy power generation, and photovoltaic (PV) panels utilization as a sustainable energy solution is gaining more popularity because of the current energy and climate problems and becoming a part of urban infrastructure, digitalization in this sector can facilitate the rapid deployment of solar energy production in sustainable cities. This approach can increase reliability and ensure optimal performance.

The recent advancements in technologies like the Internet of Things (IoT), Machine Learning (ML), Artificial Intelligence (AI), and cloud computing are steering the global energy sector towards digitalization and interconnectivity [56]. This digital transformation allows the implementation of advanced strategies, such as Digital Twins, significantly boosting the efficiency of energy systems [57].

Using Digital Twins enables the simulation and optimization of active solar systems in urban areas by analyzing various factors such as weather conditions, ageing, dust accumulation, and shading effects on solar panels. This technology forecasts energy production and preemptively identifies maintenance needs to prevent potential issues. During design phases, Digital Twins optimizes PV panel configurations, pinpointing optimal locations for solar power generation. It also models the integration of solar energy into urban energy systems at different levels and determines the most effective methods to connect these systems to the grid [58].

To utilize Digital Twins for distributed solar systems on an urban scale, Kaitouni et al. [59] propose a strategy for an optimal operation that can be utilized (Figure 4).

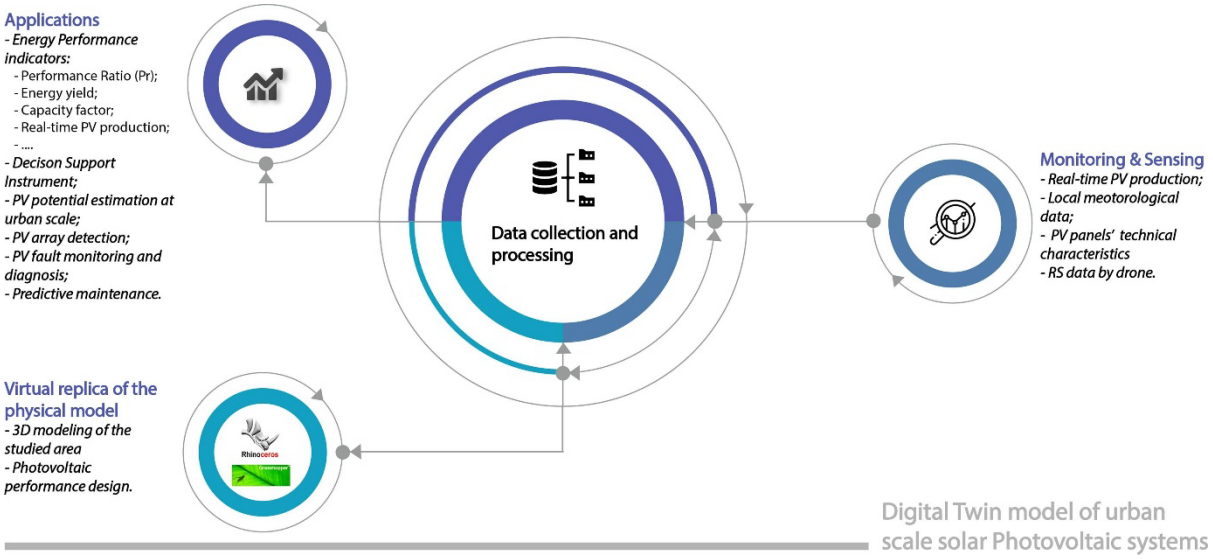

Figure 4 - Urban-scale solar photovoltaic systems Digital Twin model [59]

The Digital Twins framework can continuously monitor the efficiency of solar panels, collecting data on irradiance and temperature to quickly detect and fix issues with the components, and by integrating machine learning techniques, makes it possible to predict required maintenance and identify weaknesses in systems, providing an optimum maintenance timetable and preventing costly repairs. Moreover, it can optimize solar efficiency and provide real-time insights and financial analysis for operators, as well as offer energy management plans by simulating several scenarios involving panel layout, shading, energy consumption patterns, and grid restrictions [59, 60].

Using the Digital Twins paradigm, PV panels can be considered as physical objects whose digital representation of the system's energy production can provide real-time insights. These data can be produced as RGB or infrared images using satellite platforms [61, 62, 63] or be captured by Unmanned Aerial Vehicles (UAVs) [64, 65] (Figure 5).

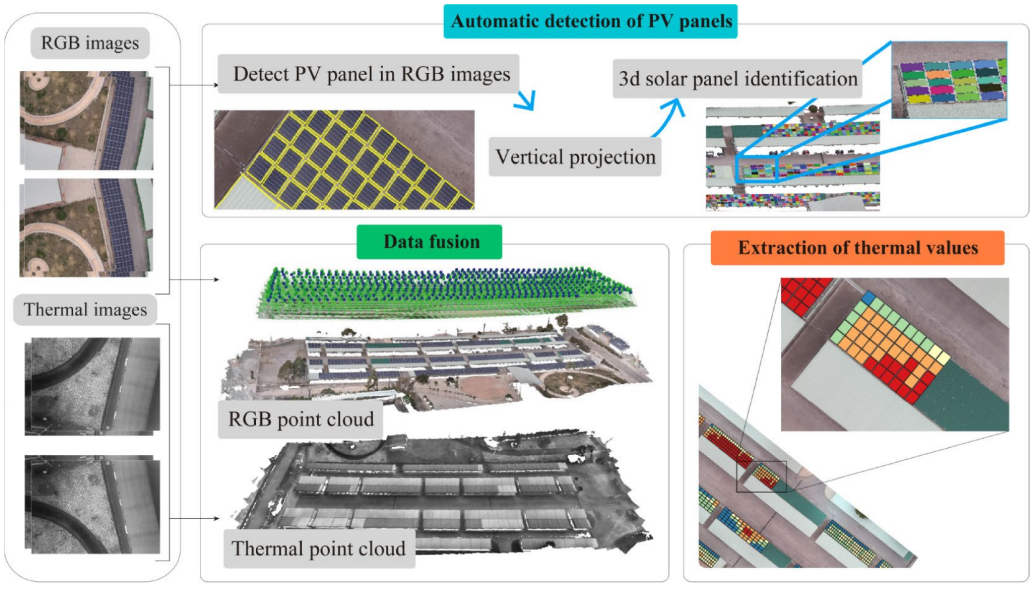

Figure 5 - An overview of a workflow for monitoring PV panels [66]

Another approach to obtaining real-time insights is enabling the data received from sensors and instruments inside the solar panel system. Implementing this method could significantly reduce expenses and result in a self-diagnosing automated system [67]. By incorporating PV potential

assessment using data flow, making simulations, and integrating real-time data, the system can be introduced as Digital Twins. Assessing the data flow can be mentioned as a layer of Digital Twins within the urban energy management sector, enabling stakeholders to take advantage of this strategy. Furthermore, this technique helps facilitate the deployment of solar energy sustainably and accelerates the transition towards smart cities and sustainable energy systems.

2.2 - Photovoltaic Potential Assessment

Improvements in the energy sector are required to address environmental degradation caused by carbon emissions. A global shift to low-carbon energy sources would assist in sustainability efforts and reduce environmental impacts, and renewable energy sources (RESs) can play a pivotal role in decarbonizing energy systems, and stabilizing energy prices [68, 69]. Solar panels offer several advantages as a renewable energy source in tackling climate change. They harness renewable sunlight to generate electricity, producing zero greenhouse gas emissions during operation. This clean energy production helps reduce reliance on fossil fuels, thereby lowering carbon emissions that contribute to global warming. Moreover, solar energy is abundant and widely distributed, making it accessible for deployment across diverse geographical regions. The optimal placement of PV plants in urban areas is made possible by remote sensing identification of ideal places, which is essential for advancing solar technology. Growing acknowledgement of the potential of this technology, new government programs, more power consumption, and improved cost parity and competitiveness with other technologies are the main reasons for the increased development of PV panels [70]. Evaluating the feasibility of integrating PV panels onto building rooftops requires considering principles like available area, solar radiation, and economic factors within a comprehensive framework to overcome efficiency evaluation barriers [71]. Furthermore, factors such as geography and climate also have an impact on the evaluation of PV potential in urban areas [72]. Therefore, to conduct an effective evaluation, it is necessary to take into consideration the characteristics that are related to these aspects (Figure 6).

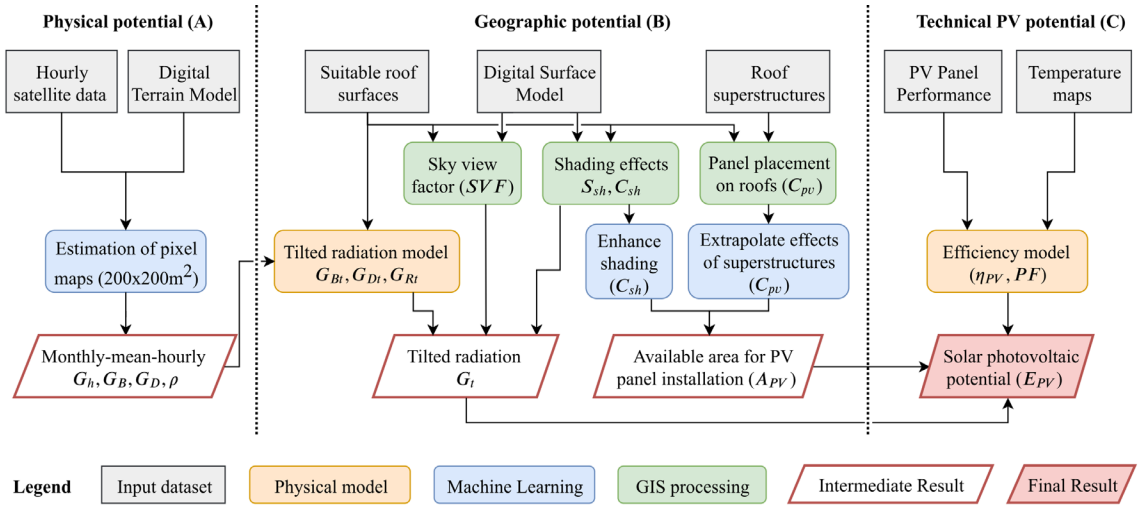

Figure 6 - A general workflow for modeling solar PV potential proposed by Walch et al. [73]

2.2.1 - Solar Radiation Models

Anselmo and Ferrara [41] have analyzed more than 100 research papers to identify the general trends in GIS-based PV potential calculation. One of the major outcomes of their study is the absolute relevance that solar radiation has in estimating the PV potential, because it is the only parameter which cannot be extracted from technical sheets but has to be estimated. Most of the models are clear-sky

models. Clear-sky solar irradiance parametric models seek to simplify atmospheric attenuation with relatively simple parameterizations to estimate solar irradiance under clear-sky conditions [74].
Several components can affect Solar Radiation (Figure 7), with physically based formulas not being able to consider them all e.g., they are not able to calculate radiation in the presence of solar barriers for real topographies. Such analyses can be done more accurately via computer modeling of the physical context across various spatial and temporal scales. Direct radiation barriers are almost simple to model while reducing diffuse irradiance from various sky directions is a significant difficulty because of anisotropy and the amount of visible sky at any given location.

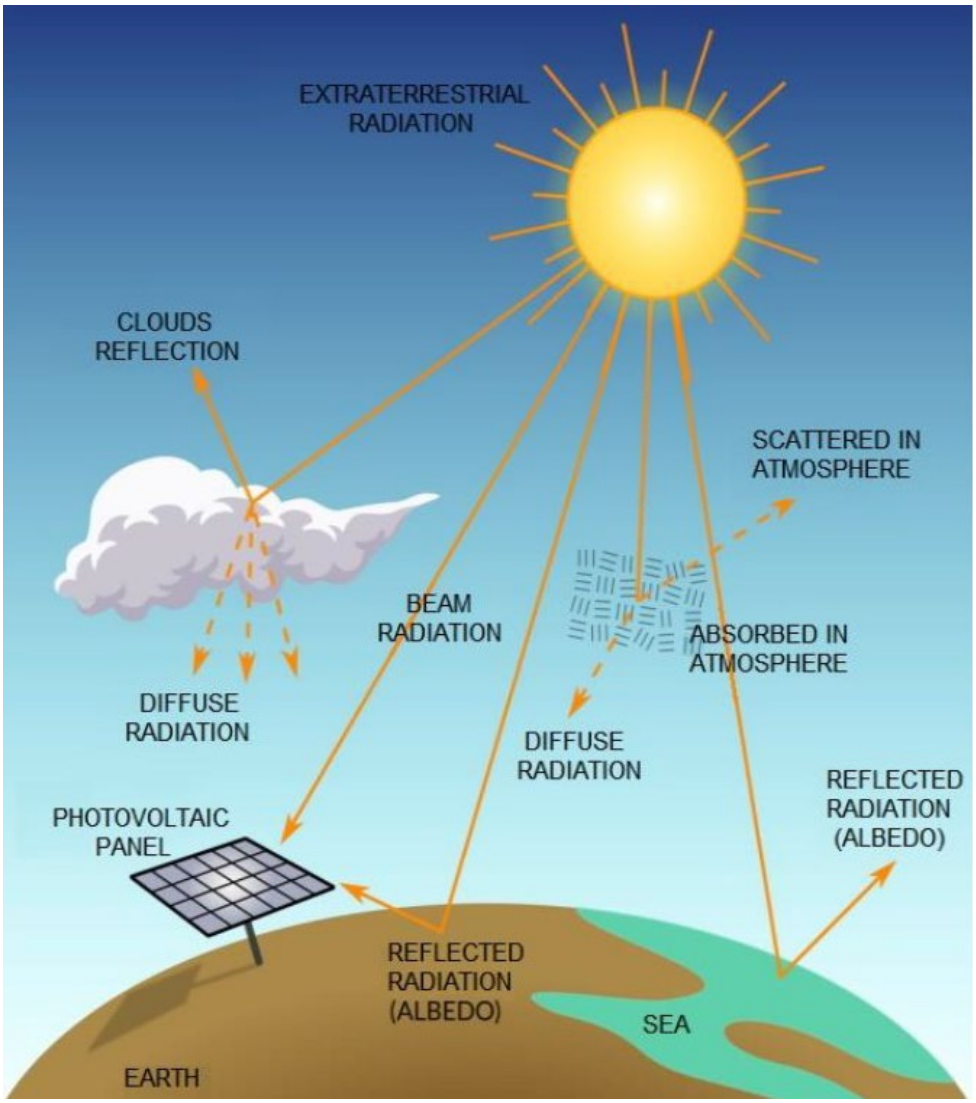

Figure 7 - Solar radiation components [75]

Solar energy research explores diverse models for irradiation. Freitas et al. [38], discuss computational solar radiation models (Table 2), highlighting the crucial balance between accuracy and computation time in model development among various categorizations available for solar irradiation models. Generally, to accurately assess the physical and geographic solar potential, a sequence of processes must be followed. This includes acquiring input data such as topographic information from Digital Surface Models derived from LiDAR, aerial or satellite imagery, and stereo imagery, as well as meteorological data from ground-based stations or satellites. Subsequently, integrating these inputs with

radiation models and GIS analysis enables the computation of solar irradiance, considering factors like sun position and local conditions such as shadows from buildings and vegetation in urban areas.

Table 2 - Computational solar radiation models by Freitas et al. [38]

Numerical methods	GOSOL
	SHADOWPACK
	ATM
	Sky view factor
	Solei-32
	SolarFlux
	Kumar et al. model
	RADIANCE
	Cumulative sky approach
	Daysim
	ArcGIS Solar Analyst
	SRAD
	Solar Envelopes
	Albedo calculator and Albedo viewer
	ESRA clear-sky model
	r.sun
	RayMan
	Preferable sky window
	Tooke et al.
	Solar3DBR
	SORAM
	Model comparison
Solar potential urban-oriented models.	All-in-one models
	CAD plugin-based models
	GIS-based models
Web-based solar maps	PVGIS
	PVWATTS and In My Backyard
	Mapdwell Solar Systems maps

The GIS-based approach for assessing suitable rooftops for PV panel installation involves developing models to estimate PV energy and solar radiation, considering geographical variables such as rooftop aspect and slope, resulting in a faster and more accurate evaluation process in comparison to manual methods or approaches based on constant values [71]. This approach can utilize both vector-based and raster-based methods. Raster-based 2.5D solutions, employing a Digital Elevation Model (DEM) raster, have been extensively embraced in various software for their simplicity [76, 77]. Open-source tools such as the r.sun command in GRASS GIS [78], utilized also by the UMEP plugin for QGIS [79], employ these raster-based methods for shadow computations. The insol package in R [80] provides similar features, suited for extensive natural landscapes, alongside the Solar Analyst extension [81] in ArcGIS supports raster-based shadow calculations [82].

According to Haklay and Weber [83], the vector-based 2.5D methodology offers several advantages over alternative approaches; firstly, it benefits from a broader availability of input data compared to specialized 3D models and high-resolution raster surfaces, facilitating comprehensive urban analysis; secondly, the processing doesn't require proprietary software or interoperability with complex specialized tools, enhancing accessibility and ease of implementation; and thirdly, the results can be seamlessly associated with individual urban elements, enabling precise analysis and interpretation. However, it's important to acknowledge that the 2.5D vector-based approach comes with certain assumptions and limitations, and in cases where these assumptions do not hold, results may be less

accurate compared to alternative approaches, such as the inability to represent complex geometric shapes beyond simple extrusions, which could limit the model's accuracy, particularly in intricate urban environments [84, 85]. Additionally, the computational efficiency of vector-based calculations may be challenged, especially for large study areas, compared to raster-based approaches [86].

2.2.1.1 - *Digital Elevation Model*

An important dataset for many GIS applications, the digital elevation model (DEM) represents terrain through an ordered set of ground elevation (spot height) in digital form. A DEM is an ordered array of numbers that describes the spatial distribution of elevations above a pre-defined datum, capturing various points in a given area in digital format [87]. This dataset is commonly referred to in many literatures by three terms: digital elevation model (DEM), digital surface model (DSM), and digital terrain model (DTM).

According to Zhou [88], the differentiation between the three terms is not universally agreed upon, but certain common principles may be outlined, including:

- A DEM represents the "bare" land surface, purportedly excluding trees, buildings, or other "nonground" objects.

- A DSM encompasses elevations of all elements, incorporating structures like buildings, treetops, and open ground.

- A DTM is a broader term denoting a DEM with various types of terrain data, such as morphological features, drainage patterns, and soil characteristics. When focusing solely on one terrain data type, such as elevation, it is termed a DEM, which is a subset of DTMs [89].

According to Croneborg et al. [90], a general name for digital images of topography, bathymetry, and/or elevation is a DEM, typically handled in electronic format. DEMs are usually represented as raster datasets, consisting of a grid where each cell indicates a specific elevation point on the ground [91]. The resolution of a DEM is determined by the size of these cells, significantly influencing the model's accuracy and practical utility. Higher resolution DEMs, characterized by smaller cell sizes, offer more detailed terrain depictions but also demand increased storage capacity and computational resources. The accuracy of DEMs and DEM-derived products depends on several factors, including the horizontal resolution, vertical precision, and the source of the elevation data. This accuracy becomes increasingly important as we extend the use of DEM data for spatial prediction of soil attributes [92].
Ideally, data collection would occur at a higher resolution, but this is typically constrained by cost and manpower [93].
Various representations exist for DEMs and similar models, ranging from flat depictions involving cell classification and colour assignment based on elevation to more complicated graphical renders like hatching techniques.
Lastly, a DEM serves as both a pixel-based "modelled representation" of the earth's surface and as input for modelling or analyzing topography using computers or algorithms [90] (Figure 8).

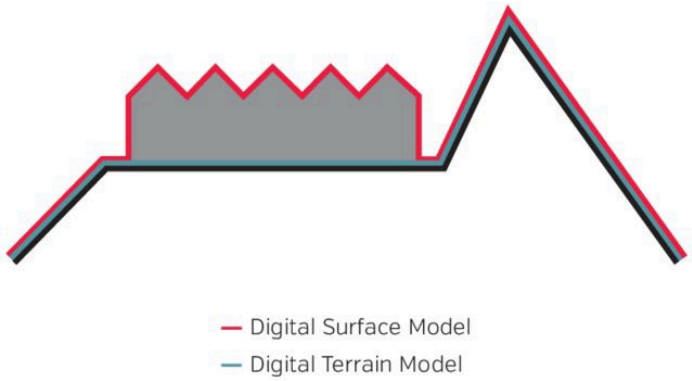

Figure 8 - Difference between DTM and DSM [94]

2.2.1.2 - *Slope and Aspect*

Aspect and slope are fundamental geographical parameters that play a crucial role in determining the suitability of sites for PV power plants. Slope, representing the steepness of terrain as a percentage of inclination, and aspect, delineating the direction of slope through azimuth angles ranging from 0° to 360°, are integral in assessing sunlight exposure and microclimate variances [95]. These parameters are commonly utilized for pre-filtering in site selection processes [41]. By leveraging DSM, DEM, and DTM, slope percentages and topographic orientations can be derived, facilitating comprehensive site assessments. The incorporation of slope and aspect data from terrain analyses allows for a thorough evaluation of terrain suitability, which is essential for determining optimal locations for the installation of PV panels. The aspect and slope of a surface directly affect the sunlight's incident angle on that surface, requiring precise computations using surface data to account for topographical nuances and accurately representing shadow estimation on the surface caused by surrounding landforms, a crucial factor influencing solar irradiation [96]. These computations also account for temporal variations, highlighting the dynamic nature of solar exposure.

2.2.1.3 - *Solar Irradiation*

The terminology related to solar energy outlines different aspects of the sun's influence on Earth. The term "solar radiation" describes the energy that the sun emits, which encompasses all types of electromagnetic energy that the sun emits, including visible, ultraviolet, and infrared light [97]. “Solar irradiation” is known as the quantity of solar radiation received per unit area at a specific location on Earth's surface [98]. This amount is commonly measured for a given period in Wh/m^2 or kWh/m^2. The power per unit area of solar radiation received at a particular location on Earth's surface is known as “solar irradiance”, and it is expressed in W/m^2. It is a representation of the power of solar radiation at a particular instant in time [99].

Solar irradiation, reaching the Earth's surface, results from complex energy interactions between the rays, the atmosphere and the ground. Comprehending solar irradiation is essential for harnessing the sun's energy for various applications. Within the renewable energy sector, solar irradiation stands as a key concept, representing the energy reaching a specific area within a defined timeframe, usually quantified as Wh/m^2 [100]. Solar radiation can be categorized into direct, diffuse, and reflected components, which together constitute global irradiation. Direct radiation refers to sunlight that reaches the Earth's surface in a straight line. Diffuse radiation, on the other hand, originates from various directions due to the scattering of solar radiation by clouds, air molecules, and aerosols in the atmosphere. This scattering phenomenon, including multiple reflections between the ground and clouds, contributes significantly to the diffuse radiation reaching the Earth's surface (Figure 9). Reflected

radiation occurs due to the reflection of both direct and diffuse radiation from the surface on which the collector is located, as well as from surrounding objects [101].

Various models have been developed to estimate diffuse radiation. Fan et al. [102] conducted a comparative study of these models, thoroughly examining techniques for determining diffuse radiation patterns. PVGIS utilizes an anisotropic two-component estimation model presented by Muneer [103] to calculate diffuse radiation values [104]. Understanding this differentiation is crucial, as various technologies harness different forms of solar energy.

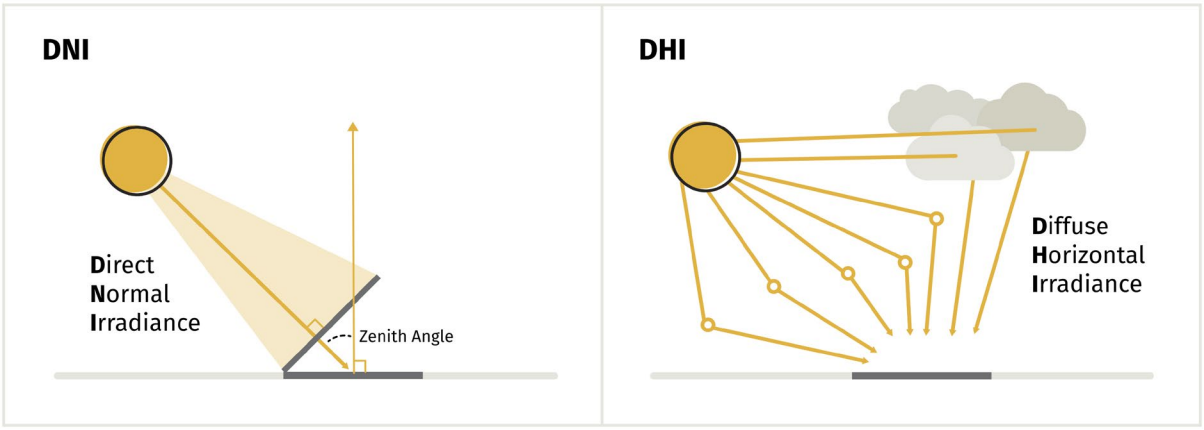

Figure 9 - Direct normal irradiance and Diffuse horizontal irradiance [105]

According to Freitas et al. [38], Meteorological stations generally measure the direct radiation component by quantifying global and diffuse radiation received on a horizontal plane, which can be obtained from equation below:

$$G_{horiz} = Dir_{horiz} + Dif_{horiz} = Dir_{horiz} \cos Z + Dif_{horiz}\, T_{Lm}$$

G_{horiz}	Global horizontal irradiance
Dir_{horiz}	Direct normal irradiance (DNI)
Dif_{horiz}	Diffuse horizontal irradiance (DHI)
Z	Sun's zenith angle.
T_{Lm}	Linke turbidity long-term monthly average

2.2.1.4 - *Linke Turbidity (T_L) Factor*

The Linke turbidity factor, serving as a valuable approximation for simulating air absorption and scattering of solar radiation in clear skies, characterizes the optical thickness of the atmosphere due to both water vapour absorption and aerosol particle absorption and scattering in comparison to a dry and clean atmosphere [106, 107]. A greater T_L factor corresponds to increased attenuation of radiation within the clear sky atmosphere, serving as a convenient metric to encapsulate atmospheric turbidity, widely utilized by engineers and consultants and essential in numerous models evaluating downwelling irradiance under clear skies across various disciplines such as renewable energies, climatology, agro-meteorology, and atmospheric pollution studies [108].

According to Chaâbane et al. [109], an indication of atmospheric turbidity can be described as the difference between the attenuation of solar radiation through a genuine atmosphere and that through a clean, dry atmosphere; moreover, It is precious when determining the amount of solar radiation and natural daylight in a location without clouds, and the T_L factor is crucial in calculating direct sunlight and scattered light in a specific area [109]. As highlighted in the study by Diabaté et al. [108], while direct determination of T_L factor using very clear sky observations is theoretically possible, such

experimental data is rarely available, leading to the common practice of assuming T_L factor as a parameter. Furthermore, the limited duration of radiation data time series poses a challenge for daily estimation; therefore, for practical purposes in numerous applications, researchers often rely on long-term monthly average values (T_{Lm}), as a suitable alternative [108].

2.2.1.5 - *Albedo*

Albedo, which translates to "whiteness," is the percentage of sunlight that a surface reflects back and affects temperature, evaporation, and heat transfer [110]. Albedo influences the amount of energy that the Earth absorbs from the Sun, thus directly influencing atmospheric conditions by controlling available energy; concurrently, roughness length, a vital physical characteristic at the land-atmosphere interface, influences mass, momentum, and energy exchanges [111].
The materials used in an urban environment and building coatings significantly impact the urban thermal environment (Table 3). Low-reflective and highly absorptive materials can boost the Urban Heat Island (UHI) phenomenon, impacting both building energy consumption and indoor and outdoor thermal comfort. This effect is notably heightened in Urban Heat Canyon (UHC) configurations, where the inter-building influence amplifies the thermal impact [112]. Dark-colored surfaces prevalent in urban areas, such as asphalt and roofs, typically exhibit low albedo, thus exacerbating the urban heat island effect. Conversely, light-coloured roofing materials utilization can reduce local heating, offering potential energy savings, especially in densely populated urban spaces [113].

Table 3 - Typical surface albedo values [114]

Material	Albedo coefficient
Highly reflective roof	0.60 - 0.70
White paint	0.50 - 0.90
Grass	0.25 - 0.30
Brick and stone	0.20 - 0.40
Trees	0.15 - 0.18
Red or brown tile	0.10 - 0.13
Concrete	0.10 - 0.35
Corrugated roof	0.10 - 0.16
Tar and gravel	0.08 - 0.20
Asphalt	0.05 - 0.20

2.2.2 - Panel Efficiency

Decades of dedicated research and innovation within the solar PV field have produced great progress, characterized by notable enhancements in energy conversion efficiency and substantial reductions in the costs associated with manufacturing processes, thereby facilitating broader accessibility to sustainable energy solutions. Solar PV power generation is an effective way to exploit renewable resources for power production [115]. It operates based on the PV effect, where potential differences are generated between dissimilar semiconductors or different areas of semiconductors combined with metals when exposed to sunlight [116]. Increased incident sunlight leads to higher photovoltaic power generation.
The performance and efficiency of PV modules are affected by several factors such as the kind of technology used, the light spectrum, solar irradiance, ambient temperature, humidity, and wind, with ageing and degradation also dependent on climatic and environmental conditions [117].

2.2.3 - Installation Area

When developing strategies to enhance sustainability in urban environments, the integration of rooftop PV panels emerges as a crucial consideration. A fundamental aspect of this process involves evaluating the rooftop space available for PV installations and understanding its potential impact on energy production potential. To promote the deployment of solar PV systems in buildings and inform future policy decisions, accurately assessing the rooftop solar PV potential is important. This assessment necessitates precise calculations of the usable rooftop area, which may be influenced by factors such as surrounding building shadows, elevator shafts, and architectural features like parapet walls and sloping roofs. By excluding shaded areas and accounting for structural elements, the total usable roof area can be determined. Subsequently, the available area for PV panels can be calculated based on panel dimensions and density, enabling the estimation of rooftop PV electricity generation. Identifying areas with high potential for rooftop PV installation holds significance for various stakeholders. Utilities can prepare to manage financial and technical implications, while developers can promote business opportunities, and policymakers can prepare inclusive policies for affordable and sustainable electricity access. This holistic approach to evaluating rooftop space for PV installations facilitates informed decision-making towards a greener and more resilient urban landscape.

Chapter 3 - Methodology

This study aims to evaluate the influence of value variation on solar irradiation calculation for urban buildings, given the relevance it has in photovoltaic (PV) energy production potential. The analysis attempts to present comprehensive results going beyond the limited availability of open-source data for model construction. Given the time-consuming characteristics of the process and the temporary outputs generated by the software, an automation model is defined to simplify operations. This automation model proposes a systematic approach to handling the sequential calculations involved in solar irradiation assessment and PV energy production estimation for buildings. By implementing automated procedures, the study seeks to enhance efficiency and reliability in data processing, thereby facilitating more robust analyses of urban energy dynamics.

3.1 - Tool Selection

Aligned with the goals set by international sustainability frameworks, deploying 3D GIS emerges as a practical tool, allowing precise analysis of geographical data for sustainable energy planning. This advanced analytical approach has prompted several studies to improve the evaluation of rooftop PV potential in cities, as mentioned by Anselmo and Ferrara [41].

Urban rooftop PV potential assessment remains challenging despite the various methodologies presented. Gagnon et al. [118] propose constant-value techniques, while Denholm and Margolis [119] suggest estimation methods considering roof area availability. Another method involves extracting roof planes from RGB images and converting them into 3D models [120].

However, the most efficient and practical approach is GIS-based, considered superior for its precision over constant-value techniques and scalability across extensive datasets, overcoming limitations of manual selection [118]. In order to utilize GIS-based methodologies, various studies employ land use data, satellite imagery, and models for urban PV potential assessment, emphasizing 3D urban modelling's significance aided by LiDAR technology for precise mapping in dense urban areas [121, 122, 123, 124].

Liao et al. [24] proposed a method aimed at accurately estimating rooftop solar irradiation in urban areas by addressing challenges in assessing PV potential over large built-up areas; it identifies seven crucial parameters (including Digital Surface Model (DSM), Sky View Factor, and building characteristics) forming the basis for modelling solar irradiation and compares the accuracy and computation time using three ML methods.

Furthermore, Vecchi et al. [125] employed a multi-scalar approach and GIS analysis to assess solar PV potential among diverse residential building archetypes, aiming for a holistic evaluation of solar energy in densely populated urban areas. A review by Anselmo and Ferrara [41] underscores the tools embedded in QGIS and ArcGIS as the most common GIS-based for solar irradiation analysis, highlighting their widespread usage in the field.

Therefore, this study considered these two, respectively r.sun.insoltime and Area Solar Radiation (ASR), for the quantification of global solar radiation. A crucial considered criterion for selecting these tools is the coherence between input and output, and checking the variability in inputs and their impact on the results. Additionally, the capability to be automated using Python programming, which is one of the objectives of the study, is considered. Using a comparative analysis will enable the selection of the most suitable tool for proceeding with the assessment of results. By employing commonly used tools in sustainable energy planning, this approach ensures a comprehensive evaluation of solar energy potential while leveraging the strengths of each software tool.

QGIS software offers the r.sun module, developed by Hofierka and Šúri [78], for solar irradiation analysis, seamlessly operates within the GRASS GIS framework, which is integrated into QGIS, an open-source platform [126]. This model utilizes equations from the European Solar Radiation Atlas (ESRA) [127] to calculate solar potential based on a user-inputted DSM.
This model is complex and flexible, generating raster maps of solar radiation based on factors like day, latitude, surface, and atmospheric conditions, including direct, diffuse, and reflected solar energy. Users can access solar parameters such as daylight length and sunrise/sunset times from the map history file or specify local time for custom calculations. Additionally, the model offers an option to account for topography's shadowing effect. Specifically, the r.sun.insoltime function is used to create a model of solar irradiance and irradiation, producing raster files that summarize daily sums of hours of sun, global radiation, beam radiation, reflected radiation, and diffuse radiation.
ArcGIS-Pro provides the ASR tool, part of the Spatial Analyst, for deriving incoming solar radiation. Similar to r.sun, it computes solar energy using a Digital Surface Model (DSM). Its parameters are classified into two main groups, including radiation parameters (such as azimuth and zenith divisions) and topography parameters (such as the "z factor" for bias correction). A DSM for the analysis area serves as this tool's primary input.
Comparatively, r.sun operates in two modes, calculating solar incidence and irradiance for a specific time or summing daily solar radiation values. Its parameters are more disaggregated than ArcGIS-Pro ASR, which shares the DSM as the principal input, thus requiring more comprehensive knowledge about the territory under analysis. Additionally, r.sun does not compute slope and aspect at every iteration, requiring pre-calculation of these maps. Further parameters in r.sun include options for the Linke turbidity (T_L) factor, albedo, beam and diffuse radiation, horizon values for shadowing calculation, days of the year for radiation calculation, time step for daily radiation sums computation, and solar constant. These multiple output options lead to diverse usages in the analyzed studies.

3.2 - Data Gathering

The data-gathering step in the methodology involves creating a supporting dataset for conducting the assigned tasks in the software. GIS-based model investigations require access to relevant environmental and geographic data for the chosen study area. This step involves identifying and collecting the specified datasets and parameters, ensuring they align with the precise specifications and requirements for successfully executing the planned analysis and computations within the software environment. Therefore, a preliminary phase includes defining the parameters needed by software packages for solar radiation analysis.

3.2.1 - Required Inputs

Accurate and efficient solar radiation calculations require careful consideration of various factors, including computational requirements and potential time consumption, particularly for large Digital Surface Models (DSMs). The latitude of the site location is pivotal in solar declination and position calculations. However, parameters like sky size, transmissivity, and diffuse proportion significantly impact calculation accuracy and time efficiency. These factors, along with essential inputs such as the T_L factor and beam and Diffuse to Global Radiation (DG) ratio, contribute to the precise solar analysis. Incorporating these considerations ensures robust and reliable outcomes in sustainable development initiatives. The selected GIS-based solar radiation analysis tools for this study, ASR in ArcGIS Pro and r.sun.insoltime in QGIS, both utilize DSMs as the primary mandatory input to efficiently compute three-

dimensional geometries, enabling accurate solar radiation estimations. For QGIS, the only other mandatory input is the day number, ranging from 1, January 1st, to 365, December 31st.
Several optional inputs enhance solar radiation estimation in these tools, meaning that if these inputs are not provided by the user, the algorithm will use default values. For ASR, these inputs include latitude, sky size, time configuration, hour interval, z-factor, directions, zenith divisions, azimuth divisions, diffuse model type, transmissivity, slope, and aspect. For r.sun.insoltime, the inputs include the T_L factor, albedo coefficient, real-sky beam radiation coefficient, real-sky diffuse radiation coefficient, latitude, longitude, slope, and aspect.
ASR calculates the aspect and slope from the inserted DSM raster file or allows the user to insert a constant value for calculation, while r.sun.insoltime requires the aspect and slope as separate raster file inputs or allows the user to insert a constant value.
Considering all the mentioned above, the only parameters common to both tools are the DSM and the diffuse to global radiation ratio. Notably, for result evaluation purposes, the study opted not to include the albedo coefficient, focusing instead on the DSM, T_L factor, and DG ratio for precise solar analysis.

3.2.2 - Data Sources

The first input for analyzing solar irradiation is a Digital Surface Model (DSM), which is created by capturing raw laser scanning data as 3D points and interpolating them onto a regular grid to form a continuous height surface; it can directly affect analyses like image segmentation, feature extraction, and object reconstruction [128]. For tasks requiring accurate topographic data sets, the availability of digital terrain information at high spatial and temporal resolutions and accuracy is becoming more crucial [129]. Unmanned aerial vehicles (UAVs) equipped with nonmetric digital cameras are being studied as a potential solution to the limitations of traditional methods [130]. UAVs are a relatively new type of remote sensing platform that have several advantages over satellites and traditional piloted aircraft, such as superior temporal and geographical resolutions, reduced operating costs, and greater operational flexibility [131].
Given the requirement for high precision in reconstructing urban surface features, a 50cm Digital Surface Model (DSM) obtained from the TerraItaly™ Metro HD project's LiDAR acquisition on January 29, 2022, was selected. This DSM was specifically procured for the SDG11 Lab at Politecnico di Torino. The data for this file was acquired by Compagnia Generale Ripreseaeree S.p.a., which utilized photogrammetric images and LiDAR (Light Detection and Ranging) data captured across the entire City of Turin using a Leica CityMapper-2S Digital sensor.
This research collects essential weather parameters from widely used open-source datasets to establish a dependable dataset. Specifically, datasets from PV Geographical Information System (PVGIS), Solar radiation Data (SoDa) website, and Meteonorm software (v8.2.0) were selected.
PVGIS, supported by the European Commission, includes the SARAH-2.1 solar radiation database, offering global solar radiation and PV production data from 2005 to 2020, excluding the polar regions. Other available datasets include SARAH (1st version) covering 2005 to 2016, and ERA5, which provides climate variables and irradiance values validated against ground station data from 2005 to 2020 [132]. The PVGIS-SARAH2 solar radiation data are based on the second version of the SARAH data record from the EUMETSAT Climate Monitoring Satellite Application Facility (CM SAF) [133]. This dataset utilizes images from METEOSAT geostationary satellites, which cover Europe, Africa, and Asia within the longitude and latitude range of ±65°. The data consist of long-term averages derived from hourly global and diffuse irradiance values over the years 2005-2020. The solar radiation datasets contain average irradiance over the specified period, measured in W/m², considering both day and night time. Optimum angle datasets are measured in degrees from horizontal for a plane facing the equator

(south-facing in the northern hemisphere and vice-versa). Available data sets include monthly and yearly average values [134].

SoDa offers a diverse range of services encompassing solar, meteorological, altitude, astronomical, and atmospheric data, catering to various solar energy applications such as site assessment, electricity production monitoring, and forecasting [135]. The SoDa dataset utilizes the HelioClim family of databases, which employ a satellite-based method to provide total solar irradiance and irradiation values at ground level. The total irradiance, equivalent to spectrally integrated solar radiation, is available across regions including Africa, Europe, the Atlantic Ocean, the Mediterranean Basin, and parts of the Indian Ocean (approximately -66° to 66° latitude and longitude) [136]. Within this website dataset, the T_L factor is calculated using beam or global radiation measurements at the ground, supported by the European Solar Radiation Atlas (ESRA) clear sky radiation model. This approach integrates satellite and ground-based information, applying fusion methods to address the significant spatial resolution differences. Additionally, the dataset incorporates water vapour maps and orography information to enhance accuracy [137].

Meteonorm software offers a detailed climatological database created for solar energy applications, generating typical years based on long-term monthly averages for global locations, and it is used as a standard tool for engineering design, environmental research, agriculture, forestry, and other meteorological and solar energy-related tasks. [138].

Meteonorm software obtains data from numerous reliable databases, uses methods to merge the ground and satellite data [139], ensuring comprehensive global simulation capabilities for solar energy systems and environmental simulations. The Swiss database, compiled by MeteoSwiss, includes 10-year mean data for parameters such as global radiation, temperature, wind speed, and sunshine duration, covering the 1983–1992 period. In Meteonorm V8.2.0, this foundational dataset has been extended to include radiation data from 2001–2020 and temperature, wind, and precipitation data from 2000–2019. Additional international datasets are incorporated, including the GEBA (Global Energy Balance Archive), which has been updated to cover the period 2001–2020, and the Globalsod data from the National Climatic Data Center (NCDC), which includes temperature, precipitation, and wind speed data processed for 2000–2019. Furthermore, radiation data from the German Weather Service (DWD) for 2001–2020 is included. Monthly average radiation values are calculated over periods of at least ten years, with a uniform period applied to each continent. For some weather stations, data has been supplemented using a differential procedure from neighboring stations. The Meteonorm database comprises data from more than 8'300 weather stations globally. The type and the distribution of the weather stations worldwide are outlined in Table 4. This software allows customization of the dataset and period for calculations. The "contemporary dataset" utilized in this study spans from 2000 to 2019 for air temperature, dew point temperature, wind speed, wind direction, days with precipitation, and precipitation amount, while radiation data is available from 2001 to 2020 [138].

Table 4 - Distribution and number of available weather stations for Meteonorm software [138]

Available parameters	Global radiation and temperature	Temperature, additional parameters	Only temperature or radiation	Total
Europe	450	1'133	62	1'645
Asia (with Russia)	287	1'514	40	1'841
Africa	134	431	35	600
North America	356	1'477	80	1913
South/Central America	76	530	20	626
Australia / Pacific	77	1'607	24	1'708
World	1'380	6'692	261	8'333

Incorporating insights from scholarly literature related to solar irradiation assessment in the city of Turin, this research considers the T_L factor calculated for the selected area [140]. Additionally, suggested standard values for the T_L factor provided by Hofierka [141], as outlined in the QGIS manual, are utilized as sources for data gathering.

To bring it all together, in this study, the T_L factor is derived from the SoDa and Meteonorm datasets, supplemented by values calculated for Turin and suggested constants outlined in the QGIS manual. Moreover, the DG ratio is collected from PVGIS and Meteonorm datasets; lastly, the Global Horizontal Irradiance (GHI) is collected from the PVGIS dataset as well. This multifaceted approach could ensure robust and precise data for subsequent analysis and applications.

3.3 - Data Processing

Following the completion of data gathering, the subsequent phase involves processing the data on solar radiation, including translating gathered data into plans of tests for evaluation, which is a critical step in determining PV potential. To understand the impact of different input values on the outcomes, exploring various combinations of extracted values is imperative. The diversity in input combinations is directly proportional to the multitude of values extracted from the sources, necessitating a meticulous approach to analysis. Weather parameters have been extracted on a monthly basis, allowing monthly solar irradiation calculations. Subsequently, these acquired values have been considered for further analysis, where they are averaged across distinct portions of time: seasonal intervals, which encompass winter (spanning from November to February), spring/autumn (comprising September, October, March, and April), and summer (encompassing May to August), as well as yearly periods, representing the average value across all months.

Aggregating these parameters not only allows for verifying the need for temporal accuracy and the level of detail in the information but also ensures that variations in solar radiation are appropriately considered and help in identifying significant seasonal patterns or anomalies. Furthermore, computational complexity can be decreased by aggregating the data, which speeds up the evaluation process and makes it simpler to compare data across various time scales, thereby streamlining the derivation of meaningful conclusions and informed decisions.
This process extends to values from sources including the T_L factor and DG ratio, providing a comprehensive understanding of their impact on solar radiation.
Afterwards, the obtained seasonal and yearly values serve as input data for monthly solar irradiation analysis.
In ArcGIS software, the monthly interval calculation can be exploited, whereas, in QGIS, the process first involves calculating daily radiation and then conducting monthly solar irradiation calculations using the raster calculator tool and multiplying the daily acquired value by the number of days in the respective month to derive the total monthly solar radiation. The number of days in the evaluation period is necessary for accurate estimation, with each day of the year ranging from 1 (1st January) to 365 (31st December). The list of significant days corresponding to each month, provided by Klein [142], is shown in Table 5, which is considered in this study.

Table 5 - Day number and number of days for each month of the year [142]

	Jan.	Feb.	Mar.	Apr.	May.	Jun.	Jul.	Aug.	Sep.	Oct.	Nov.
Cumulative average days	17	47	75	105	135	162	198	228	258	288	318
Number of days	31	28-29	31	30	31	30	31	31	30	31	30

Given that both assessing GIS tools generate raster files as outputs, the zonal statistics tool is utilized to derive statistical indicators, including minimum, maximum, and median values, to understand solar radiation variations for the selected buildings.

3.4 - Automation

The process of calculating solar irradiation through QGIS software is time-consuming due to its repetitive nature. This process requires operating the same tool and procedure multiple times with varying input values, resulting in the generation of numerous temporary files. While these files are helpful in the computation phase, they become redundant once the final results are obtained. This accumulation of temporary files consumes storage space and increases the complexity of managing the overall process. Automating this process can significantly reduce these challenges and streamline the workflow.

The "Graphical Modeler" tool in QGIS facilitates the automation of the entire solar irradiation calculation process. This tool allows users to create a workflow with composite functions, where the output of one algorithm or operation serves as the input for subsequent steps, thereby eliminating the need for intermediate files. Automation reduces the computational load and enhances resource efficiency.

This tool provides an intuitive interface for creating complex models in Geographic Information Systems (GIS), where analysis operations are typically interconnected rather than isolated, integrating these operations into a single process, executing the chain of operations with different inputs later as a single algorithm regardless of the number of steps and algorithms involved, thereby streamlining the workflow and saving time.

Creating a model involves two key steps:

1. Definition of Necessary Inputs:

   Inputs are added to the parameters window, allowing user to set their values when executing the model. Since the model is an algorithm, the parameters window is generated automatically, similar to other algorithms in the processing framework.

2. Definition of the Workflow:

   The workflow is defined using the model's input data. Algorithms are added, and their use of defined inputs or outputs generated by other algorithms in the model is specified.

Additionally, the Graphical Modeler tool generates Python code corresponding to the defined workflow. This feature enables access to Python scripting capabilities, allowing for further customization and integration with external libraries. Python scripting extends the functionality of the automation process beyond the built-in tools of QGIS, enhancing its versatility for various scenarios.

In this study, the steps for calculating solar irradiation are executed sequentially using the Graphical Modeler tool in QGIS.

The process starts with the insertion of a Digital Surface Model (DSM) file - which serves as the input for computing the Aspect and Slope files - and selected buildings shape file. Then, incorporating additional weather and geographical inputs along with the aspect and slope data, the r.sun.insoltime algorithm is executed for specified days. In the next step, the raster calculator algorithm calculates the solar radiation for each month using specific values corresponding to number of days of the month is calculated; and finally, the zonal statistics algorithm provides statistical indicators - in this study

Maximum, Minimum, and Median values are obtained - for buildings, which are included in the final results.
Overall, the use of the graphical modeler not only simplifies complex processes but also enhances efficiency and resource management in GIS operations, making it a powerful tool for tasks such as solar irradiation calculation.

3.5 - Case Study

To address the municipality's interest in urban development on the outskirts, our study focuses on the Northern edge, particularly District 6, chosen for its diverse characteristics. This district encompasses a range of human activities, from densely populated areas to industrial zones and the primary Turin dump. Divided by the Stura river, the Barriera di Milano area near the city center contrasts with the residential and infrastructural landscape of Falchera, characterized by a housing district established in the 1950s.
The district's evolution has been influenced historically by its industrial heritage. The nearby Aurora area housed significant national plants, including the FIAT engine production facility. Post-World War II, the surge in employment led to a demand for housing, resulting in the development of marginal districts like Barriere. Construction peaked in the 1970s, with sporadic additions in the 1980s. Notably, the area's northwest border aligns with the renovated backbone, following the Gregotti and Cagnardi masterplan in the 2000s. Similarly, the Bologna street area underwent revitalization during this period. Exceptions to the post-war development include pre-war industrial buildings outside toll barriers, such as the Docks Dora warehouses, biscuit production facility to the west, and a woollen mill and military warehouse to the east.
The construction period influences building height, which is crucial for our research. Buildings typically range from 3 to 6 floors, with newer constructions adhering to urbanization standards, preventing shadowing of surrounding structures.
Understanding the spatial and historical context of District 6 is essential for our study, as it informs decisions regarding urban planning, energy assessment, and sustainable development initiatives. Established in the late 19th century, Barriera experienced rapid growth due to factories like FIAT, attracting migrants from rural and urban areas. Recent demographic changes include immigration from Africa and Eastern Europe.
The municipality has undertaken significant regeneration efforts, notably through the Integrated Programme of Urban Development (PISU) launched between 2007 and 2013. These initiatives aimed to improve public spaces and mobility infrastructure.
Additionally, the proposed Variante 200 urban transformation plan anticipates further development, leveraging planned subway lines. Recent years have seen a growing cultural scene in Barriera. These transformations and cultural activities provide valuable context for studying the district's socio-economic and environmental dynamics.

In this study, four representative buildings are selected within the study area to facilitate the process and enable efficient analysis of result variations, each with unique characteristics:

- Building 1: This building features a simple two-pitched roof, oriented North-South, covering an area of 700.3m². It has six floors, and the elevation is covered with light-colored materials. The straightforward design makes it an ideal candidate for analyzing the basic impacts of solar irradiation on a conventional roof structure. The North-South orientation allows for a

comparative study of solar exposure on both the eastern and western slopes throughout the day (Figure 10).

Figure 10 - Schematic representation of building 1 roof, and street view.

• Building 2: This structure has a more complex four-pitched roof, oriented Northwest-Southeast, covering an area of 680.2m². It is a four-floor building made of brick. The orientation allows for an analysis of how different roof pitches and angles affect solar irradiation levels, particularly during transitional periods of the day, such as early morning and late afternoon (Figure 11).

Figure 11 - Schematic representation of building 2 roof, and street view.

• Building 3: Similar to Building 2, Building 3 also has a four-pitched roof but is oriented Southwest-Northeast, covering an area of 419.2m². It is also a four-floor building made of brick. This orientation allows for the study of the impact of afternoon and early evening sun on solar irradiation levels (Figure 12).

Figure 12 - Schematic representation of building 3 roof, and street view

• Building 4: The most complex of the selected buildings, Building 4, features multiple pitches and surrounding shadowing elements, primarily trees, covering an area of 1371.1m². It is a single-story building. The intricate roof structure and the presence of shadows provide insight into how shading from nearby elements can influence solar irradiation (Figure 13).

Figure 13 - Schematic representation of building 4 roof, and street view

By selecting these four buildings with diverse roof structures and orientations, the study aims to cover a broad spectrum of scenarios, ensuring a comprehensive analysis of solar irradiation impacts on different types of buildings. This approach helps in understanding the nuances of solar energy capture and the factors that influence its efficiency in various architectural and environmental contexts.

Chapter 4 - Results

This thesis concentrates on attaining predefined goals in evaluating the PV systems' energy production potential in urban areas and investigates essential elements of precise parameterization, evaluation of tools, and automation. The study explores the impact of parameters on accuracy, the efficacy of tools and setups, and the possibility of automating processes using GIS tools.

4.1 - Tool Selection

To determine which of the two tools, r.sun.insoltime in QGIS and Area Solar Radiation (ASR) in ArcGIS Pro, provides the most accurate estimation of solar irradiation, variations in DG ratios are assessed for both tools using identical input parameters. Changing the DG ratios allowed us to check the impact on the results and compare the outcomes from each tool.

For ASR, the DG ratios used are 0.25, 0.5, and 0.75, with the transmittivity set to 0.5 by default. For r.sun.insoltime, the DG ratio input values are also 0.25, 0.5, and 0.75, with the Linke turbidity (T_L) factor and other values not set. The median yearly solar irradiation for the four buildings under study are considered to compare the results and analyse the variations.

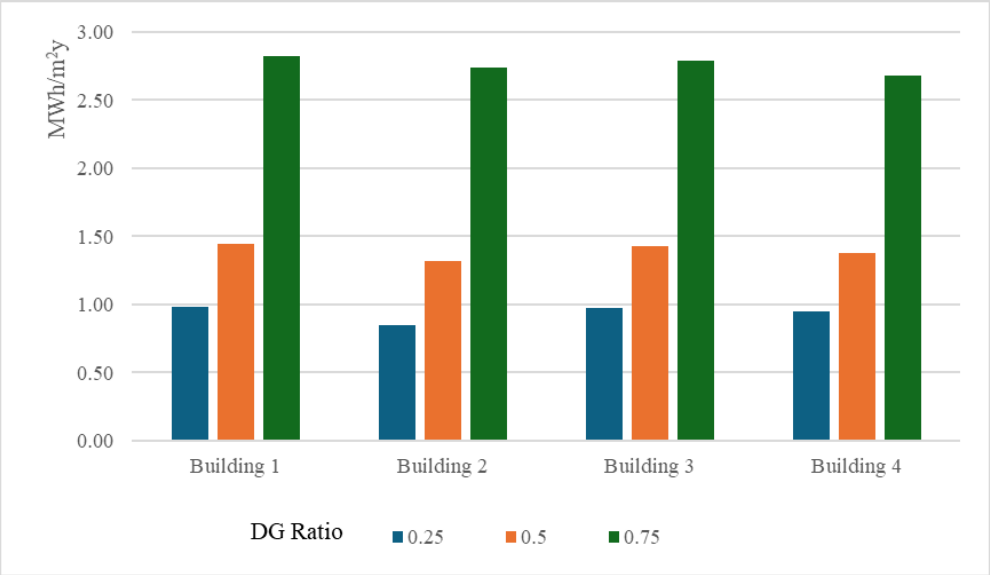

Figure 14 - Comparison of obtained results from ASR by changing the DG ratio parameter

Results from ASR (Figure 14) show that for all four buildings, changing the input affected the output. When the DG ratio increased, the solar irradiation outcome also increased.
The DG ratio was increased in two steps, each by 0.25. However, the second increase in results was larger than the first.

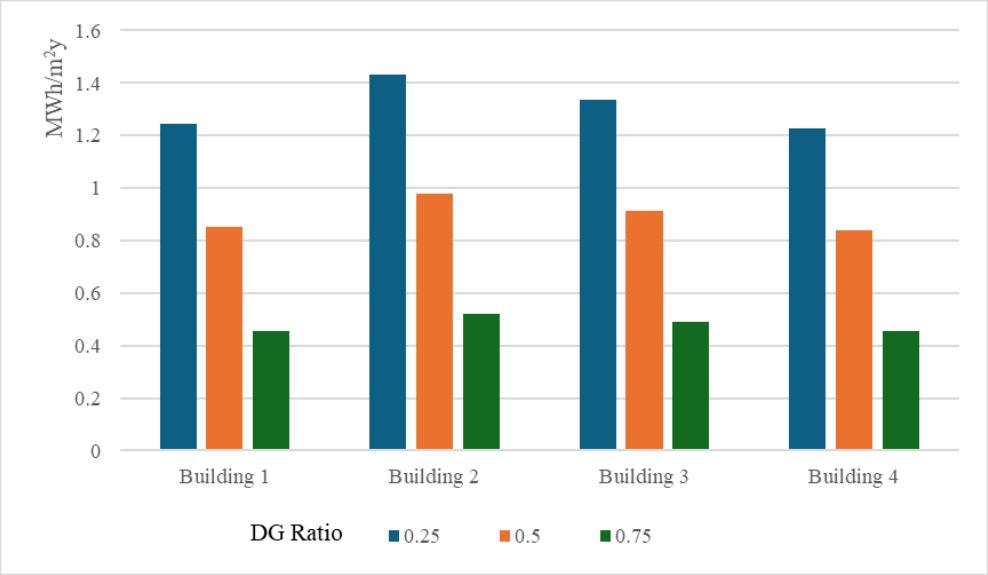

Figure 15 - Comparison of obtained results from r.sun.insoltime by changing the DG ratio parameter

On the other hand, results from r.sun.insoltime (Figure 15) showed that for all four buildings, changing the input also affected the output. However, when the DG ratio increased, the solar irradiation outcome decreased. The DG ratio was increased in two steps, each by 0.25, and the decrease in results was almost the same for each step.

According to the results, the outcomes from r.sun.insoltime were found to be more consistent with changes in the inputs. By using the same parameters for both tools and comparing the results, the study found that the trends in r.sun.insoltime were more logically expected, making it the preferred tool for this study.

4.2 - Collected Data

The primary results begin with observations on the meteorological parameters gathered for Turin, highlighting both yearly and monthly outcome trends and evaluating different data sources and aggregations. In this phase, the investigation centres on calculating solar radiation using the r.sun.insoltime tool in QGIS. Essential data for this tool, including DEM, T_L factor, and DG ratio, are collected from open-source datasets. Monthly values are collected and aggregated into seasonal and yearly parameters to assess the variations and their impact on output. This approach illustrates the trend of variations, and by comparing the differences in output, it is possible to identify suitable parameters for solar radiation estimation in Turin.

4.2.1 - Digital Elevation Model

In the data gathering category, the primary elevation file used for this research is the Digital Surface Model (DSM), which is produced in 2022 and covers the entire area of Turin. The data was collected using a Piper PA31 aircraft that was calibrated to an altitude of roughly 1500 meters. Through an accurate acquisition approach, the density of the LiDAR point cloud was estimated to be approximately 40 points per square meter. This high density allowed for the development of a DSM with a spatial resolution of 0.5 meters. This high-resolution capability facilitates in-depth investigations, enabling the accurate identification of specific characteristics such as roof slopes, chimneys, and dormers. Afterwards, the study area is extracted from this dataset, with a specific focus on geographical borders that are important to the research region.

The study gathers the essential meteorological factors required for solar irradiation estimation tools. These parameters, crucial for GIS tools, encompass T_L factor and DG ratio. The collection of these parameters is vital for ensuring accurate calculations, given the specific combinations demanded by different tools. For example, ASR in ArcGIS Pro relies on the DG ratio and transmissivity for its computations. On the other hand, the r.sun.insoltime tool in QGIS utilizes a distinct combination, emphasizing both the DG ratio and T_L factor for its estimations.

4.2.2 - Linke Turbidity (T_L) Factor

The T_L factor for the Turin study area is obtained from various sources, including SoDa datasets, Meteonorm software datasets, constant values reported by Fracastoro et al., and values mentioned in r.sun documentation. Meteonorm offers four different configurations for Turin, resulting in four distinct values for the T_L factor, thus indicating the contribution of seven different sources to the dataset. Monthly data collection ensures the highest temporal resolution possible. The SoDa dataset combines global satellite data on clear sky radiation, water vapor, and aerosol optical depth with ground-level turbidity measurements, using fusion methods to address differences in spatial resolution along with water vapor maps and terrain information. This results in raster data with different values across multiple pixels for the study area. Due to the SoDa raster's spatial resolution of about 10 km at mid-latitude (1/12°), multiple values are returned for Turin [137]. In order to address this, an average value for each month is calculated, producing a single T_L value from SoDa. Meteonorm determines the T_L factor using satellite data and ground station measurements. Ground data for Turin are collected from Aeronet stations, with the nearest located in Ispra, approximately 110 km away, as well as from weather stations at Turin Airport (Caselle Torinese, TO) and in the area of the Maddalena Hill (Figure 16). Four configuration options in Meteonorm offer various methods for calculating the T_L factor, incorporating direct measurements from Aeronet stations and weather stations (with and without (W/O) the inclusion of direct global radiation measurement) alongside interpolated data for a central location in the city [138].

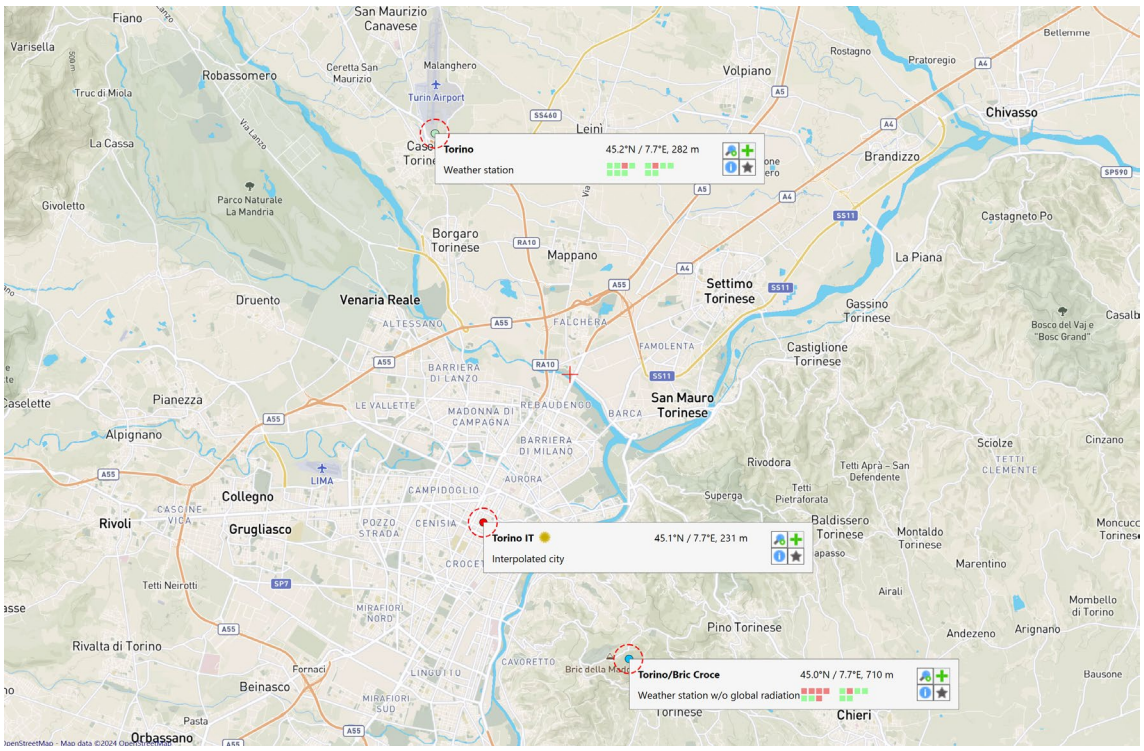

Figure 16 - Available locations for Turin in Meteonorm software (v8.2.0)

Additionally, values from the documentation supporting the use of the r.sun tool by Hofierka et al. [141] are incorporated into the analysis. These values, categorized broadly into city, mountains, countryside, and industrial areas, represent average values for a mild climate in the Northern Hemisphere, serving as alternatives when specific data are unavailable. Nonetheless, their inclusion in this study allows for evaluating their influence on the final results. Furthermore, site-specific values, such as those calculated by Fracastoro et al. [140], were also integrated into the dataset. Table 6 presents the T_L values for the city of Turin, obtained specifically for this study.

Table 6 - Linke Turbidity factor values extracted from the sources for the city of Turin

Month	Source						
	QGIS (city) [141]	Fracastoro et al. [140]	Meteonorm Weather station	Meteonorm Aeronet	Meteonorm Interpolated	Meteonorm w/o	SoDa [143]
January	3.10	3.50	2.58	2.99	2.60	2.40	3.40
February	3.20	4.30	2.79	3.70	2.82	2.60	4.15
March	3.50	4.00	3.26	4.04	3.29	3.03	4.60
April	4.00	4.20	3.77	4.41	3.8	3.51	4.65
May	4.20	4.60	3.74	4.44	3.77	3.48	4.60
June	4.30	4.60	3.76	4.62	3.79	3.50	4.90
July	4.40	4.40	3.51	4.14	3.54	3.27	4.25
August	4.30	4.50	3.43	3.97	3.46	3.19	4.15
September	4.00	4.30	3.34	4.23	3.37	3.11	4.15
October	3.60	4.00	3.25	4.19	3.28	3.02	4.15
November	3.30	4.40	2.84	2.91	2.87	2.64	3.25
December	3.10	4.40	2.55	2.73	2.57	2.37	3.15

Meanwhile, these numbers are displayed in Figure 17, in order to graphically represent the findings to facilitate better understanding.

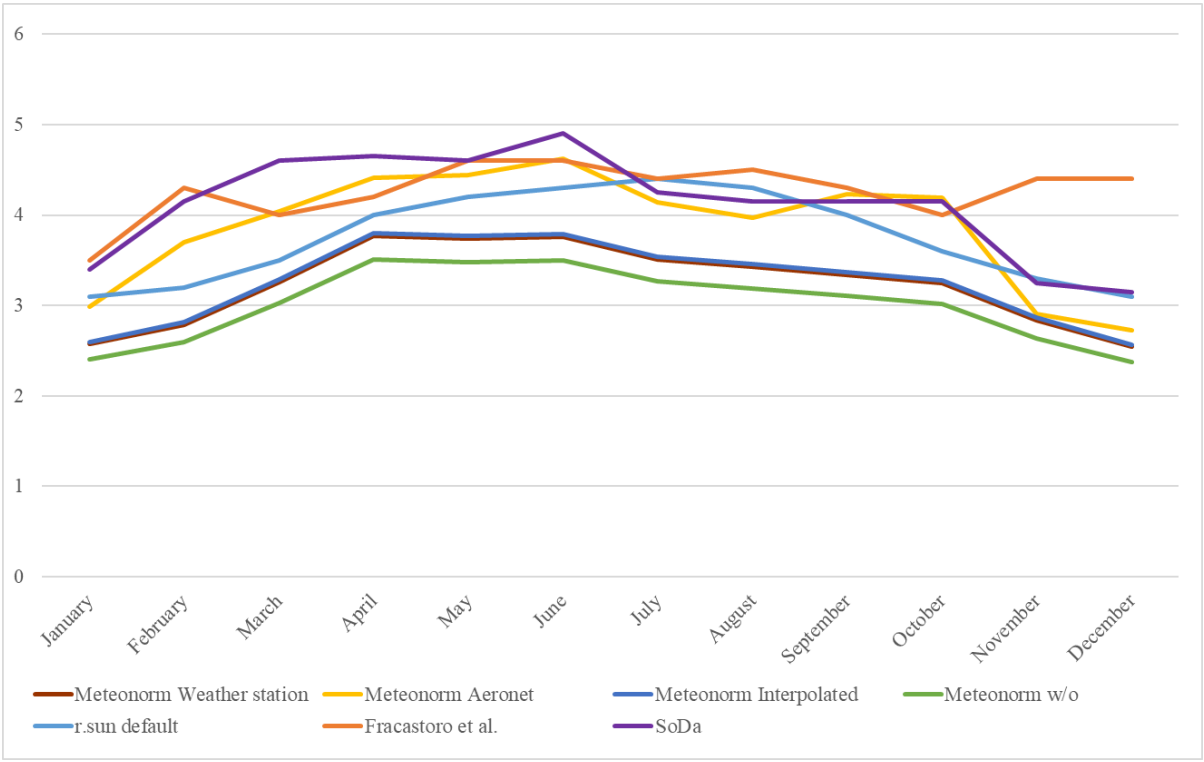

Figure 17 - Monthly values of Linke Turbidity Factor for the city of Turin

Upon examining the data, it is evident that the T_L Factor has a higher value during the summer months (June, July, and August) in comparison with the winter months (December, January, and February). The variation of this factor can be attributed to the levels of aerosols [144] and water vapour [145] present in the atmosphere during seasons, as well as the influence of air mass, the irradiance on a surface normal to the solar beam, the solar constant, and the reduction factor for mean solar distance at specific times [146].

The comparison of the data from the sources and the computation of the averages reveals significant inconsistencies. More precisely, the T_L factor, calculated using the Meteonorm W/O data set, regularly exhibits lower values throughout the year in comparison to other sources.
In contrast, the computed yearly T_L factor averages, using the values reported by Fracastoro et al. consistently show greater values, especially during the winter season. These differences can be ascribed to variances in the data collection methods, spatial resolution, or interpolation techniques used by each source.
Further analysis shows that some sources exhibit consistent trends across all months. As an example, Meteonorm Interpolated and Meteonorm Weather Station datasets, regularly report similar T_L factor values, indicating reliable and consistent data, while, data extracted from the SoDa dataset has more fluctuations, with some months showing higher values compared to other sources. The obtained monthly values are utilized as primary values to calculate averages for specific periods, including seasonal intervals and the entire year.

The average for the winter season is determined by using values from November to February, while the average for the summer season is computed using values from May to August. The average value for spring and autumn is found by calculating the median of the values from September, October, March, and April. In addition, an annual average value is computed to indicate the overall mean value across all months. The computed seasonal and annual averages are shown in Table 7.

Table 7 - Aggregated Linke Turbidity factor values for the city of Turin

Season	**Source**						
	QGIS (city)	Fracastoro et al.	Meteonorm Weather station	Meteonorm Aeronet	Meteonorm Interpolated	Meteonorm w/o	SoDa
Winter	3.17	4.15	2.69	3.08	2.71	2.50	3.48
Spring/Autumn	3.77	4.12	3.40	4.21	3.43	3.16	4.38
Summer	4.3	4.52	3.61	4.29	3.64	3.36	4.47
Yearly average	3.75	4.26	3.23	3.86	3.26	3.01	4.11

For the summer, the values show the highest turbidity, ranging from 3.36 to 4.52. Fracastoro et al. report the greatest value again, while the Meteonorm W/O dataset, shows the lowest. During this season, the majority of sources indicate that the values are around 4.0, which suggests a substantial increase in turbidity compared to previous seasons.

Considering the annual average, the values range from 3.01 to 4.26. The yearly data presents a comprehensive overview of general atmospheric conditions. Similar to monthly average values, Fracastoro et al. report the highest annual average, suggesting a consistently higher perception of turbidity, while Meteonorm W/O reports the lowest, indicating clearer overall conditions. The yearly averages show moderate turbidity with a slight inclination towards higher values, reflecting the combined seasonal effects.

Overall, the data reveals clear seasonal variations in atmospheric turbidity for Turin. The lowest values are generally observed in winter, with a gradual increase through spring and autumn, peaking in summer months. This seasonal trend is consistent across most sources, highlighting the impact of seasonal changes on atmospheric clarity.

Overall, it is evident that the sources generally exhibit a trend of increasing turbidity from winter to summer. However, the specific values are not equal, highlighting the importance of using multiple data sources for a better analysis. Comparing monthly and aggregated values, differences are evident. Aggregated seasonal values show a difference of 3.2% to 7.0% across different sources. The difference between aggregated yearly and monthly values ranges from 5.3% to 13.5% across sources. Notably, values sourced from the Fracastoro et al. show only a 1.2% difference between aggregated seasonal and yearly values, indicating lower fluctuations compared to other sources.

4.2.3 - Diffuse to Global Radiation Ratio

To determine the diffuse to global radiation (DG) ratio for the Turin study region, numerous sources, such as the datasets given by the Meteonorm software and the PVGIS dataset, are utilized.
Meteonorm software provides three unique setups for Turin, resulting in three separate results for the DG ratio, thereby demonstrating the contribution of totally four distinct sources to the dataset.
The utilization of monthly data-gathering methodologies is done to reach the highest possible temporal resolution that is yet practical.

Through the utilization of ground station data recording, the Meteonorm software enables the calculation of the DG ratio.The information for these measurements comes from the meteorological stations that are situated in the neighbourhood of Maddalena Hill (Figure 16) and at Turin Airport (Caselle Torinese, TO).
The values that are available in the PVGIS dataset are also taken into consideration during the analysis processes. The exact location which is picked in order to access the PVGIS database and extract the relevant data, is situated at a latitude of 45.097 degrees and a longitude of 7.710 degrees, which is located in Corso Taranto in the study area (Figure 18).

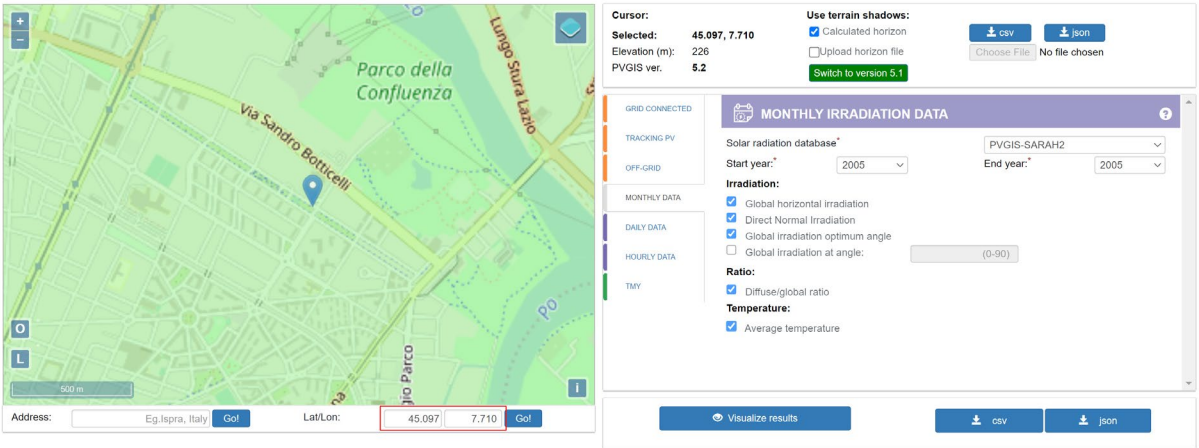

Figure 18 - Selected location in PVGIS platform to extracting data

The DG ratio values for the city of Turin are presented in Table 8. These values are obtained specifically for the purpose of this study.

Table 8 - DG ratio values extracted from the sources for the city of Turin

Month	Source			
	PVGIS	Meteonorm W/O	Meteonorm Interpolated	Meteonorm weather station
January	0.39	0.16	0.19	0.17
February	0.41	0.21	0.23	0.23
March	0.39	0.17	0.19	0.19
April	0.40	0.17	0.20	0.19
May	0.42	0.16	0.18	0.18
June	0.38	0.18	0.20	0.20
July	0.35	0.15	0.18	0.17
August	0.37	0.18	0.21	0.20
September	0.41	0.14	0.16	0.16
October	0.48	0.19	0.22	0.21
November	0.47	0.17	0.21	0.20
December	0.40	0.19	0.22	0.20

In addition, these numerical values are shown in Figure 19 to provide a visual representation of the findings and facilitate a better understanding.

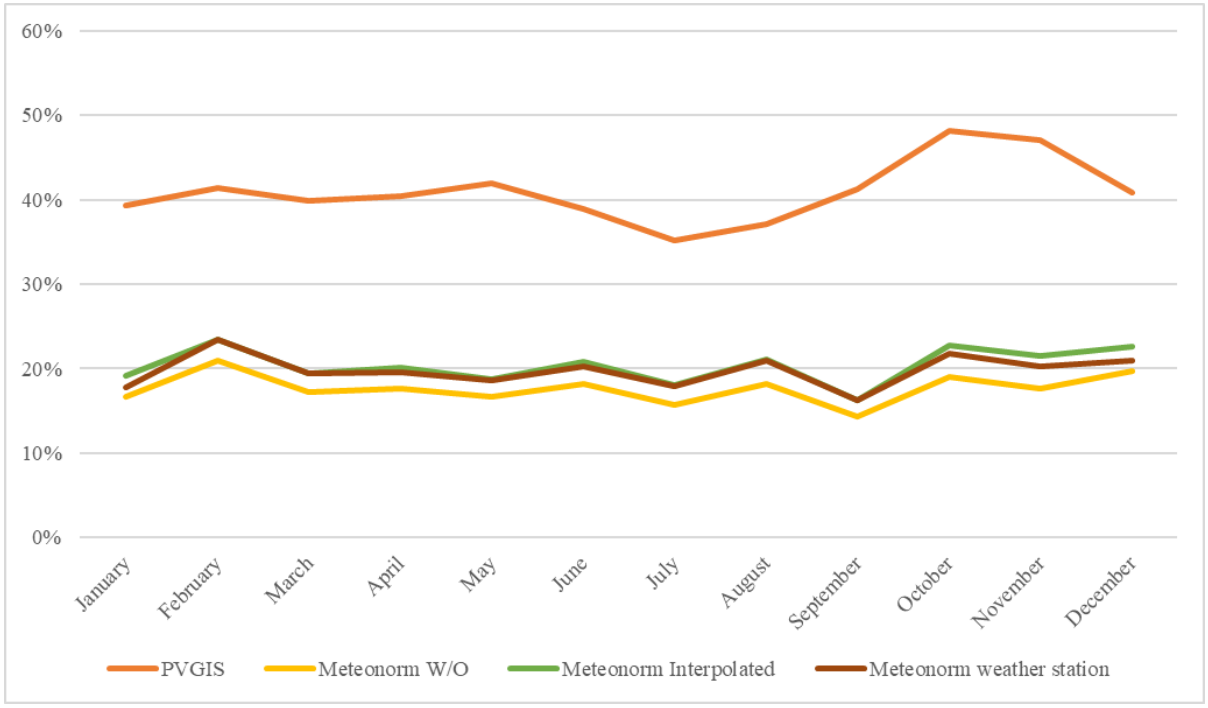

Figure 19 - Monthly values of Diffuse to Global radiation ratio for the city of Turin

According to Table 8 and Figure 19, the months of summer tend to exhibit lower levels of diffuse radiation in comparison to global radiation, whereas the months of winter exhibit significantly higher levels throughout the winter months. Analyzing the trends reveals a mixed pattern across the months. Generally, the DG ratio tends to decrease from January to June, and from July to October, it has a tendency to increase. However, the magnitude of these changes varies across the data sources. Additionally, although the values of the DG ratio from PVGIS appear to be consistently greater than those from the Meteonorm datasets, the trends of both datasets are almost the same, which indicates that the DG ratio can be measured with a high level of accuracy.

However, there are some discrepancies with the values provided by the DG Meteonorm, which can be regarded as a hint to the possibility of inaccuracy under certain meteorological conditions. To calculate the averages for specific periods such as seasonal intervals and the entire year, the collected monthly

DG ratio values served as the primary data. The readings from November to February are utilized to compute the average for the winter season, while those from May to August form the basis for the summer season average. For Spring/Autumn, the average is derived by computing the median of the numbers from September, October, March, and April. Additionally, an annual average value is generated to indicate the overall average value across all months. The results of these computations for the seasonal and annual averages are shown in Table 9.

Table 9 - Aggregated DG ratio values for the city of Turin

Season	Source			
	PVGIS	Meteonorm W/O	Meteonorm Interpolated	Meteonorm weather station
Winter	0.42	0.18	0.21	0.20
Spring/Autumn	0.42	0.17	0.19	0.19
Summer	0.38	0.17	0.19	0.19
Yearly average	0.40	0.17	0.20	0.19

There are noticeable shifts in the seasonal and yearly values of the DG Ratio across all datasets, as shown in Table 9. The winter season shows considerable variation in the DG Ratio depending on the dataset, while in the summer, the range of values narrows slightly. The Spring/Autumn season also reflects this pattern.

These results indicate seasonal differences in DG ratios, with winter months often having higher values than summer months. The variation in DG Ratio values across datasets underscores the influence of regional weather data on the precision of solar radiation estimation.

4.3 - Solar Radiation Calculation

In this section, the focus shifts from data extraction to the application and testing of solar radiation calculation methodologies. The comprehensive data gathered from various sources are used as a robust foundation for the analysis.

Diverse combinations of DG ratios and T_L factors are created to evaluate the influence of different input parameters on solar radiation outcomes. This systematic approach allows for a detailed examination of how regional weather variations and data precision impact the accuracy of solar radiation estimations. Each combination is replicated across yearly, seasonal, and monthly configurations, ensuring a thorough investigation of solar irradiation patterns.

The subsequent test plans, elaborations, and calculations are designed to shed light on the optimal conditions and parameters for accurate solar radiation estimation, ultimately contributing to more efficient urban energy planning in the city of Turin.

4.3.1 - Test Plan Definition

Following the extraction of the necessary data, the subsequent phase involved creating various combinations of datasets from the extracted values to evaluate the influence of different inputs on the outcomes.

Specifically, the analysis is based on seven distinct T_L factor values and four DG ratio values, all meticulously extracted from the available sources. These diverse values are used to create 28 possible input combinations, ensuring a comprehensive examination of potential scenarios. Each combination provides a unique set of conditions under which the solar radiation calculations can be tested, offering insights into how each variable influences the results.

The development of these combinations is detailed in Table 10 which outlines the specific configurations used in the study.

Table 10 - Sequential numbering of test plans with specified DG ratio and Linke Turbidity Factor values

Number	DG ratio Source	TL Source
1	Meteonorm w/o	Meteonorm w/o
2		Meteonorm weather station
3		Meteonorm interpolated
4		QGIS (city)
5		Meteonorm Aeronet (Ispra)
6		SoDa
7		Fracastoro et al.
8	Meteonorm weather station	Meteonorm w/o
9		Meteonorm weather station
10		Meteonorm interpolated
11		QGIS (city)
12		Meteonorm Aeronet (Ispra)
13		SoDa
14		Fracastoro et al.
15	Meteonorm interpolated	Meteonorm w/o
16		Meteonorm weather station
17		Meteonorm interpolated
18		QGIS (city)
19		Meteonorm Aeronet (Ispra)
20		SoDa
21		TL_Fracastoro et al.
22	PVGIS	Meteonorm w/o
23		Meteonorm weather station
24		Meteonorm interpolated
25		QGIS (city)
26		Meteonorm Aeronet (Ispra)
27		SoDa
28		Fracastoro et al.

Each combination is replicated with yearly, seasonal, and monthly input, resulting in 84 series of elaborations and 1008 monthly values. To better understand how variations in the input data influence the results, the values in the series were sorted in ascending order by the DG ratio values and then by the T_L factor, making it easier to recognize any emerging patterns.

4.3.2 - Yearly Solar Irradiation

The average yearly solar irradiation for each of the four buildings is determined using the yearly average, seasonal average, and monthly values presented in tables 6 to 9, and the aggregated results' median values for the buildings are demonstrated in Figure 20. In order to cover all planning scenarios, the estimation process was conducted across 28 plans for the intervention periods, totalling 84 calculations.

During the initial computation process, a single set of average yearly values is considered for each testing plan, as input parameters across all months. Following this step, the calculating procedure is repeated, however, this time the computed seasonal average values are used as the main inputs for the estimation process. For each testing plan, this strategy requires the utilization of a constant set of parameters throughout the months that reflect each season. Lastly, the monthly values are taken into account as the inputs for calculating the solar irradiation of each building. The medians of the findings assigned to each test plan are visualized in Figures 21 to 24 for better comprehension.

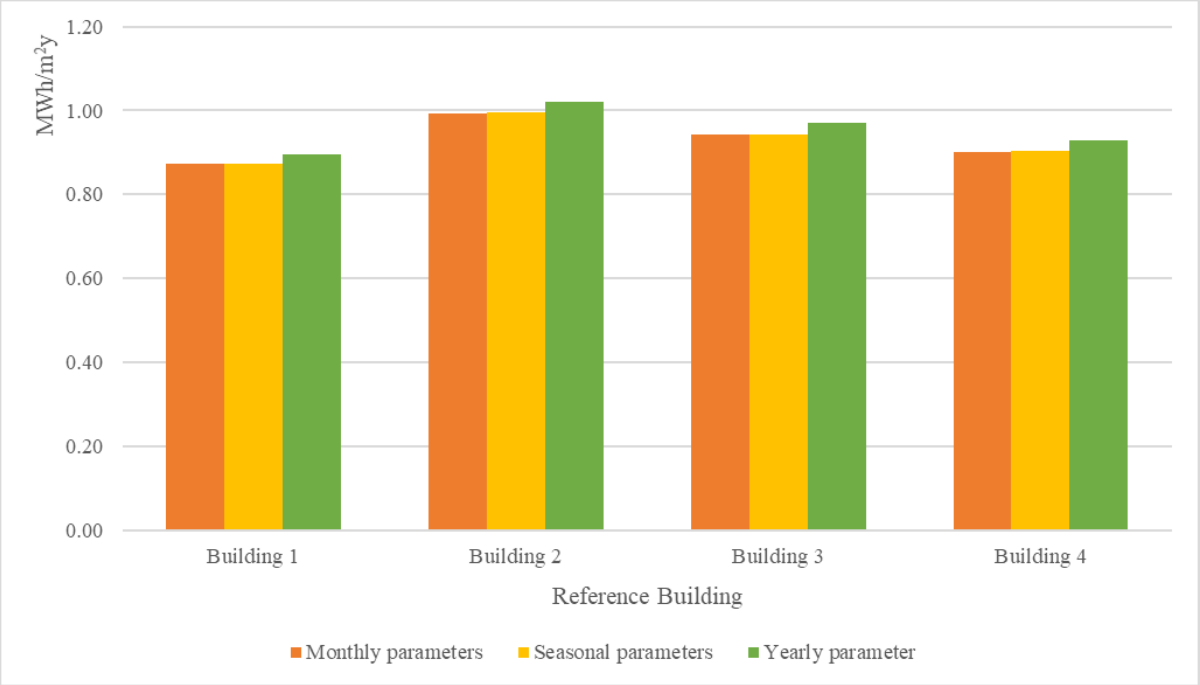

Figure 20 - Median Yearly solar irradiation for Each Building

According to Figure 20, it is evident for the four selected buildings in this research, that using yearly parameters as inputs for solar irradiation calculation results in a higher amount of solar irradiation than seasonal parameters, which in turn results in higher values than monthly parameters.
Further explorations reveal that for all buildings, the median of estimated solar irradiation using aggregated yearly parameters shows a +2.80% increase on average, compared to the results obtained using monthly parameters, which is greater than the difference between using aggregated seasonal parameters and monthly parameters, which is only +0.16% on average.

Based on the findings, the building 2 is the one that receives the maximum annual solar irradiation among the buildings that were selected. This is attributed to its optimal orientation, specifically with one of its pitches facing South-West, which maximizes exposure to afternoon solar radiation. This results in an annual average solar irradiation of 1.00 MWh/m² for the building 2.
On the other hand, the building 1, which is oriented in a north-south direction, benefits from the least amount of annual solar irradiation of all the structures that were investigated, with an average of 0.88 MWh/m^2.

The building 3 and building 4 exhibit intermediate levels of annual solar irradiation. The building 3 benefits from morning solar radiation, resulting in an average of 0.95 MWh/m² annually.
On the other hand, the building 4 benefits from the complex geometry of its roof, ensuring continuous exposure to solar radiation throughout the day, with an average annual solar irradiation of 0.91 MWh/m².

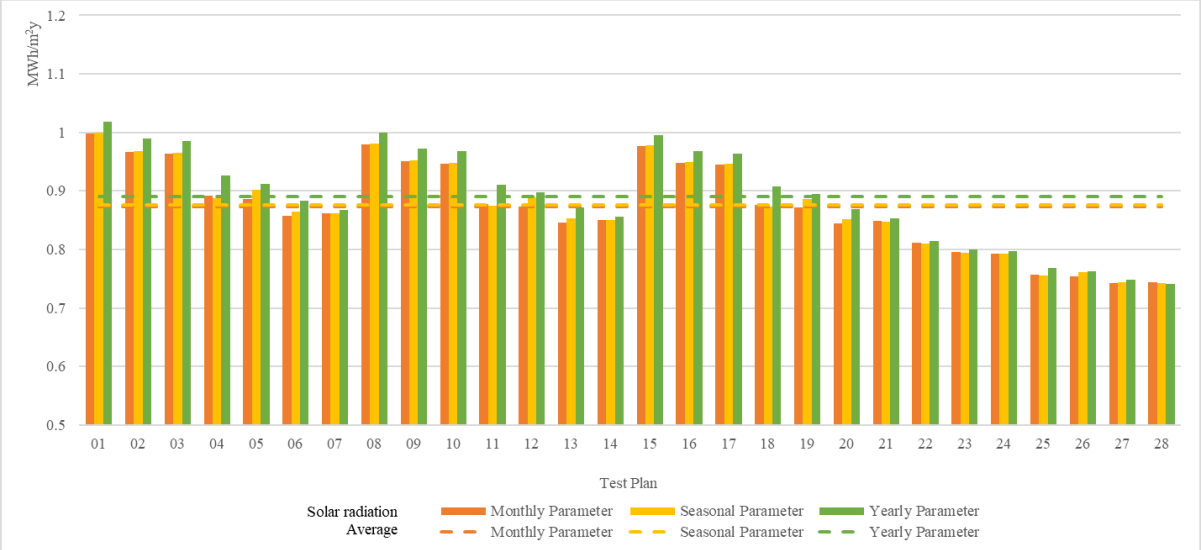

Figure 21 - Median solar irradiation on building 1, differentiated by input level of aggregation

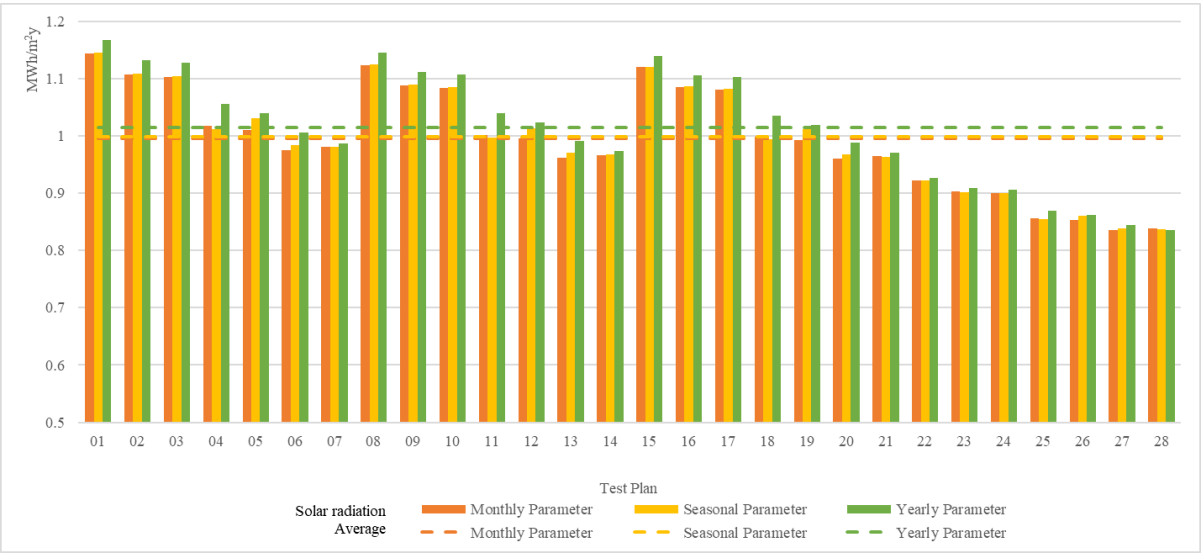

Figure 22 - Median solar irradiation on building 2, differentiated by input level of aggregation

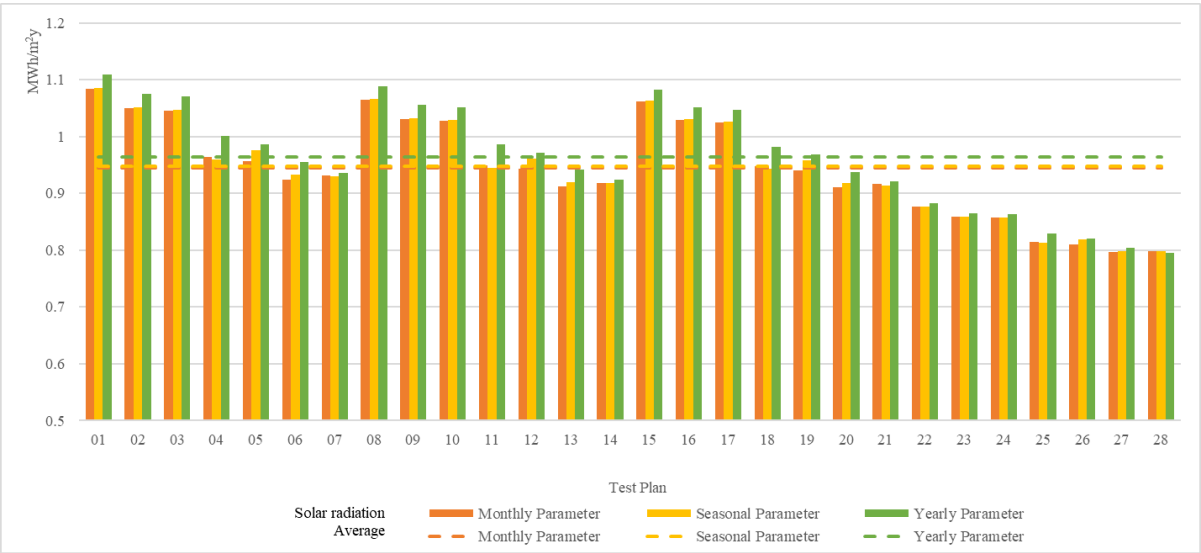

Figure 23 - Median solar irradiation on building 3, differentiated by input level of aggregation

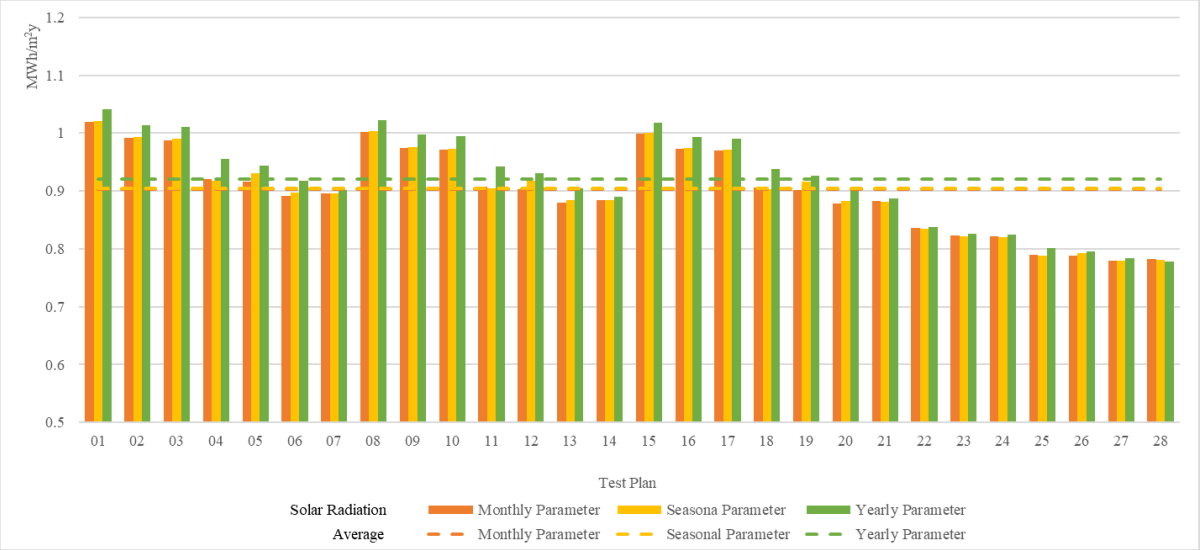

Figure 24 - Median solar irradiation on building 4, differentiated by input level of aggregation

Figures 21 to 24, demonstrate the medians of the results assigned to each plan of test, as well as the average of yearly solar irradiation - in dashed lines - received by the building estimated by monthly, aggregated seasonal and yearly input values.

A recognizable pattern appears as a result of the analysis of the data that is collected, which encompasses a similar trend for the buildings. Over a large range, there is a consistent pattern of decreasing irradiation levels observed across the series of plans. This pattern aligns with the expected logic, attributed to rising turbidity values indicating increased haze in the atmosphere, and larger DG ratios indicating greater diffusion of solar radiation. In particular, this pattern demonstrates a steady decline beginning with Plan 01 and continuing all the way to Plan 07. After this, there is a significant increase, and then the fall occurs again, beginning with Plan 08 and continuing through Plan 14. Consequently, following an upward movement, the trend maintains its downward track from Plan 15 all the way through Plan 21. Specifically, the decrease in irradiation levels exhibits a significantly smoother trajectory among the subset that covers plans 22 through 28.

Regarding the results corresponding to each building, the solar irradiation tests values assigned to plans 22 to 28, where the DG ratio is gathered from PVGIS dataset, often show lower values in comparison to other plans, while plans 01 to 07, which use the DG ratio offered by Meteonorm W/O dataset, frequently have elevated values.

Overall, Plan 01, using the yearly values as inputs for the building 2 shows the highest yearly average solar irradiation at 1.15 MWh/m², and Plan 28, using the yearly values as inputs for the building 1 shows the lowest average solar irradiation at 0.74 MWh/m².

Analyzing the differences between achieved results reveals variations and the impact of inputs on outcomes, quantified as percentages. The difference between the results are shown in the Table 11.

Table 11 - Percentage difference of the results for each building

Building	**The difference compared to median of outcomes using monthly parameters (%)**	
	Median of outcomes using yearly parameters	Median of outcomes using seasonal parameters
Building 1	+2.8	+0.21
Building 2	+2.7	+0.12
Building 3	+2.9	+0.17
Building 4	+2.9	+0.15

According to Table 11, across all 28 plans, the building 1 demonstrates an average difference of +2.8% with yearly values and +0.21% with seasonal values, both compared to results derived from monthly values. Similarly, for the building 2, the differences are +2.7% and +0.12%, though, for the building 3, the differences are +2.9% and +0.17% in the same order; and regarding the building 4, the differences are +2.9% and +0.15%, respectively.
The comparative analysis shows that the building 2 has relatively smaller variances in outcomes. On the other hand, the building 1 is more sensitive to input changes, resulting in a more significant fluctuation compared to other buildings.

4.3.3 - Monthly Solar Irradiation

To enhance the insights into the impact of parameters on the obtained results, the monthly solar irradiation median values used for calculating the average yearly solar irradiation (Section 4.3.2 -) have been assessed.

4.3.3.1 - *Median Outcomes*

This step involved a thorough investigation of the median results using yearly, seasonal, and monthly parameters for plans 01 and 28, which have the lowest and highest DG ratio and T_L factor, respectively. This analysis was conducted across all four buildings in the study.By focusing on these specific plans, the full range of potential variations in solar radiation estimates was explored, providing a detailed comparison of how different input values affect the outcomes.
Figures 25 to 28 present the elaborations for buildings under test plans 01 and 28, utilizing the three input configuration.

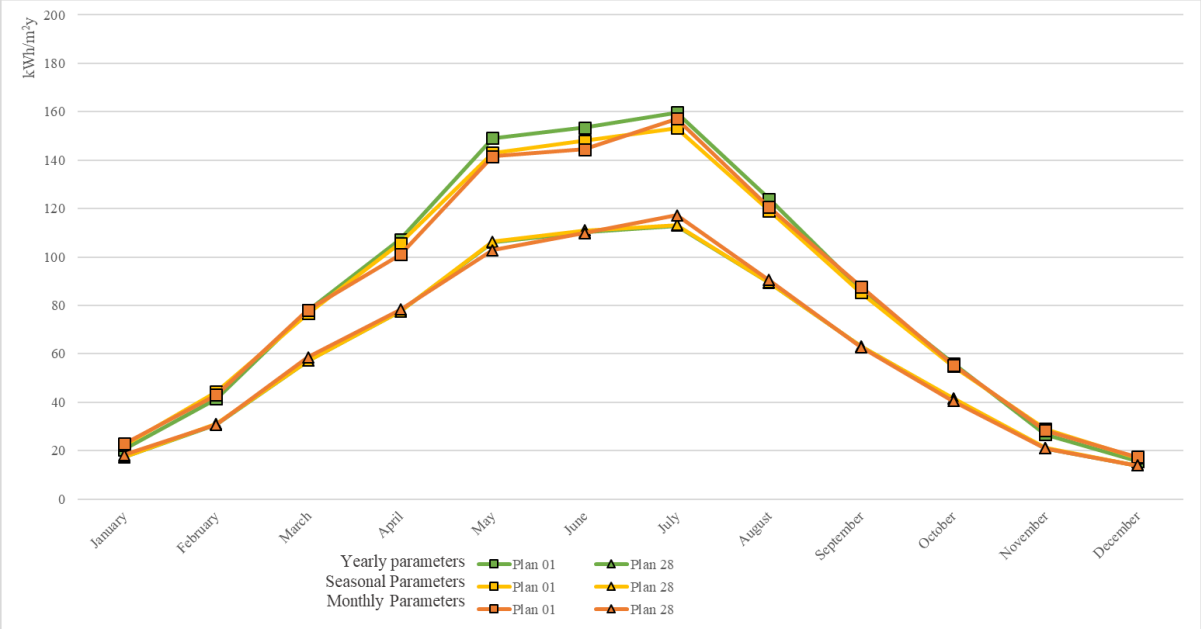

Figure 25 - Monthly solar irradiation calculated for building 1 regarding plans 01 and 28

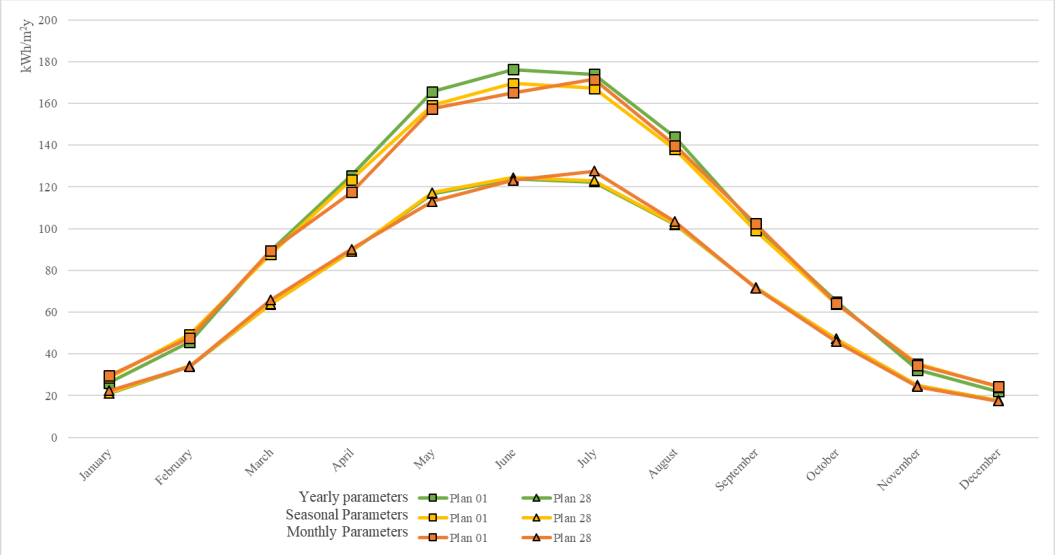

Figure 26 - Monthly solar irradiation calculated for building 2 regarding plans 01 and 28

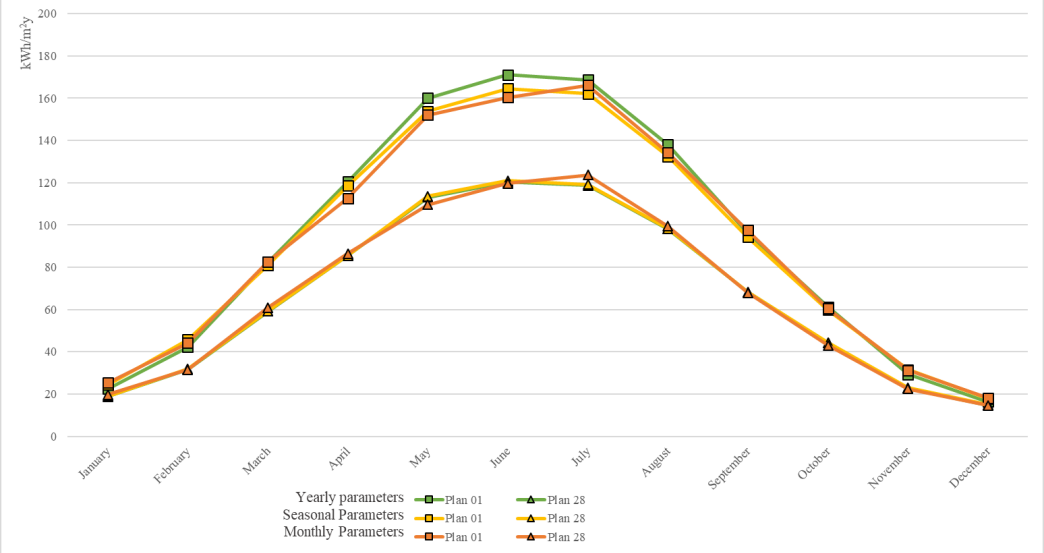

Figure 27 - Monthly solar irradiation calculated for building 3 regarding plans 01 and 28

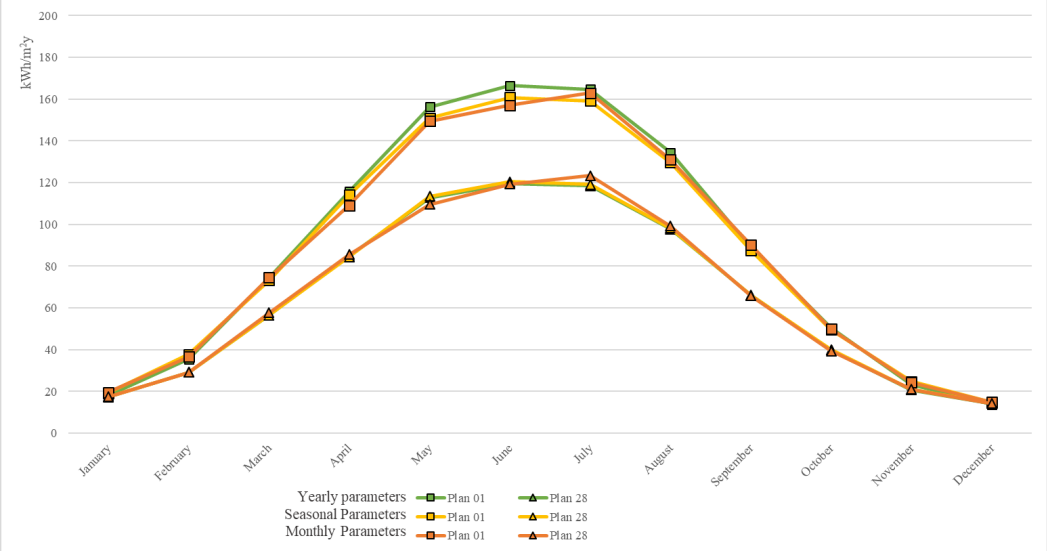

Figure 28 - Monthly solar irradiation calculated for building 4 regarding plans 01 and 28

According to Figures 25 to 28, the result lines generally shift downward from plan 01 to plan 28 with three sets of parameters (yearly, seasonal, and monthly).
This downward shift indicates a consistent trend where the results decrease as the DG ratio and T_L factor increase. Furthermore, the differences are more significant in summer months, when the radiation estimation values are higher.
Given that the variation in monthly solar radiation results for each building varies across months, comparing the scale of the differences as a percentage shows the effect of inputs on the outcome (Table 12).

Table 12 - Percentage Differences in Outcomes for Plans 01 and 28 Across Monthly, Seasonal, and Yearly Parameters for Each Building

Building	Input Parameter	Results difference (%)												
		January	February	March	April	May	June	July	August	September	October	November	December	Average
Building 1	yearly	18.23	34.38	36.68	38.10	40.59	39.15	41.43	38.83	37.38	35.23	27.79	13.46	33.44
	Seasonal	27.54	43.38	34.34	36.46	34.58	33.48	35.35	33.18	35.36	32.32	36.95	22.66	33.80
	monthly	25.59	39.90	33.08	28.98	37.75	31.52	33.98	33.31	40.06	36.94	35.16	25.61	33.49
Building 2	yearly	23.61	33.93	40.03	40.60	41.74	42.34	42.17	41.12	40.51	38.07	30.22	24.91	36.61
	Seasonal	34.00	44.38	37.30	38.66	35.66	36.22	36.05	35.06	38.11	35.12	41.31	35.81	37.31
	monthly	32.18	40.36	35.91	30.28	39.27	34.16	34.46	35.27	43.27	39.92	42.00	40.29	37.28
Building 3	yearly	19.71	32.70	39.34	40.73	41.44	42.18	42.04	40.72	40.78	38.65	28.74	10.43	34.79
	Seasonal	29.08	43.50	36.59	38.67	35.41	36.10	35.91	34.63	38.36	34.70	37.63	19.28	34.99
	monthly	28.28	39.97	35.53	30.23	38.90	34.03	34.34	34.91	43.55	40.49	39.46	23.96	35.30
Building 4	yearly	3.04	21.63	31.75	36.49	38.46	39.25	39.12	37.48	34.35	26.28	11.47	3.82	26.29
	Seasonal	9.84	29.14	29.69	35.08	32.90	33.54	33.53	32.02	32.65	23.92	18.38	2.17	26.07
	monthly	12.81	25.85	29.12	27.66	36.37	31.66	32.11	31.97	36.91	26.84	15.34	4.41	25.92

According to Table 12, across all buildings studied, the results show variations in solar irradiation values between plan 01 and plan 28. The percentage differences in outcomes for plans 01 and 28 are calculated across monthly, seasonal, and yearly parameters for each building, determined by comparing the percentage differences between maximum and median outcome values, as well as between median and minimum outcome values. Specifically, for the building 1, plan 01 returns values that are on average 33.6% higher than those of Plan 28. Similarly, the building 2 sees values from plan 01 that are 37.1% higher compared to plan 28. In contrast, the building 3 exhibits an average increase of 35.0% in values from plan 01 compared to plan 28. Lastly, the building 4 shows values from Plan 01 that are on average 26.1% higher than those from Plan 28. More into detail, comparing the results for plans 01 and 28, the building 1 shows a maximum difference of 40.59% in May and a minimum difference of 13.45% in December, both using yearly inputs. For the building 2, the highest difference is 40.51% in October with monthly inputs, while the lowest is 10.42% in December with yearly inputs. In addition, a peak difference of 41.44% is observed for the building 3 during November when monthly inputs are used, while the minimum difference is observed in December when yearly inputs are used. Furthermore, for the building 4, the greatest and smallest differences, 39.11% and 2.16%, are observed in July and December, respectively, both using yearly inputs.

Furthermore, except for five conditions, which correspond to the building 4 - including -3.82% in December with yearly inputs, 2.17% in December with seasonal inputs, 4.41% in December with monthly inputs, 3.04% in January with yearly inputs, and 9.84% in January with seasonal inputs- the all other amount of differences are more than 10%.
Overall, it is noticeable that across all three input settings, differences are minimal during winter when solar radiation is lower, both in terms of percentage change and actual values. However, these differences become more evident during the spring, summer, and autumn months. Another significant contrast is seen in the peak solar radiation period. Generally, using yearly and seasonal inputs, maximum solar radiation occurs in June. In contrast, when using monthly parameters, solar radiation increases from May and reaches a peak in July, with slightly lower values in June.

The next stage involves analyzing the median values of all the plans assigned for each month (Figures 29 to 40) for each building. In the graphs, the results from monthly inputs are categorized based on the DG ratio, indicated by color, and the T_L factor, represented by symbols.

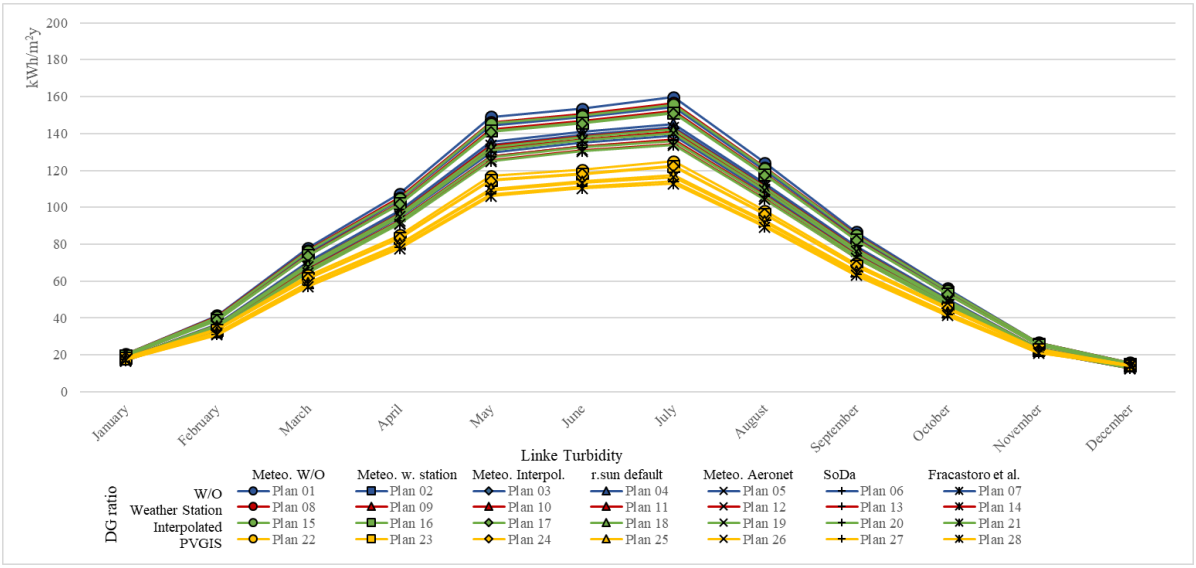

Figure 29 - Comparison of monthly results' median from elaborations with yearly inputs for building 1

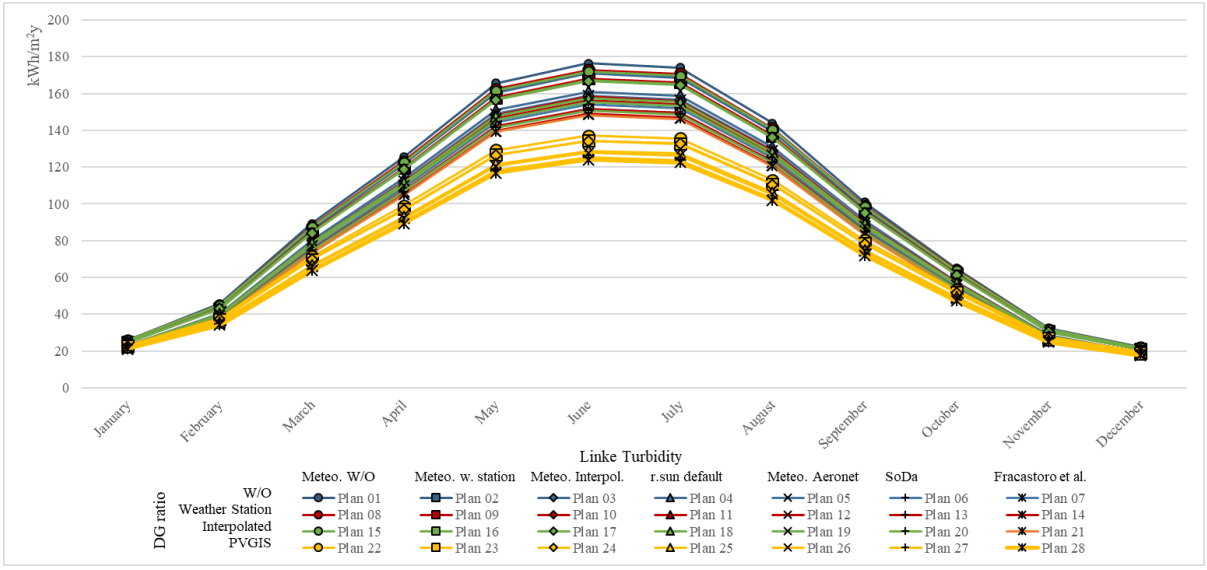

Figure 30 - Comparison of monthly results' median from elaborations with yearly inputs for building 2

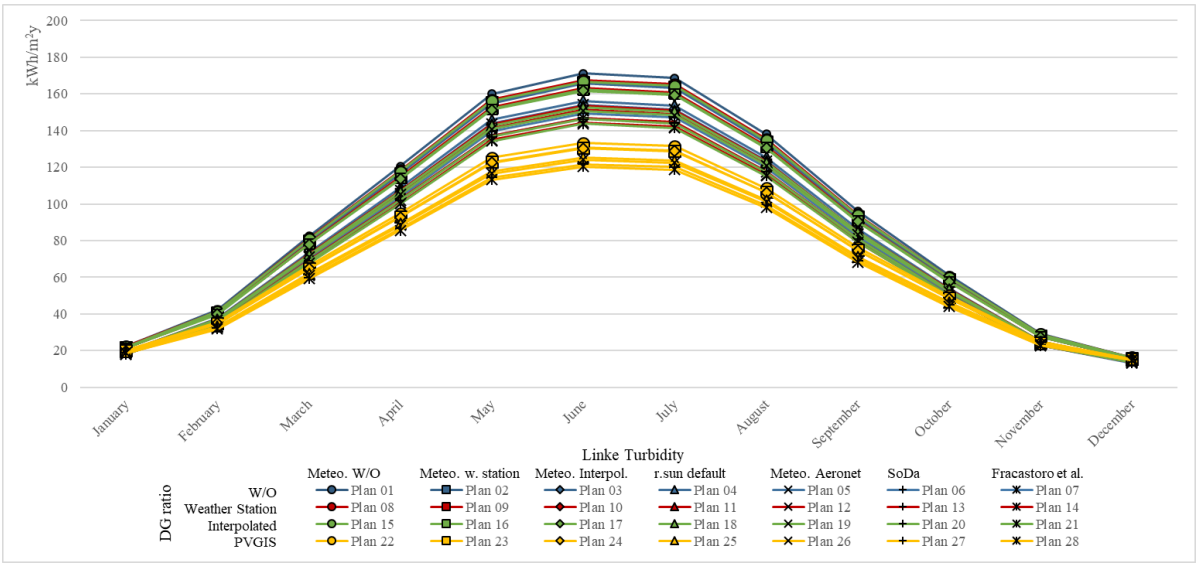

Figure 31 - Comparison of monthly results' median from elaborations with yearly inputs for building 3

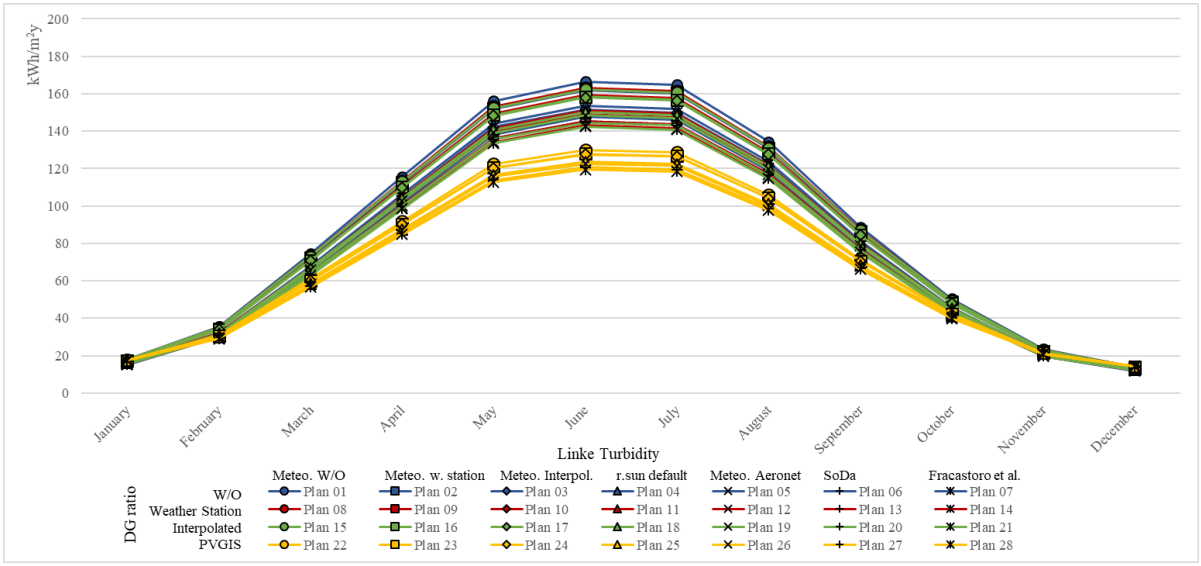

Figure 32 - Comparison of monthly results' median from elaborations with yearly inputs for building 4

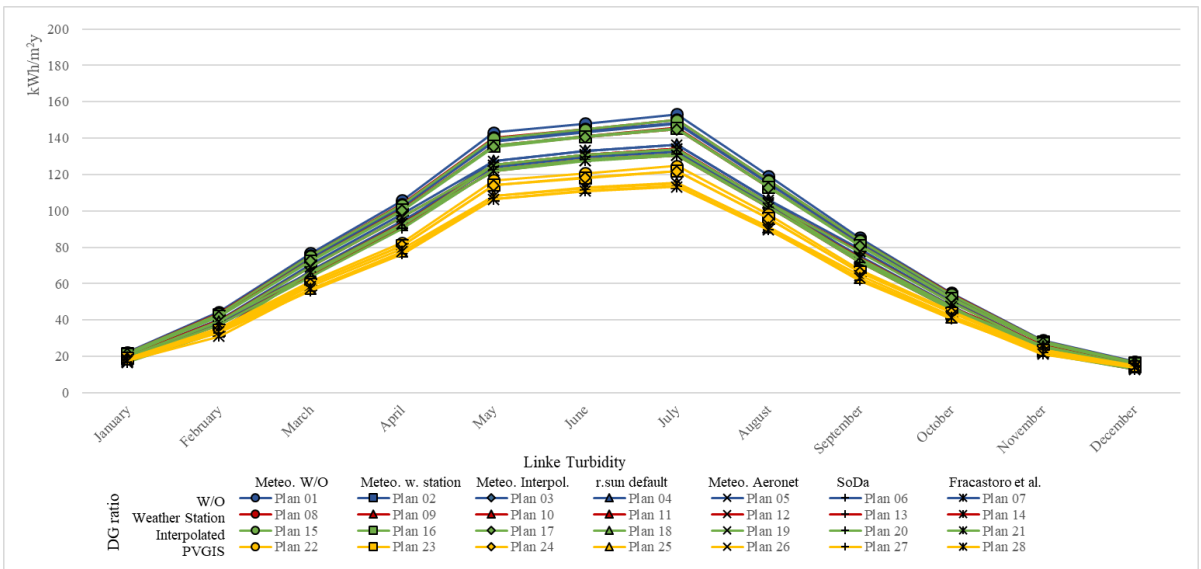

Figure 33 - Comparison of monthly results' median from elaborations with seasonal inputs for building 1

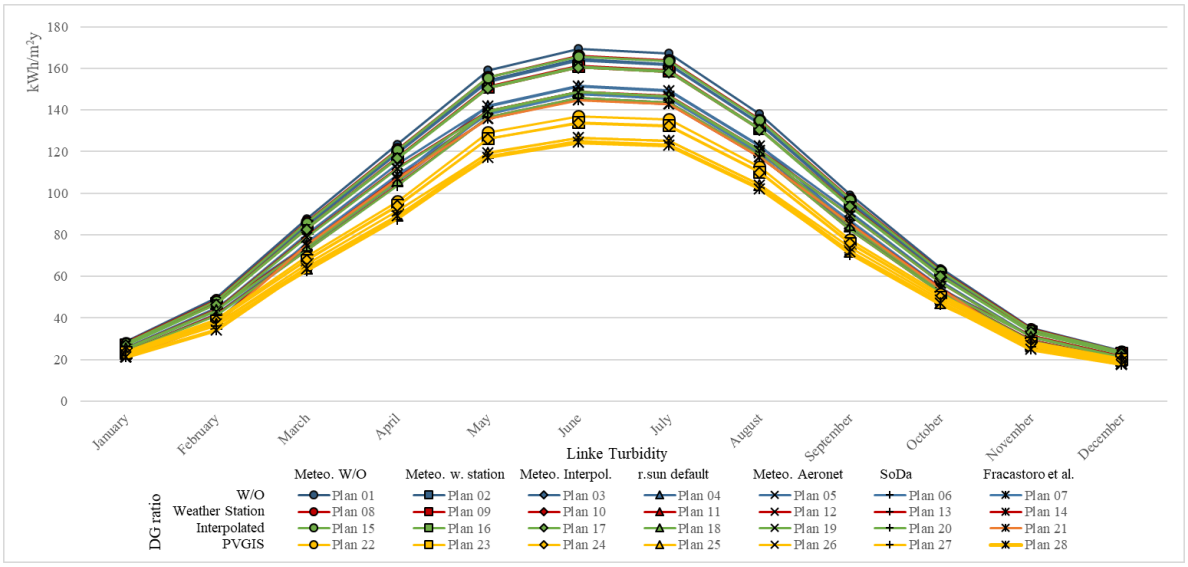

Figure 34 - Comparison of monthly results' median from elaborations with seasonal inputs for building 2

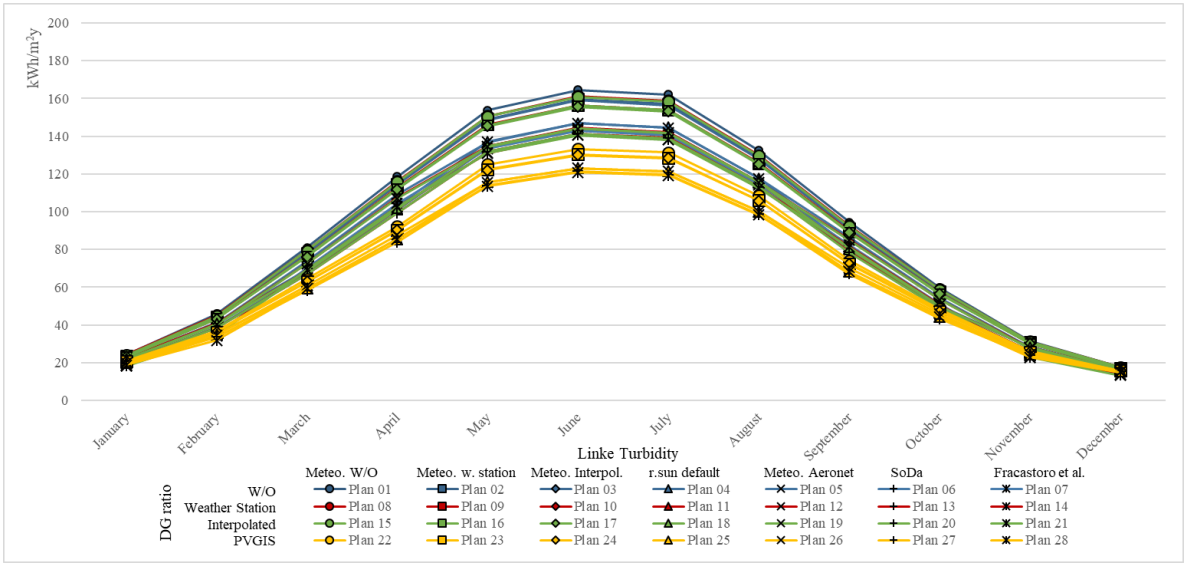

Figure 35 - Comparison of monthly results' median from elaborations with seasonal inputs for building 3

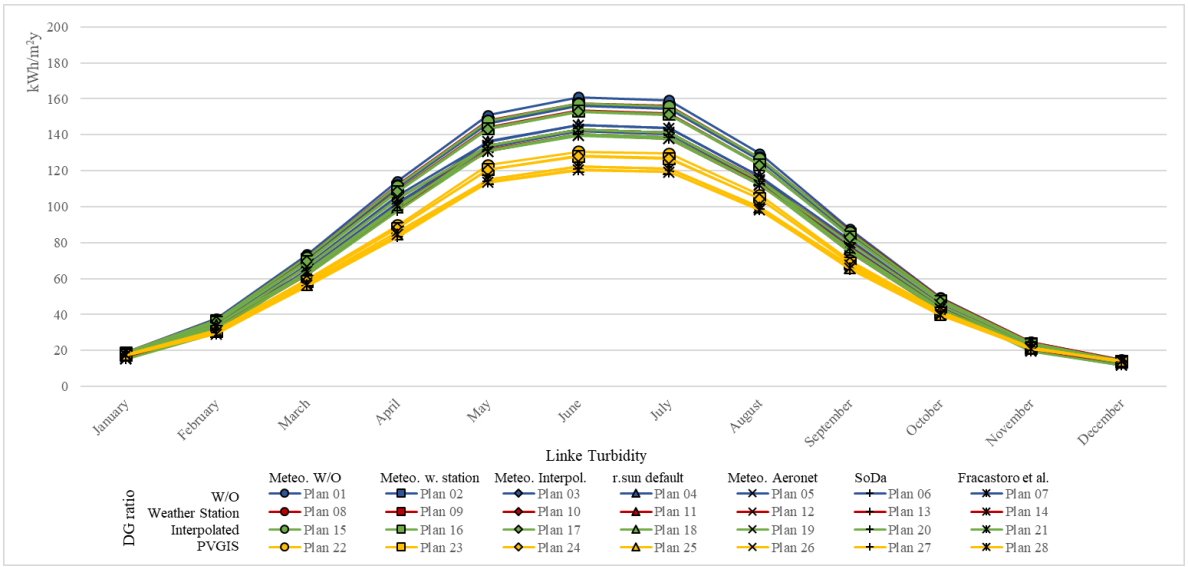

Figure 36 - Comparison of monthly results' median from elaborations with seasonal inputs for building 4

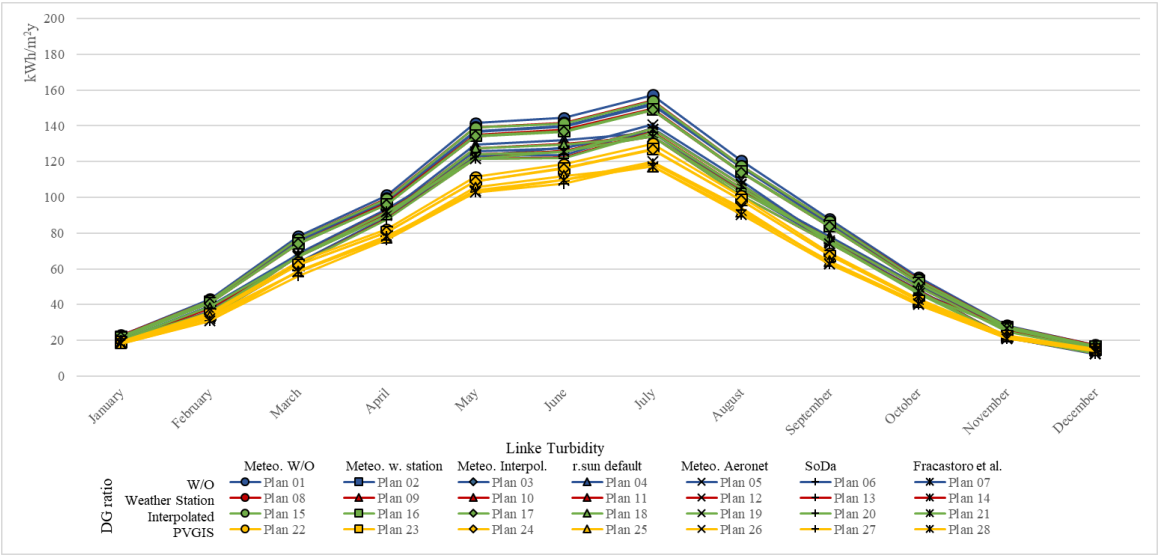

Figure 37 - Comparison of monthly results' median from elaborations with monthly inputs for building 1

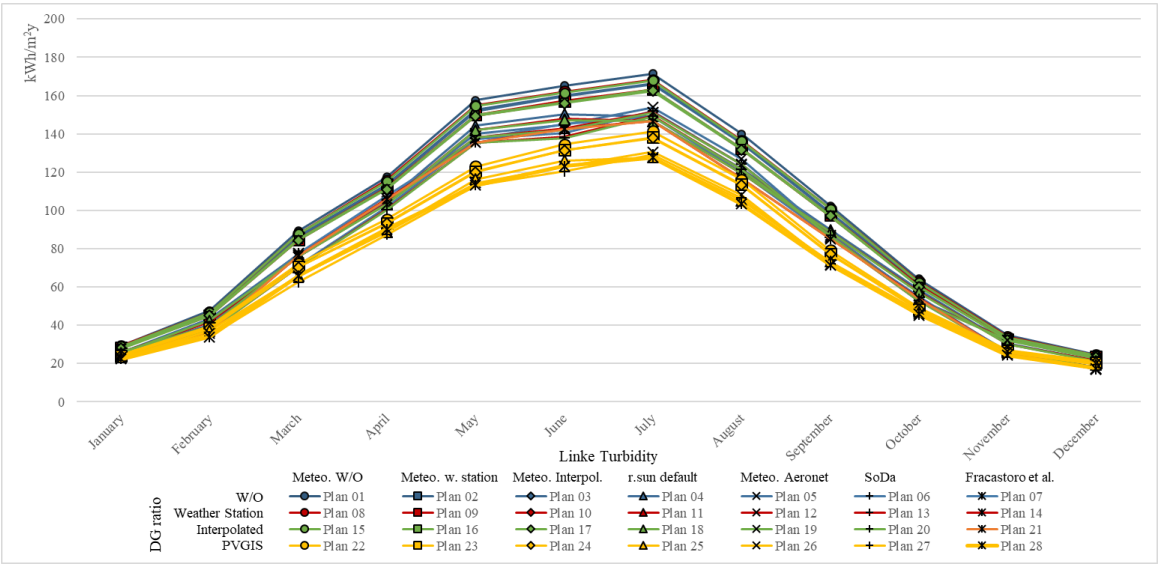

Figure 38 - Comparison of monthly results' median from elaborations with monthly inputs for building 2

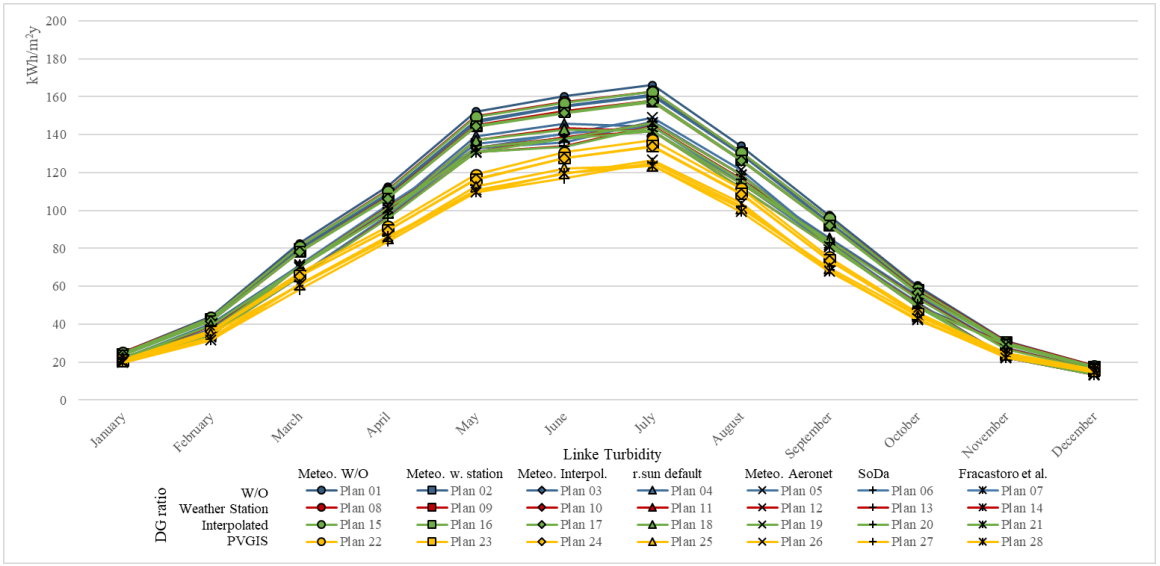

Figure 39 - Comparison of monthly results' median from elaborations with monthly inputs for building 3

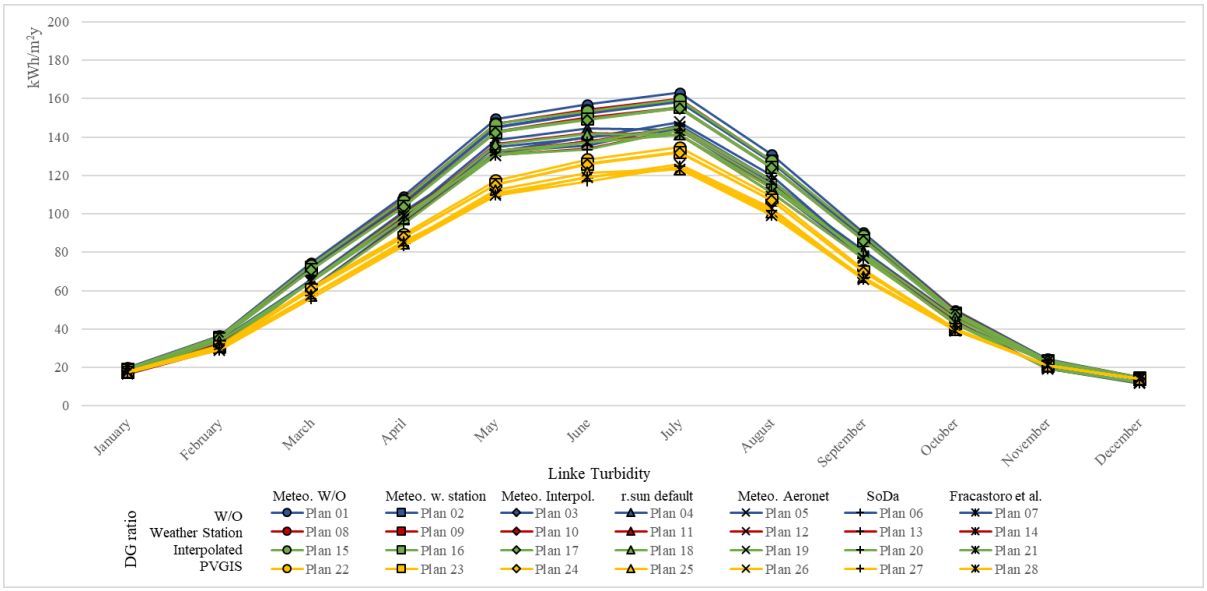

Figure 40 - Comparison of monthly results' median from elaborations with monthly inputs for building 4

The displayed trends in Figures 29 to 40 reveal the general expected pattern that appears across all four buildings when the 28 plans are taken into consideration. Beginning in January, the trends show an increase in the levels of solar radiation, peaks in July, and then followed by a subsequent decrease that continues until December.

Generally, during the summer months, higher levels of solar radiation are estimated, whereas during the winter months, lower levels are seen. This pattern is a reflection of the variation in solar radiation that happens throughout the year.
As a result of the fact that this pattern has been matched consistently throughout all four buildings, the permanence of the seasonal impact in solar radiation that has been detected is brought to light.
Moreover, it is clear that there is a smaller degree of range in the outcomes during the winter months, when the values are lower, whereas the variation is greater during the summer months when the values are larger.
To put it another way, the difference between the results increases as the amount of estimated solar radiation increases. Furthermore, the results assigned to plans 22 to 28, where the DG ratio derived from PVGIS (the highest DG ratio value in this research) typically shows lower values compared to those of other plans, align with the expected logic that larger DG ratios indicate greater diffusion of solar radiation; and plans 01 through 07, on the other hand, which use the DG ratio from Meteonorm W/O (the lowest DG ratio value), often display greater values in comparison.

As for the monthly solar radiation outcomes, the final comparison evaluates all four analyzed buildings. Figure 41 illustrates the median solar radiation for each building throughout the year, along with the average of these medians.

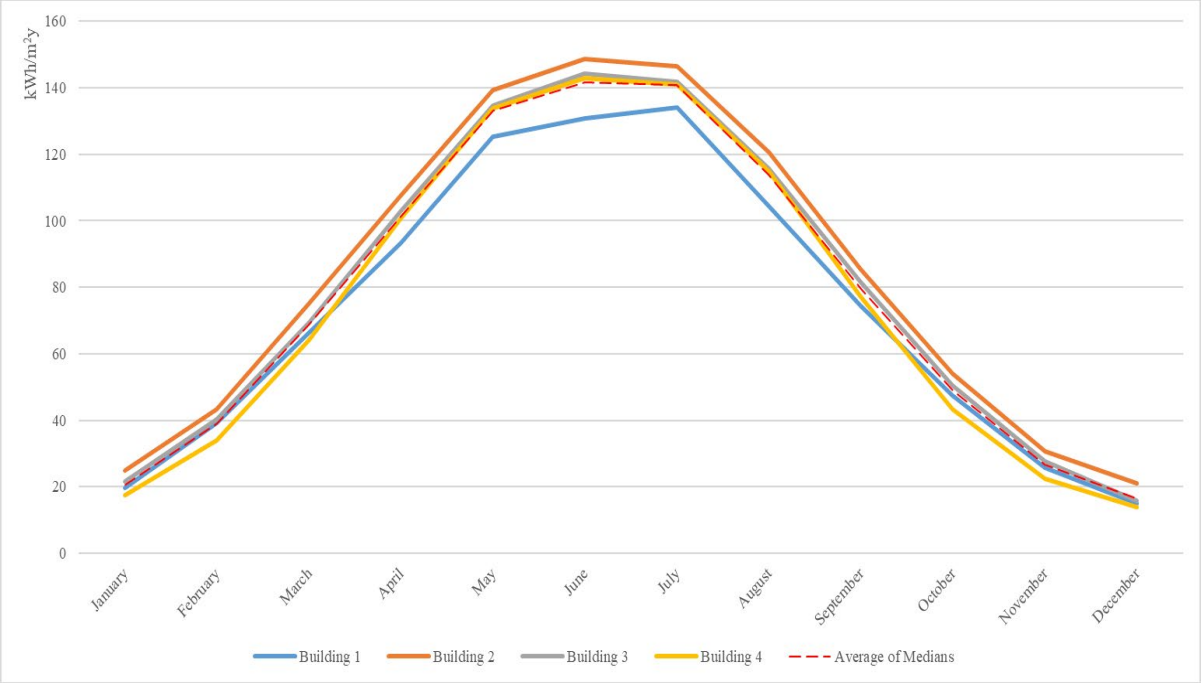

Figure 41 - Monthly median irradiation for the four analyzed buildings

According to Figure 41, the examination of median values across twelve months displays distinct performance patterns among the buildings under study. Specifically, building 1 consistently shows the lowest median values from April to September, indicating a period of relatively lower performance compared to other buildings.

Conversely, building 4 demonstrates lower median values from January to March and October to December.

Throughout the entire year, building 2 consistently exhibits the highest median values across all months, underscoring its favorable orientation compared to the other buildings. Further analysis reveals that the median solar irradiation of building 4 surpasses the average in only four months, where the difference does not exceed 1% compared to the other buildings. Additionally, the overall performance of buildings 2 and 3 remains closely aligned throughout the year.

Building 2 consistently receives the maximum amount of solar radiation every month. On the other hand, building 4 experiences the least amount of solar radiation during the first and last three months of the year, while building 1 absorbs the least amount from April until September.

Moreover, while buildings 2, 3, and 4 experience their highest solar radiation levels in June, building 1 reaches its peak in July.

4.3.3.2 - *Maximum and Minimum Outcomes*

In the next stage, after investigating the median values, the focus shifts to examining the maximum and minimum outcomes. This step aims to determine the variations in solar radiation received by each building throughout the year.

The results are presented as line charts (Figures 42 to 53), showing the maximum and minimum solar irradiation values for each month. This analysis reveals the range of solar exposure and highlights the months with significant fluctuations, offering a clearer picture of each building's solar performance under different conditions.

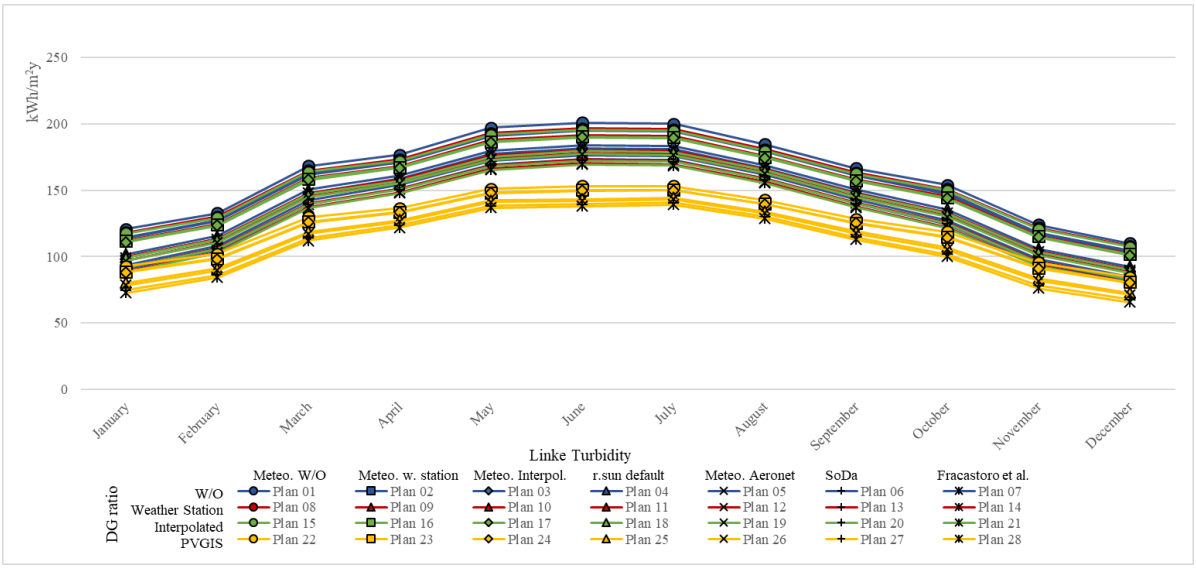

Figure 42 - Comparison of monthly results' maximum from elaborations with yearly inputs for building 1

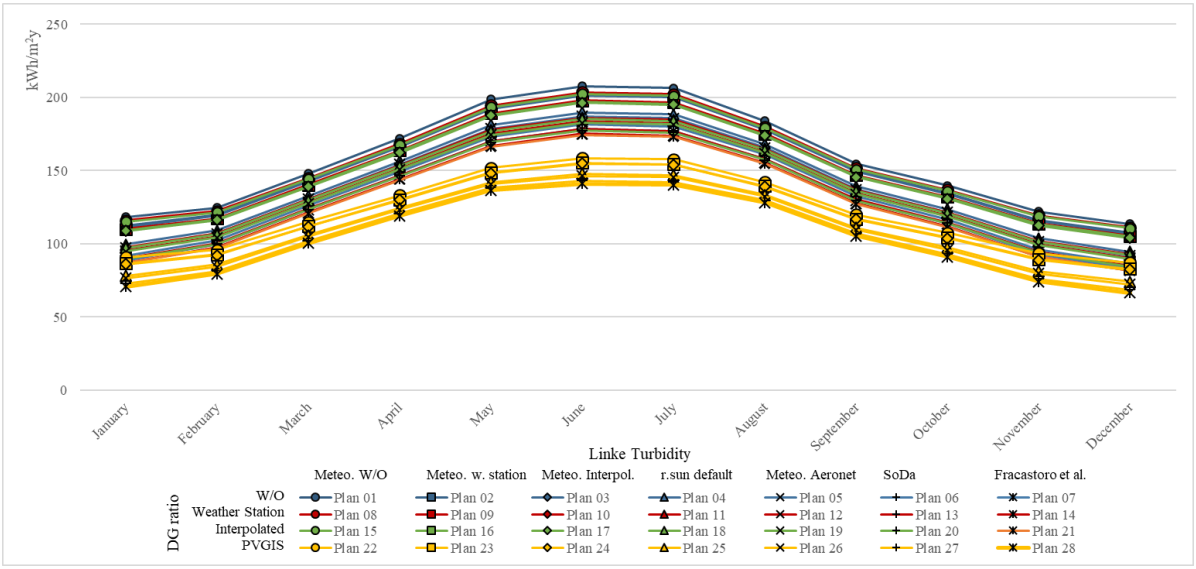

Figure 43 - Comparison of monthly results' maximum from elaborations with yearly inputs for building 2

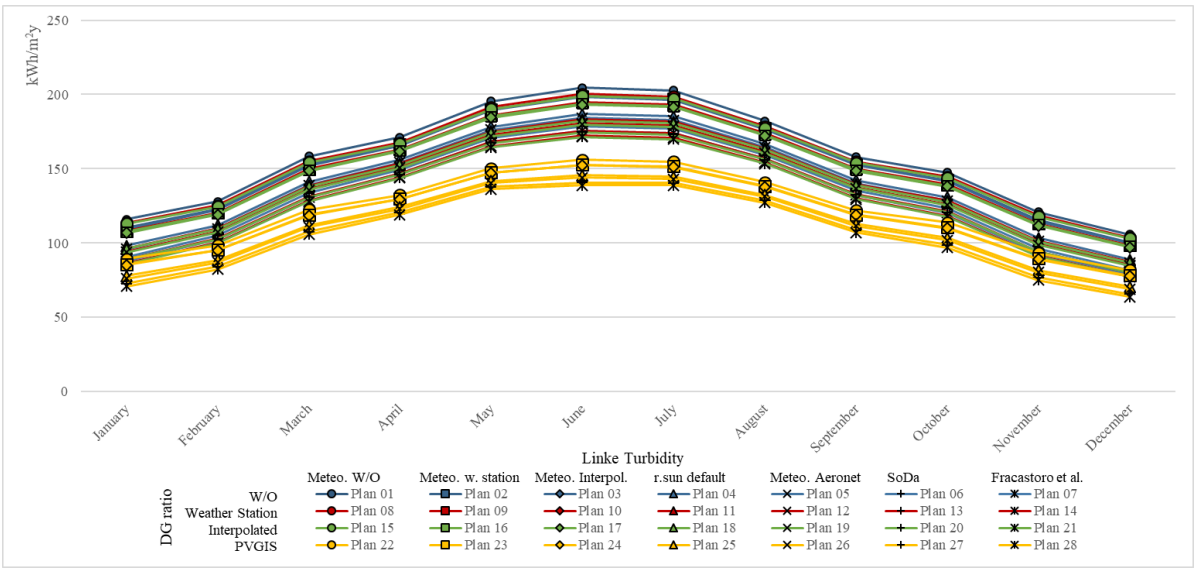

Figure 44 - Comparison of monthly results' maximum from elaborations with yearly inputs for building 3

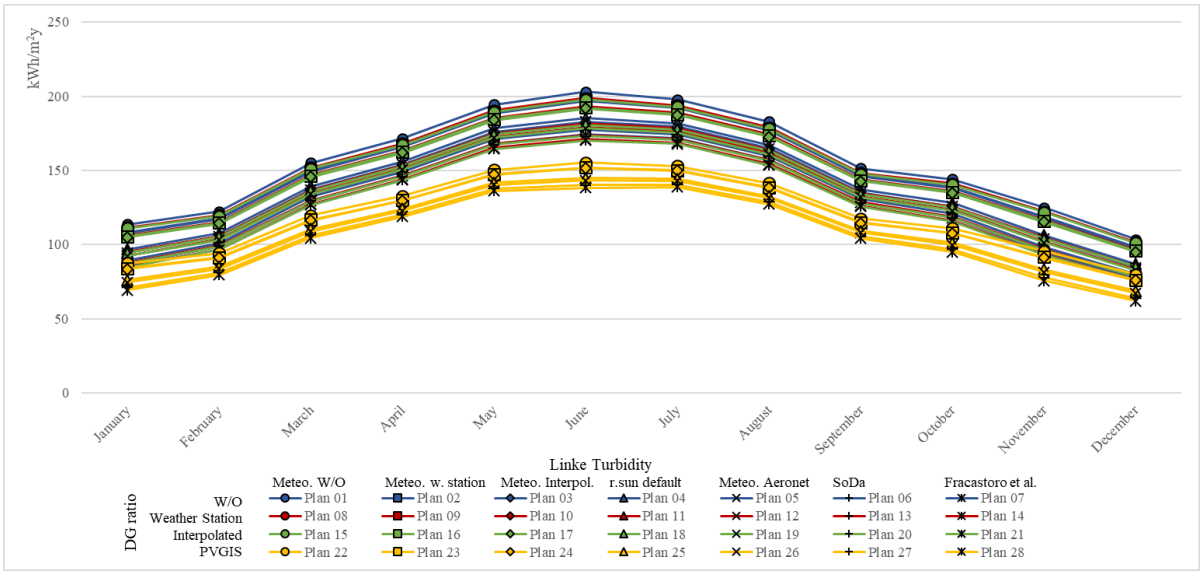

Figure 45 - Comparison of monthly results' maximum from elaborations with yearly inputs for building 4

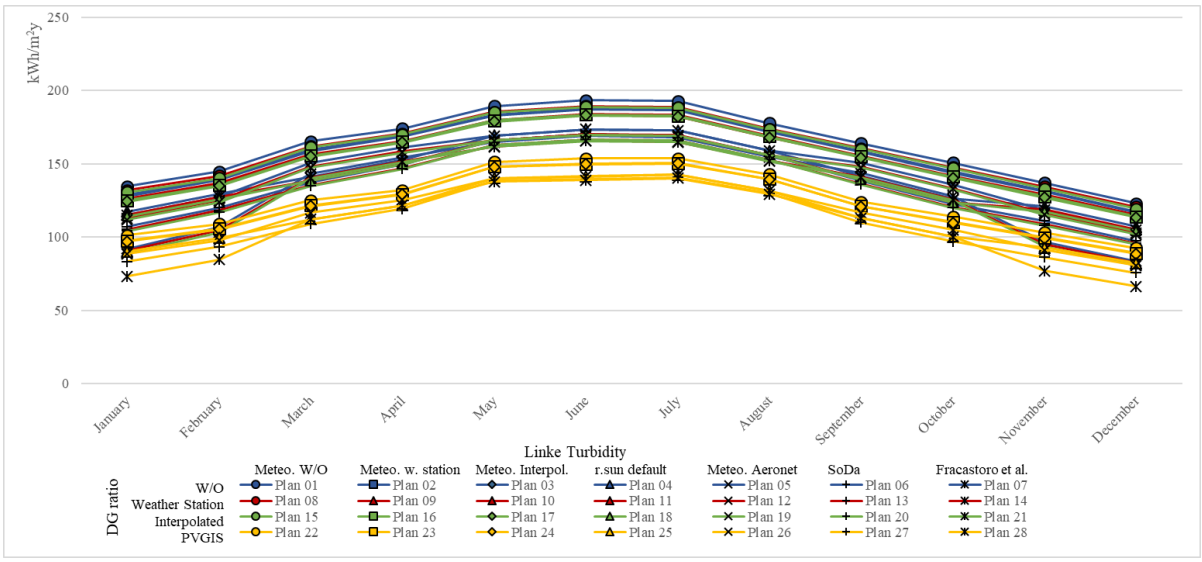

Figure 46 - Comparison of monthly results' maximum from elaborations with seasonal inputs for building 1

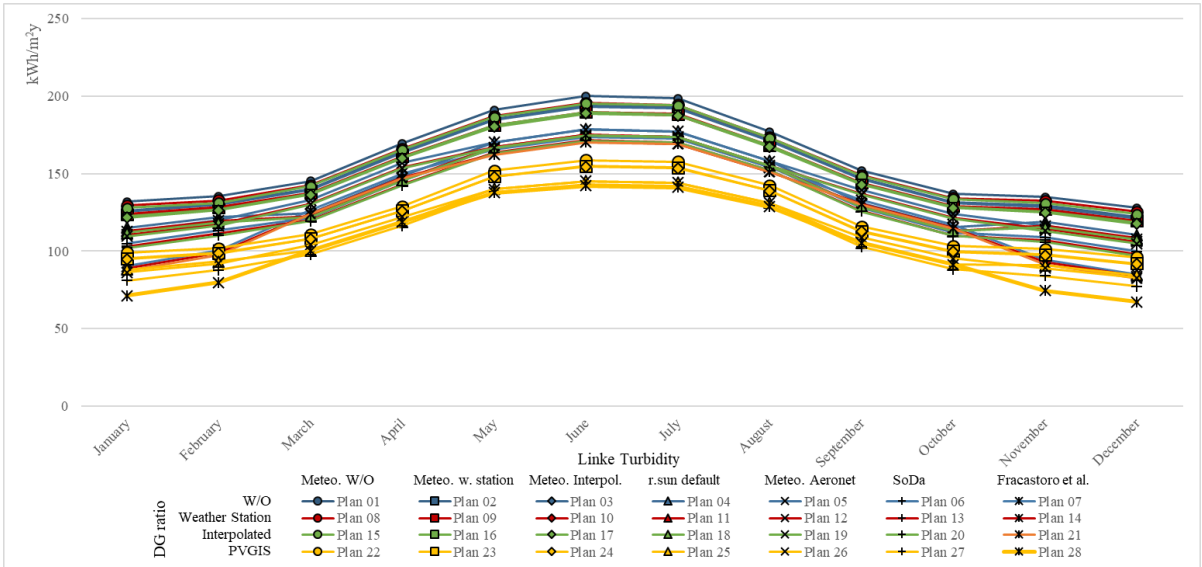

Figure 47 - Comparison of monthly results' maximum from elaborations with seasonal inputs for building 2

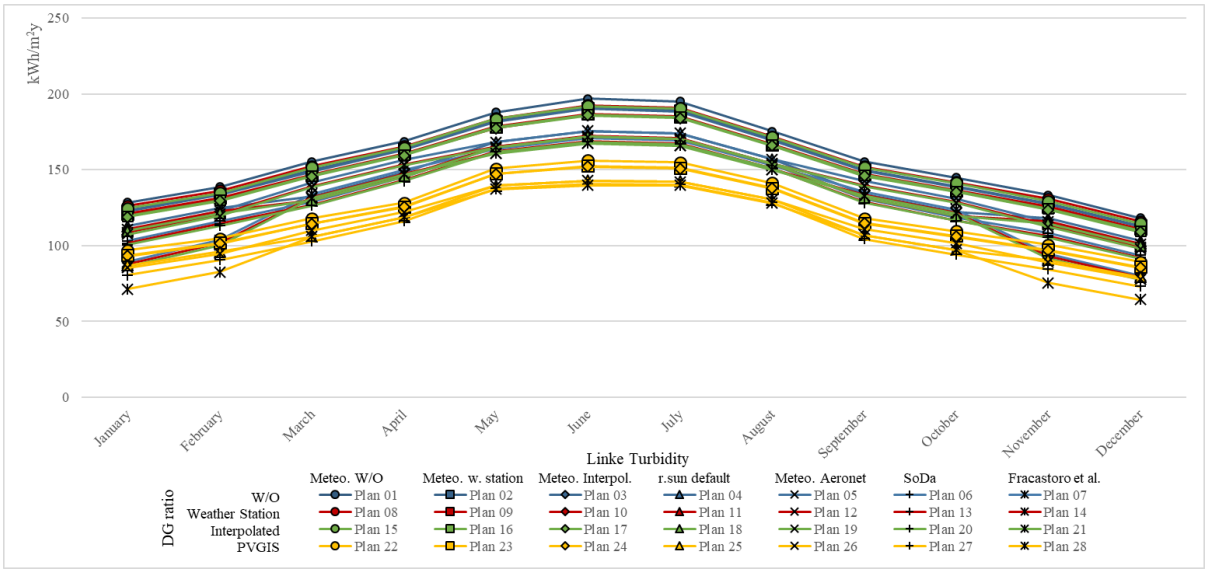

Figure 48 - Comparison of monthly results' maximum from elaborations with seasonal inputs for building 3

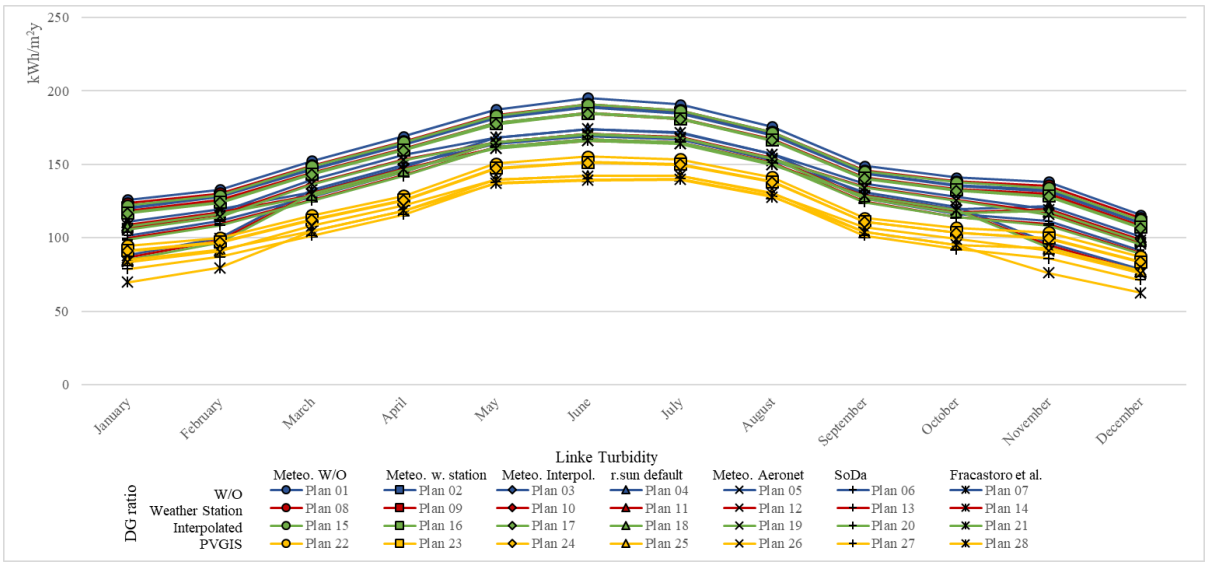

Figure 49 - Comparison of monthly results' maximum from elaborations with seasonal inputs for building 4

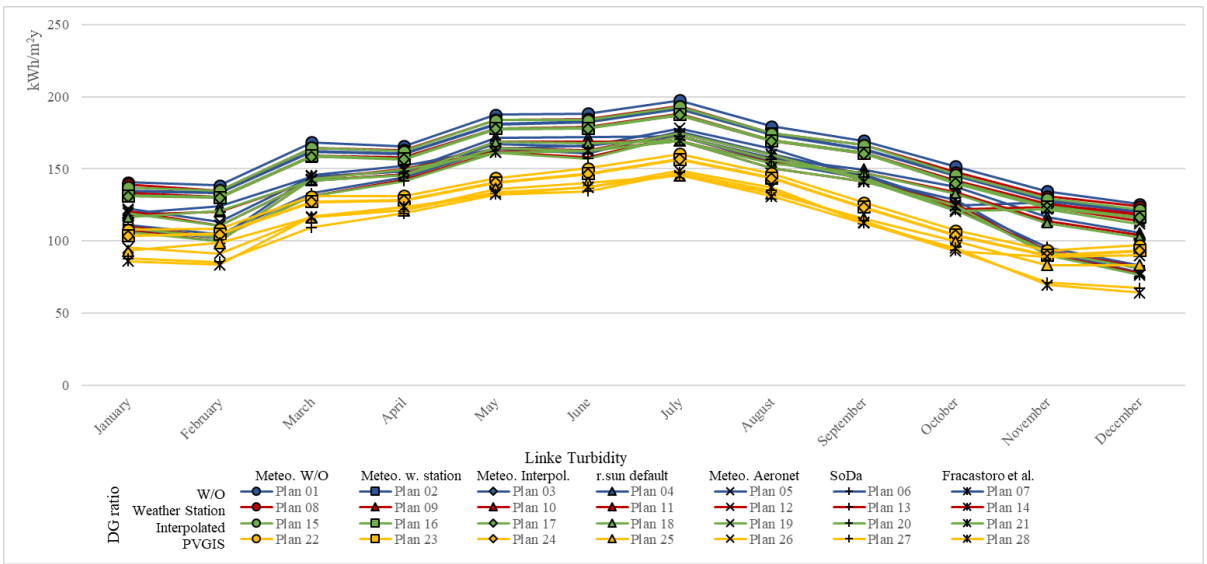

Figure 50 - Comparison of monthly results' maximum from elaborations with monthly inputs for building 1

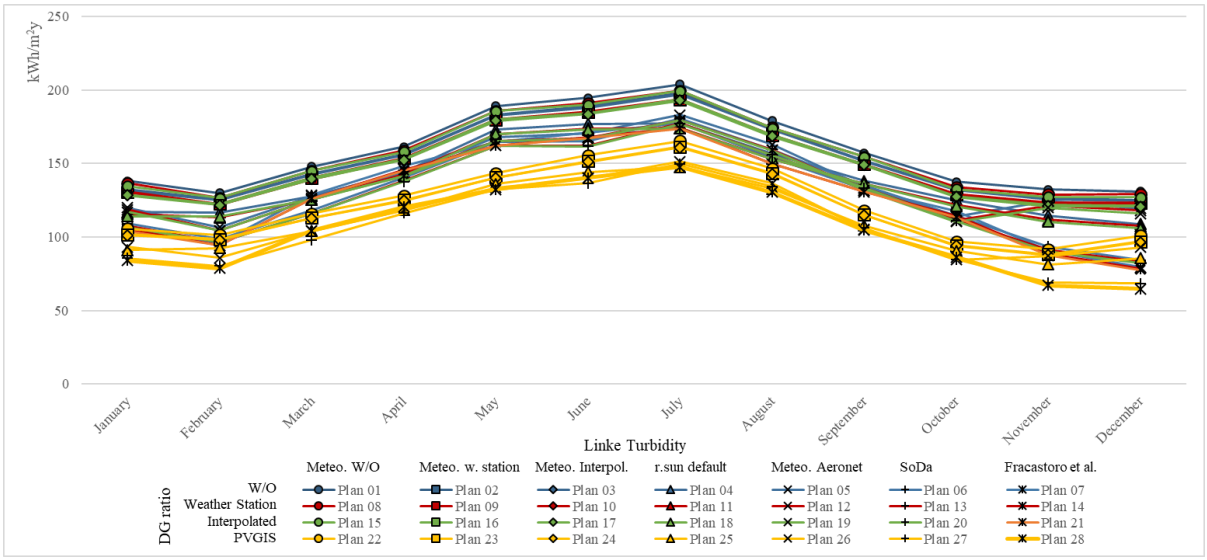

Figure 51 - Comparison of monthly results' maximum from elaborations with monthly inputs for building 2

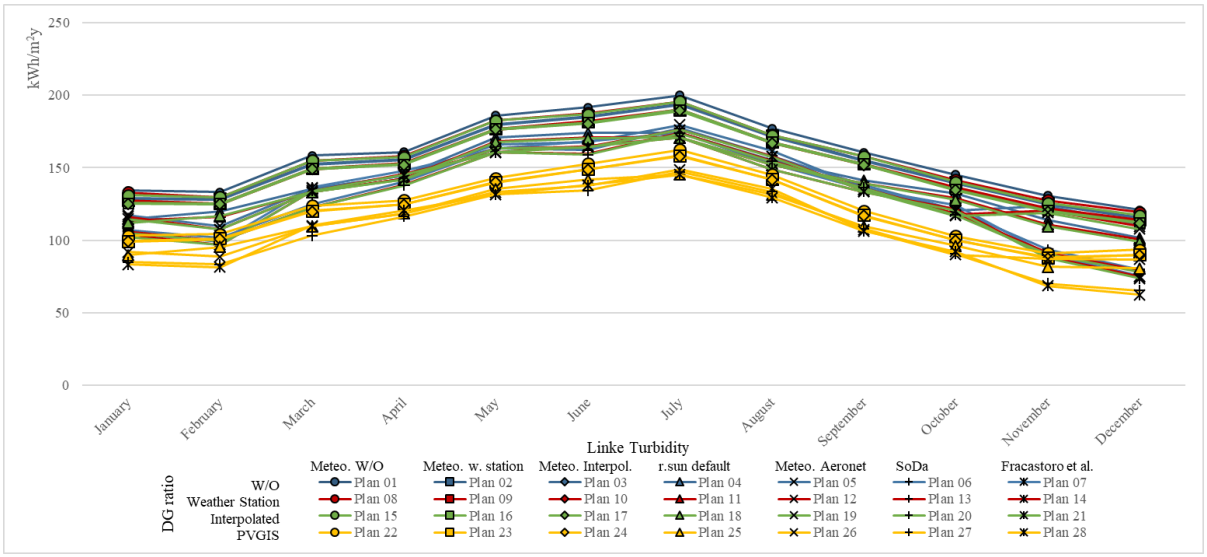

Figure 52 - Comparison of monthly results' maximum from elaborations with monthly inputs for building 3

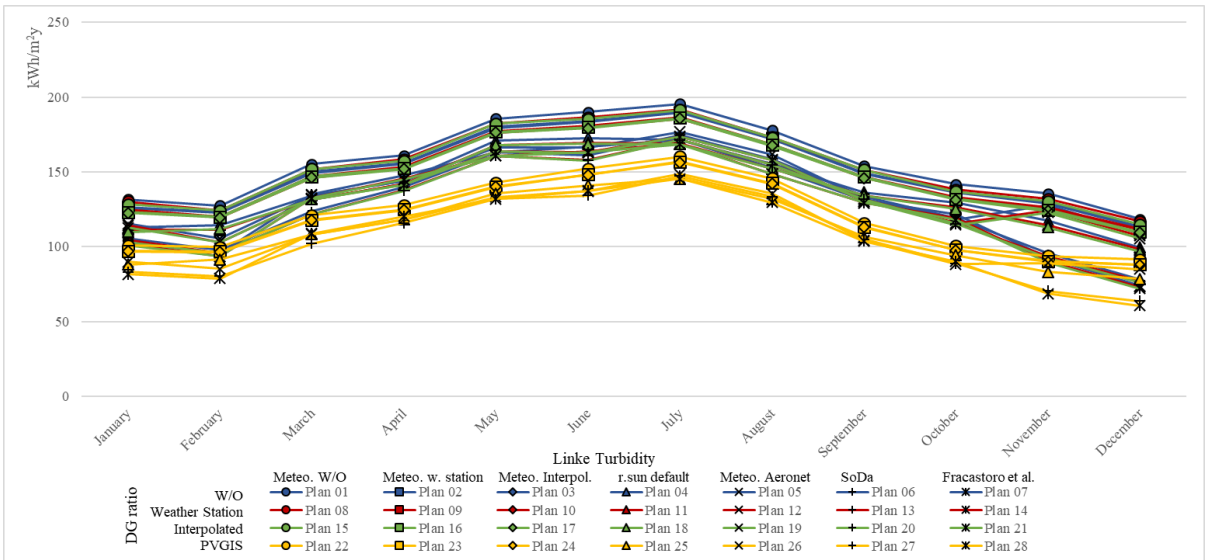

Figure 53 - Comparison of monthly results' maximum from elaborations with monthly inputs for building 4

According to Figures 42 to 45, considering yearly inputs, the building 1 shows maximum outcomes ranging from 200.6 kWh/m² to 65.8 kWh/m², while for the building 2, the maximum outcomes vary between 207.8 kWh/m² and 66.5 kWh/m². Similarly, the building 3 shows maximum outcomes ranging from 204.5 kWh/m² to 63.7 kWh/m². Lastly, the building 4 records maximum outcomes ranging from 203.0 kWh/m² to 62.1 kWh/m².

In terms of seasonal parameters, the Figures 46 to 49 illustrate the maximum monthly solar radiation outcomes across the same four buildings.
The building 1 reports maximum outcomes ranging from 193.4 kWh/m² to 66.3 kWh/m², while for the building 2, the maximum outcomes vary between 200.0 kWh/m² and 67.2 kWh/m². Similarly, the building 3 shows maximum outcomes ranging from 196.7 kWh/m² to 64.3 kWh/m². Lastly, the building 4 exhibits maximum outcomes ranging from 195.2 kWh/m² to 62.6 kWh/m².

Regarding monthly parameters shown in Figures 50 to 53, the maximum monthly solar radiation outcomes across four buildings over a year are depicted. The building 1 shows maximum values ranging from 197.6 kWh/m² to 82.9 kWh/m².
In the case of the building 2, maximum outcomes vary between 203.8 kWh/m² and 76.9 kWh/m². Similarly, the building 3 exhibits maximum outcomes ranging from 200.1 kWh/m² to 78.9 kWh/m². Lastly, the building 4 records maximum outcomes ranging from 195.6 kWh/m² to 72.9 kWh/m².

Considering the depiction of the minimum outcomes in Figures 54 to 65, an adjustment has been made to enhance the clarity of the charts; the scale of the vertical axis has been modified to fit the relatively smaller values observed in these outcomes.
This modification ensures that the presented data is clear and accessible, facilitating a detailed analysis of the variations in minimum solar radiation across different months and buildings.

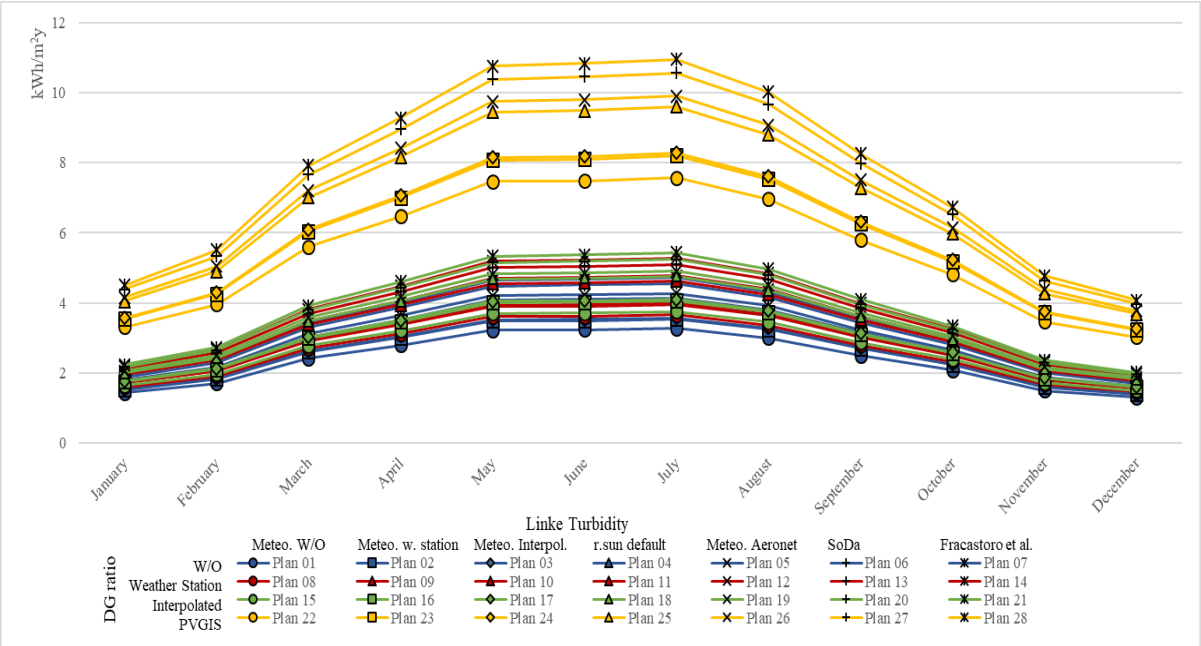

Figure 54 - Comparison of monthly results' minimum from elaborations with yearly inputs for building 1

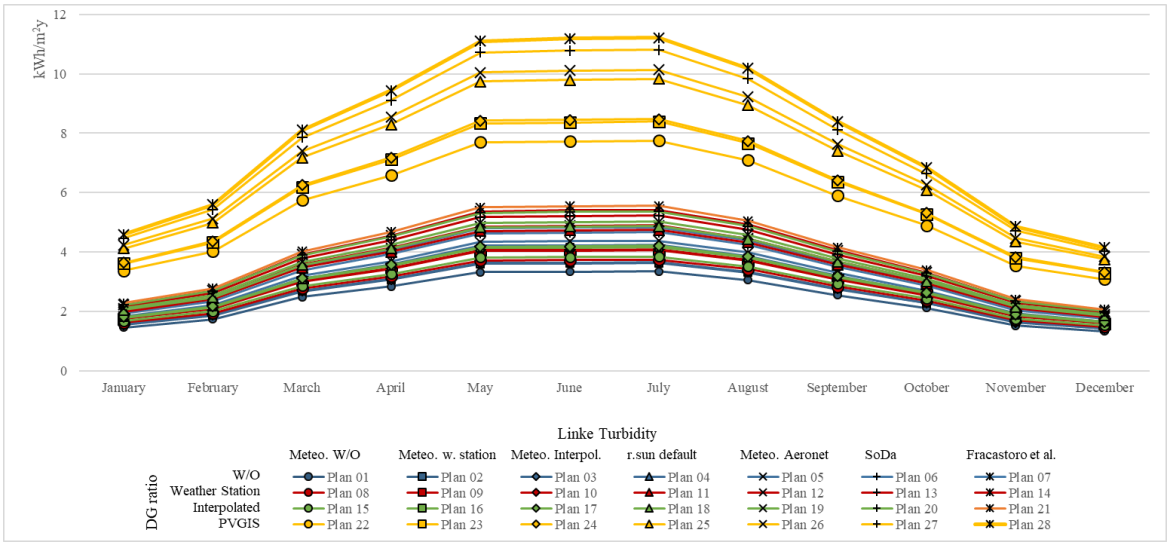

Figure 55 - Comparison of monthly results' minimum from elaborations with yearly inputs for building 2

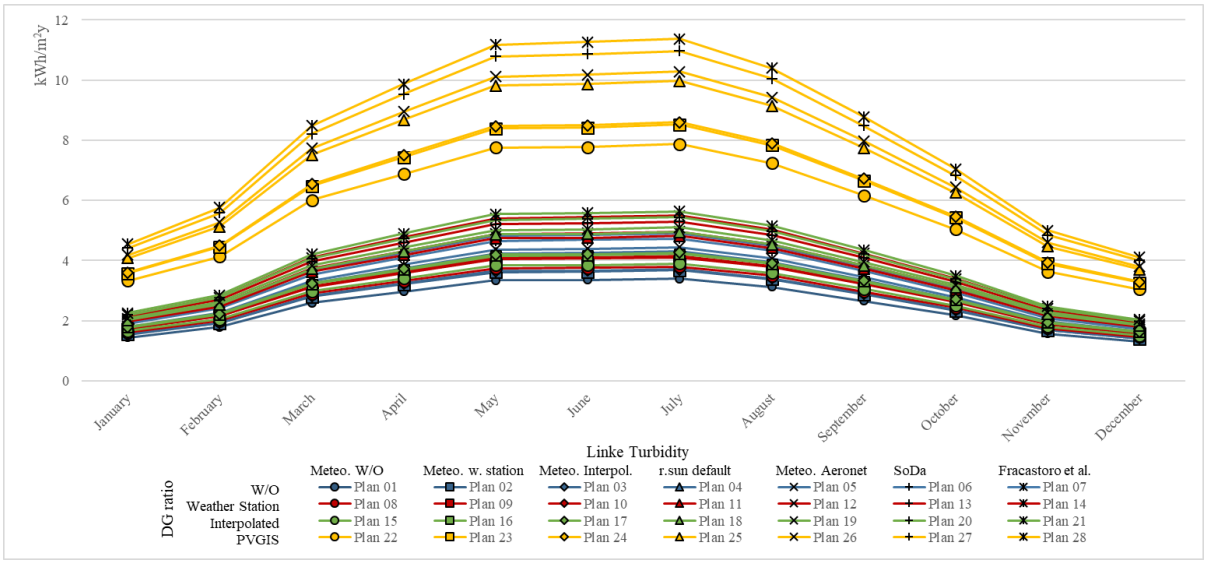

Figure 56 - Comparison of monthly results' minimum from elaborations with yearly inputs for building 3

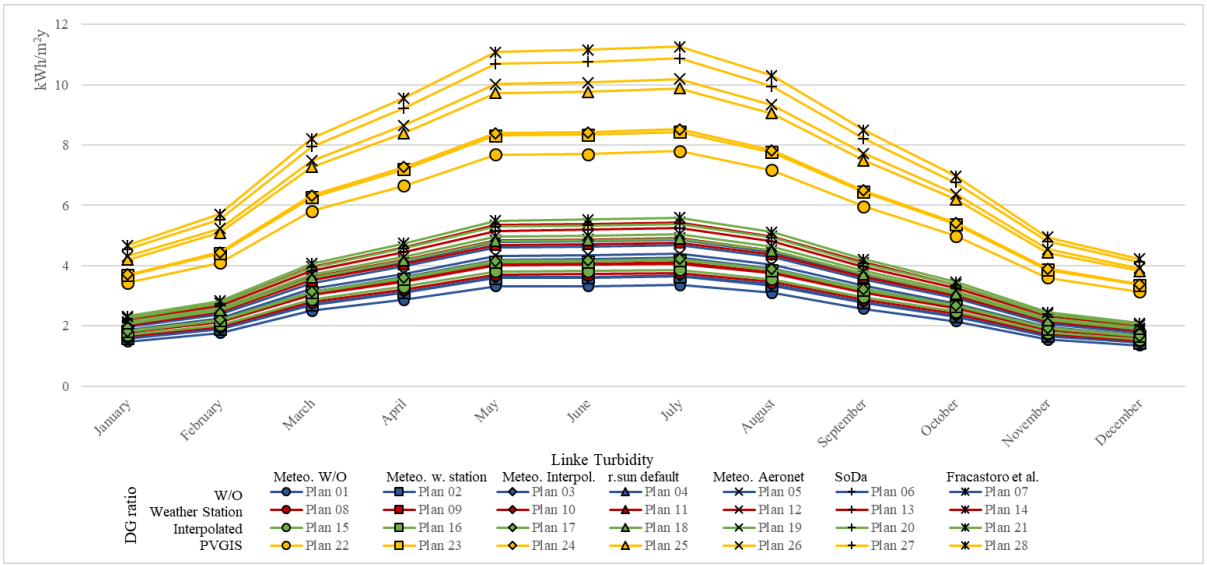

Figure 57 - Comparison of monthly results' minimum from elaborations with yearly inputs for building 4

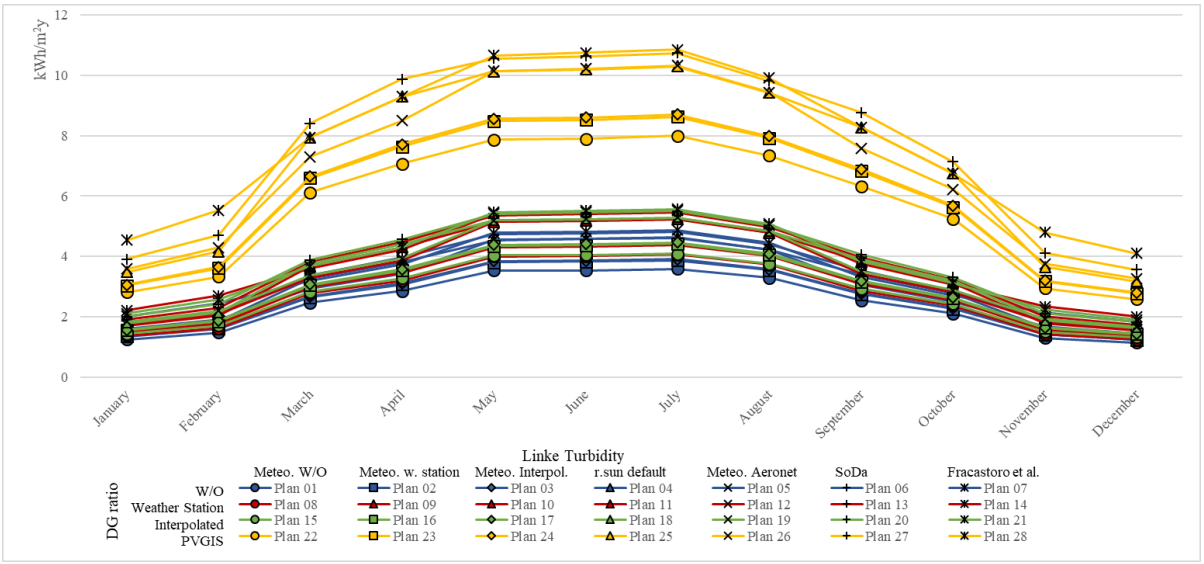

Figure 58 - Comparison of monthly results' minimum from elaborations with seasonal inputs for building 1

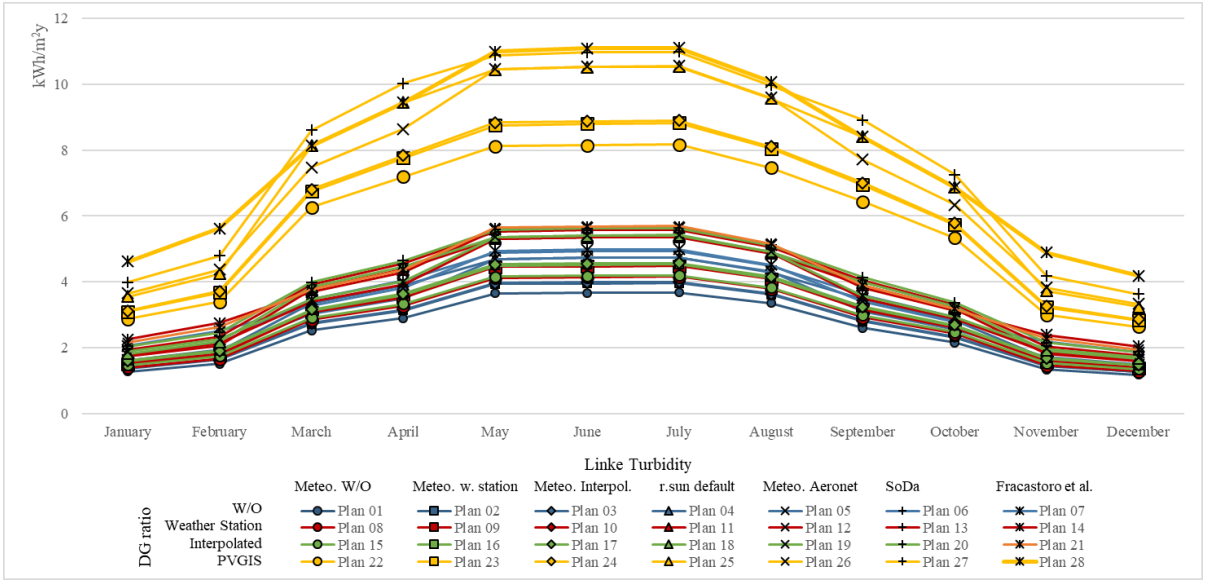

Figure 59 - Comparison of monthly results' minimum from elaborations with seasonal inputs for building 2

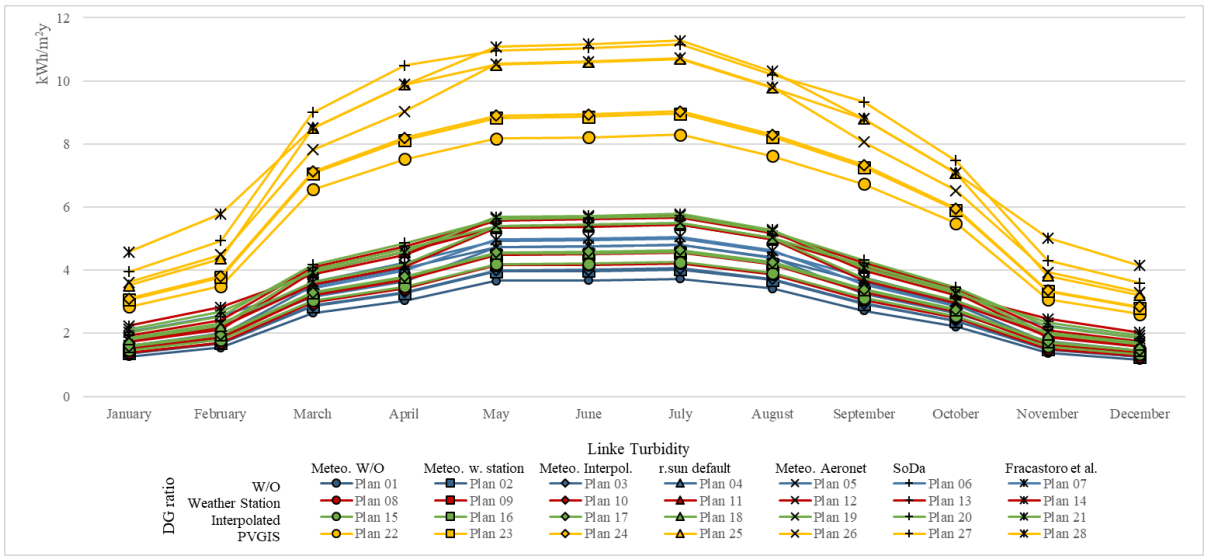

Figure 60 - Comparison of monthly results' minimum from elaborations with seasonal inputs for building 3

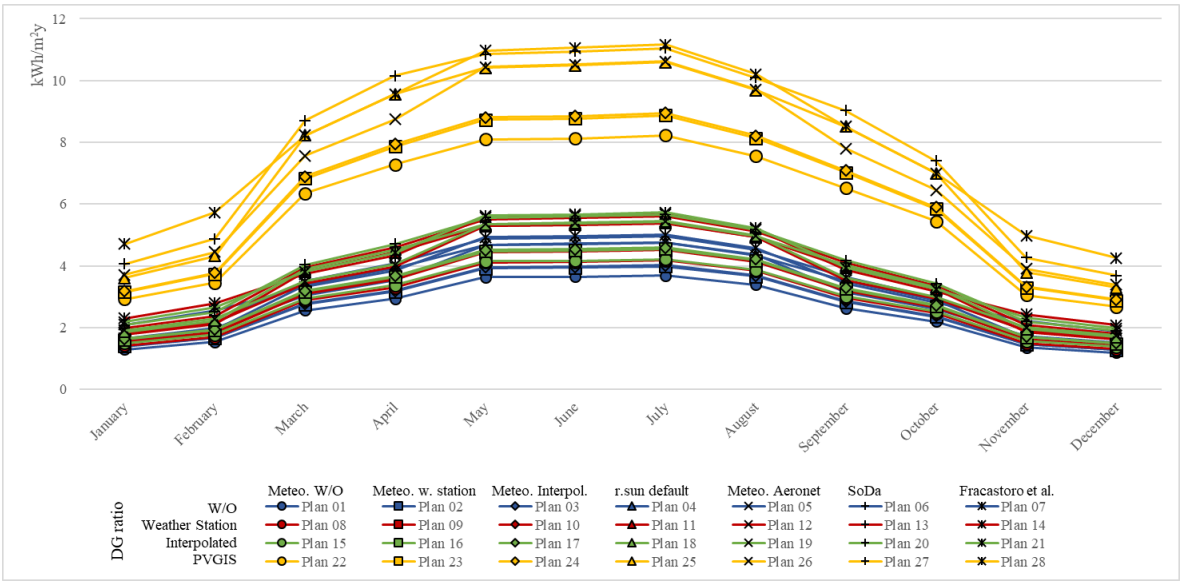

Figure 61 - Comparison of monthly results' minimum from elaborations with seasonal inputs for building 4

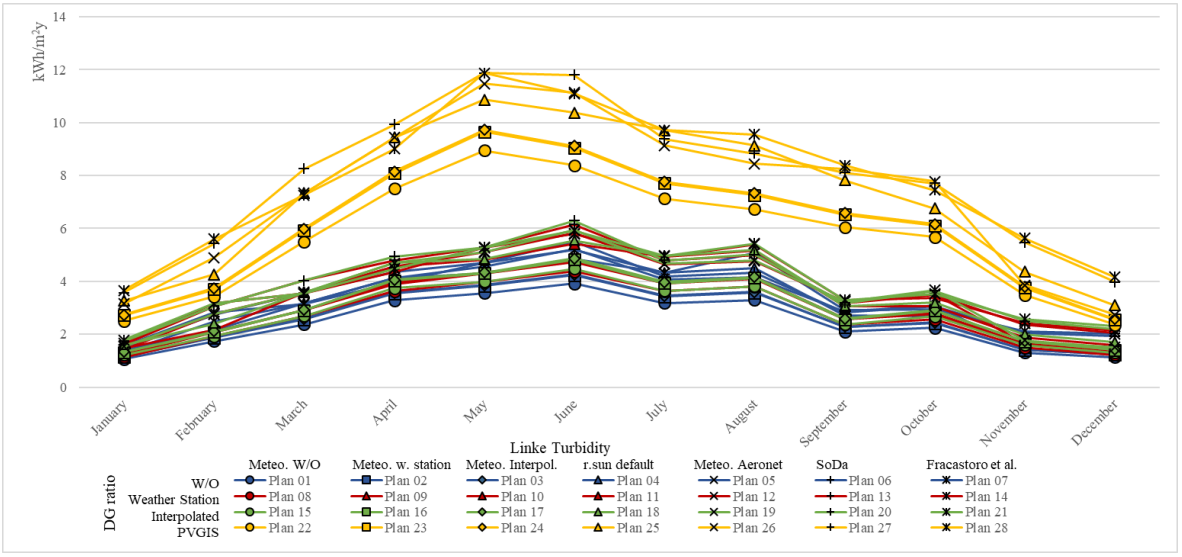

Figure 62 - Comparison of monthly results' minimum from elaborations with monthly inputs for building 1

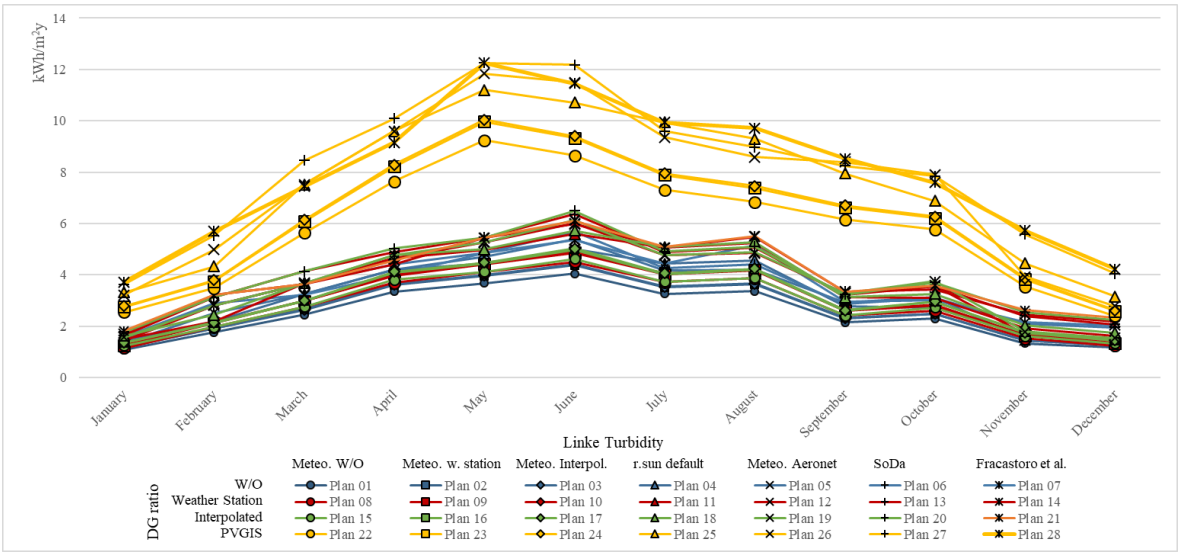

Figure 63 - Comparison of monthly results' minimum from elaborations with monthly inputs for building 2

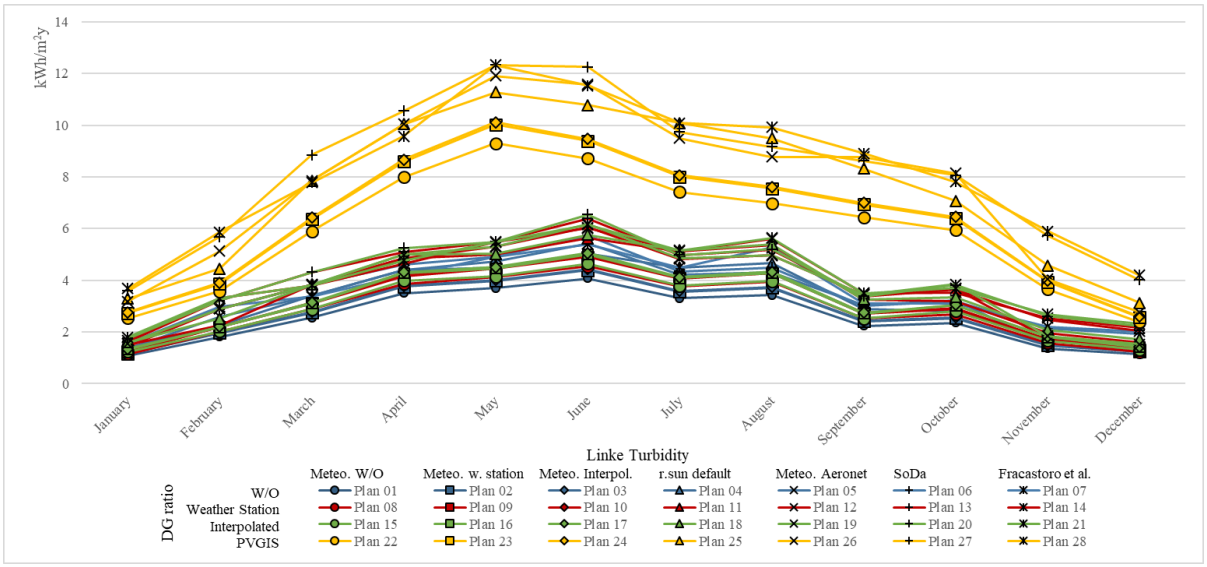

Figure 64- Comparison of monthly results' minimum from elaborations with monthly inputs for building 3

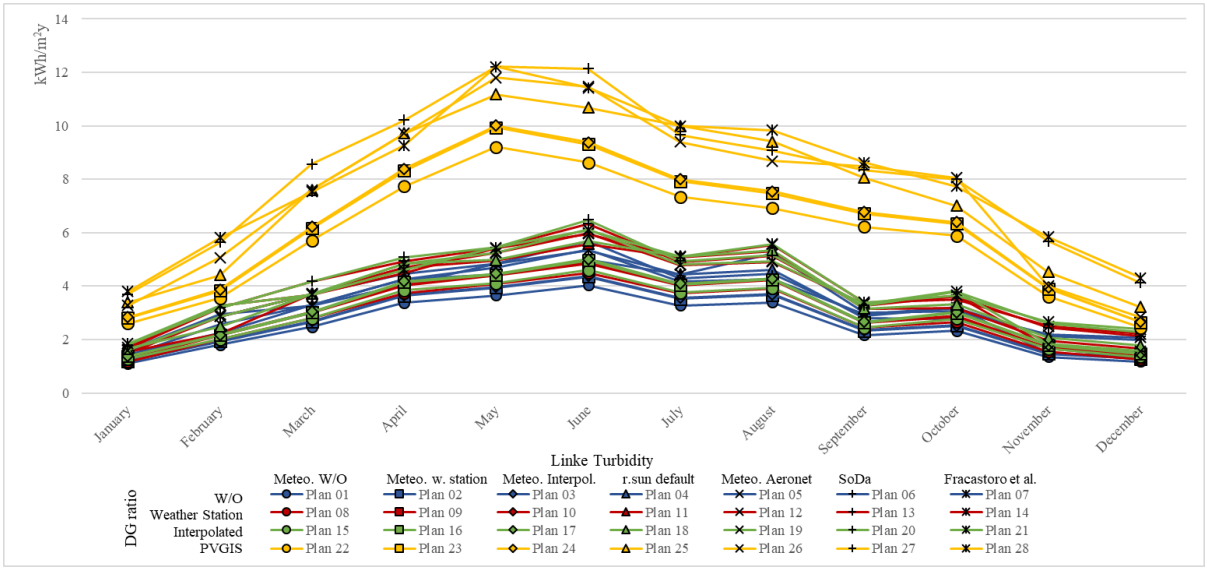

Figure 65 - Comparison of monthly results' minimum from elaborations with monthly inputs for building 4

According to the Figures 54 to 57, considering the yearly inputs, the minimum monthly solar radiation outcomes for the building 1 ranges from 10.9 kWh/m² to 1.5 kWh/m², while for the building 2, outcomes vary between 11.2 kWh/m² and 1.5 kWh/m². Similarly, the building 3 exhibits values ranging from 11.3 kWh/m² to 1.5 kWh/m². Lastly, the building 4 shows outcomes ranging from 11.2 kWh/m² to 1.4 kWh/m².

Regarding seasonal parameters shown in Figures 58 to 61, the minimum monthly solar irradiation outcomes for the building 1 is ranging from 10.8 kWh/m² to 1.1 kWh/m², while for the building 2, outcomes vary between 11.1 kWh/m² and 1.3 kWh/m². Similarly, the building 3 shows values ranging from 11.2 kWh/m² to 1.3 kWh/m². Lastly, the building 4 exhibits values ranging from 11.1 kWh/m² to 1.3 kWh/m².

In terms of monthly parameters illustrated in Figures 62 to 65, the minimum solar radiation outcomes for the building 1 vary from 11.8 kWh/m² to 1.1 kWh/m², while for the building 2, outcomes vary

between 12.2 kWh/m² and 1.2 kWh/m². Similarly, the building 3 shows values ranging from 12.3 kWh/m² to 1.1 kWh/m². Lastly, the building 4 records values ranging from 12.2 kWh/m² to 1.2 kWh/m².

Overall, an expected patterns, similar to the median outcomes (in Section 4.3.3.1 -), are observed. From January, the values start to increase until the summer months, and after reaching a peak, they begin to decrease until winter.
A significant difference can be seen between the minimum and maximum values, which may result from building orientation or shadows on the buildings during the estimation period.
To better compare the maximum and minimum outcomes, the average of the maximum outcomes, the average of the minimum outcomes, and the average of the median outcomes are considered and presented in Figures 66 to 69 for each building separately.

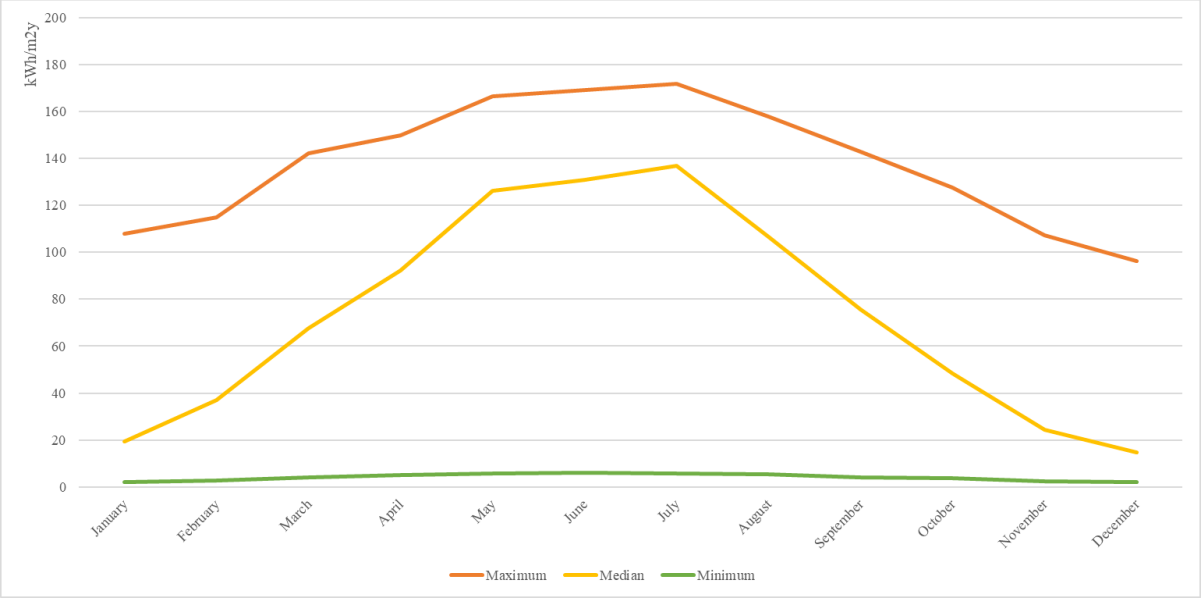

Figure 66 - The average of minimum, median, and maximum outcomes for the building 1

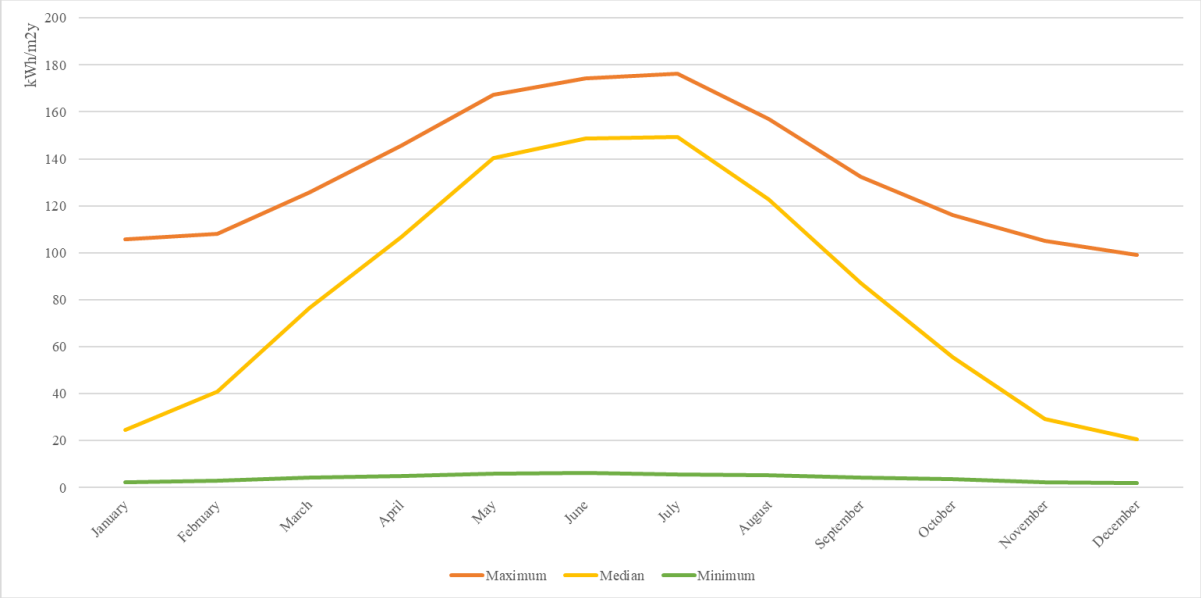

Figure 67 - The average of minimum, median, and maximum outcomes for the building 2

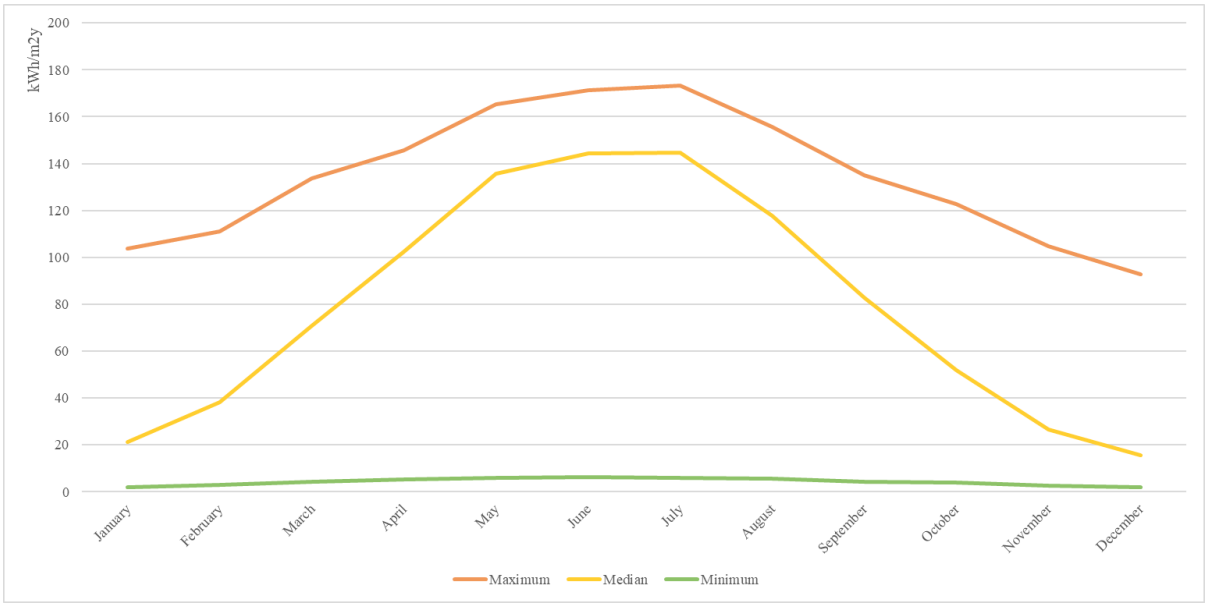

Figure 68 - The average of minimum, median, and maximum outcomes for the building 3

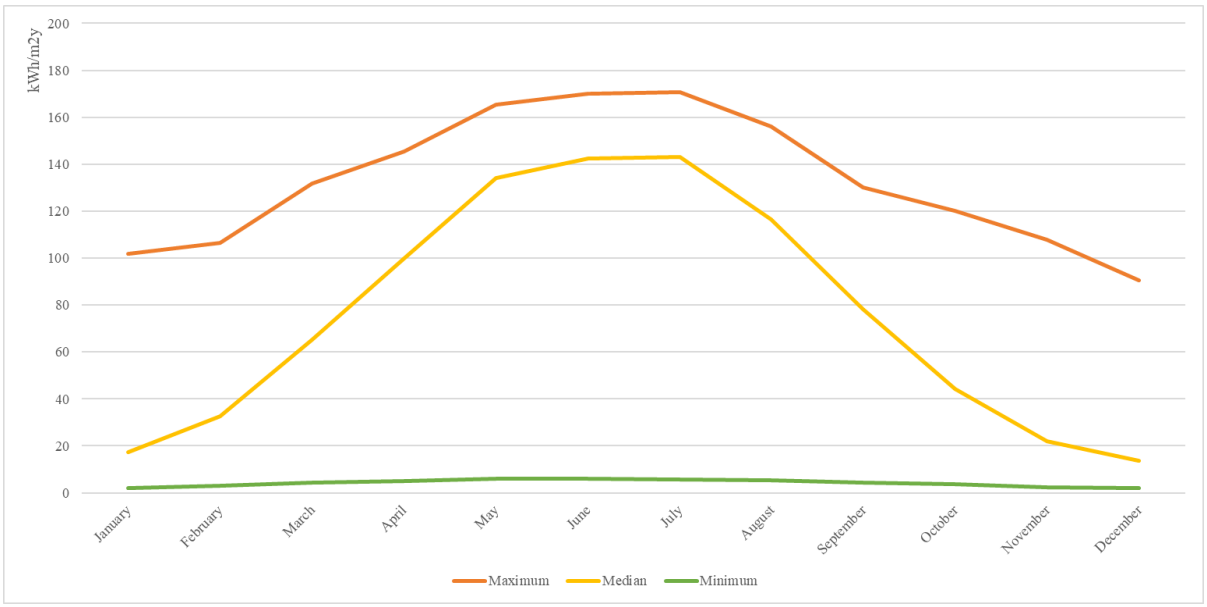

Figure 69 - The average of minimum, median, and maximum outcomes for the building 4

Figures 66 to 69 show that in summer months, median solar radiation values are closer to the maximum outcomes, indicating higher sunlight exposure.
In contrast, during winter months, the median values align more closely with the minimum outcomes, suggesting lower levels of solar radiation.

Table 13 provides the percentage differences between the average maximum and median values, as well as between the average median and minimum values. This comparison helps to understand how solar radiation varies across seasons, highlighting the seasonal fluctuations and their impact on sunlight exposure throughout the year.

Table 13 - Percentage Differences Between Average Maximum and Average Median Values, and Between Average Median and Average Minimum Values

Building	%Diff with Median	Results difference (%)											
		January	February	March	April	May	June	July	August	September	October	November	December
Building 1	Maximum Outcomes	455.13	210.36	110.53	62.27	31.71	29.21	25.42	48.15	88.83	163.27	338.91	549.65
	Minimum Outcomes	822.99	1233.51	1532.05	1744.63	2073.01	2100.95	2333.72	1899.50	1701.12	1213.63	920.35	635.34
Building 2	Maximum Outcomes	331.14	163.65	64.02	36.54	19.26	17.07	18.00	27.79	52.07	108.90	259.51	385.27
	Minimum Outcomes	1043.49	1352.34	1707.15	1998.65	2238.90	2326.54	2493.81	2170.22	1940.66	1381.61	1100.18	895.71
Building 3	Maximum Outcomes	389.21	191.64	88.70	42.29	21.95	18.69	19.68	32.12	63.07	136.04	296.12	495.29
	Minimum Outcomes	899.33	1211.22	1497.15	1822.25	2145.10	2238.75	2375.54	2031.30	1756.34	1248.94	953.93	666.59
Building 4	Maximum Outcomes	483.20	227.21	101.53	45.63	23.19	19.51	19.25	34.10	66.90	170.42	393.14	569.35
	Minimum Outcomes	699.93	1032.09	1422.52	1839.88	2143.15	2228.55	2372.69	2023.71	1708.08	1063.23	779.43	548.02
Average of difference		640.55	702.75	815.46	949.02	1087.03	1122.41	1207.26	1033.36	922.13	685.75	630.20	593.15

In general, Table 13 demonstrates that there are considerable seasonal variations in solar radiation differences. The most significant variations occur notably in summer months when solar radiation is highest. July stands out as the month with the largest differences across all buildings, while the lowest variation is seen in December, which highlights the impact of seasonal changes as well as the effects of orientation and shadowing on the solar radiation recieved by the buildings.

4.4 - Automation

Due to the complicated algorithms that are involved and the several required steps, the process of estimating solar irradiation using the r.sun.insoltime tool in the QGIS software is a very time-consuming process. Estimating the daily solar irradiation is the first step in the process, which is then followed by calculating the monthly outcomes and then aggregating all of the findings to obtain the yearly solar radiation. In order to complete this process, it is required to calculate the solar radiation for the area under study and then determine the quantity of solar radiation received by the buildings located within that area. The process also requires a significant amount of computer resources, which includes the use of a substantial amount of memory and the creation of temporary files that are only usable during particular projects and calculations.

The method of estimating solar radiation is carried out for a total of 28 different plans within the scope of this investigation, making use of the criteria described in section 4.2 -. Due to the repetitive nature of this task, the importance of automating the process to improve both speed and accuracy became evident. In response to this, incorporating computer programming in Python would be highly efficient. Python scripts can continuously iterate and perform calculations, using the output of each function and

algorithm as an input for the next iteration, all while avoiding the generation of a large number of temporary files.

Since QGIS models are based on Python programming, the software can generate Python script codes for these models, and the Graphical Modeler tool is not an exception. Therefore, the Graphical Modeler tool in QGIS was chosen to automate the solar radiation estimation procedure. It utilizes Python, can be extracted into Python scripts for further development or use, and features a simple user interface that connects the required nodes to create the desired algorithm..

As this study requires input parameters on a monthly, seasonal, and yearly basis, three distinct models are presented in order to account for the fluctuations that exist in these parameters (Figures 70 to 72). In the raster and shapefile formats, respectively, the Elevation model and the buildings that are planned to be located in the research area are brought into each of these models as the main inputs.

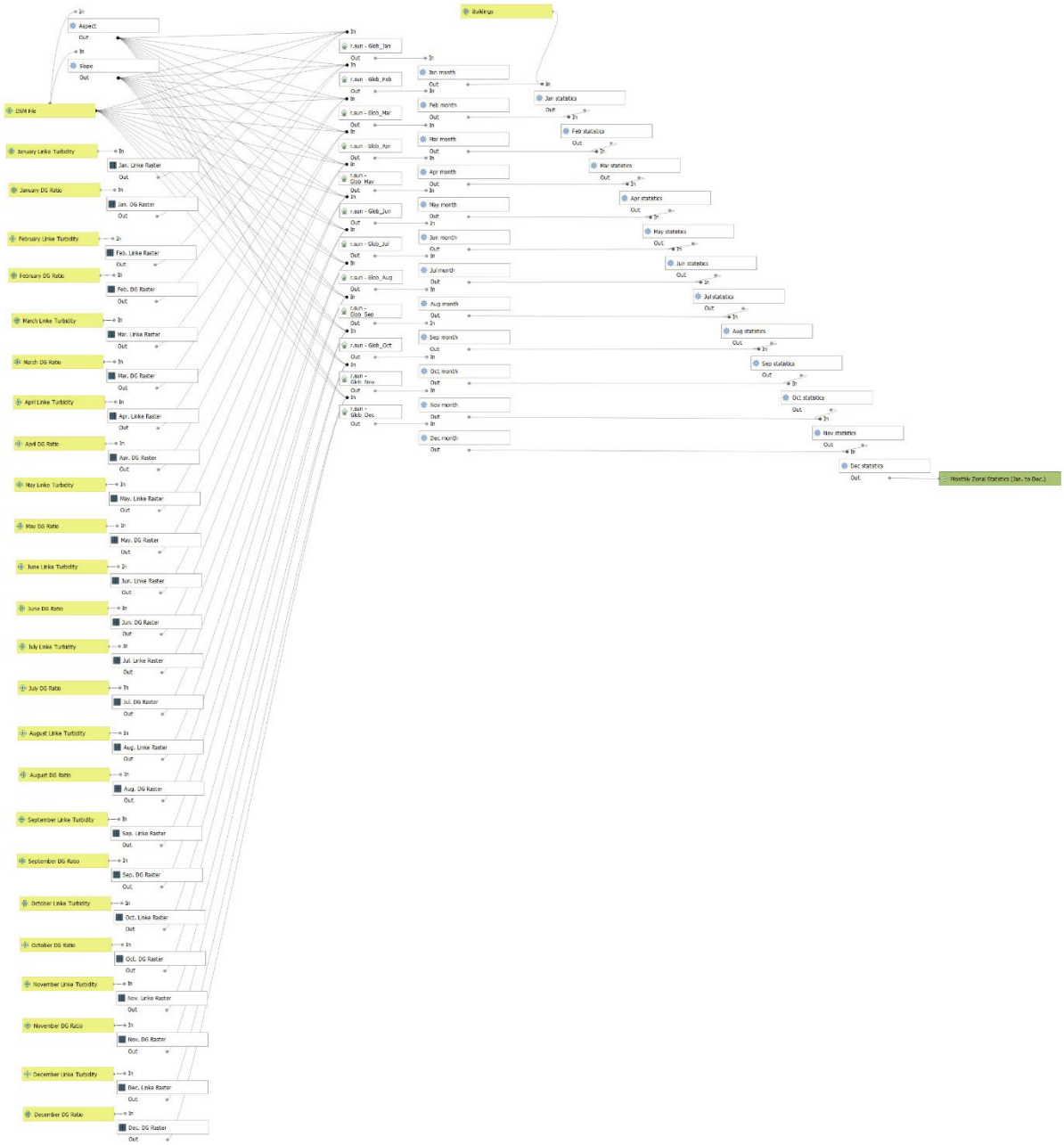

Figure 70 - Composite function for the solar radiation estimation with monthly inputs

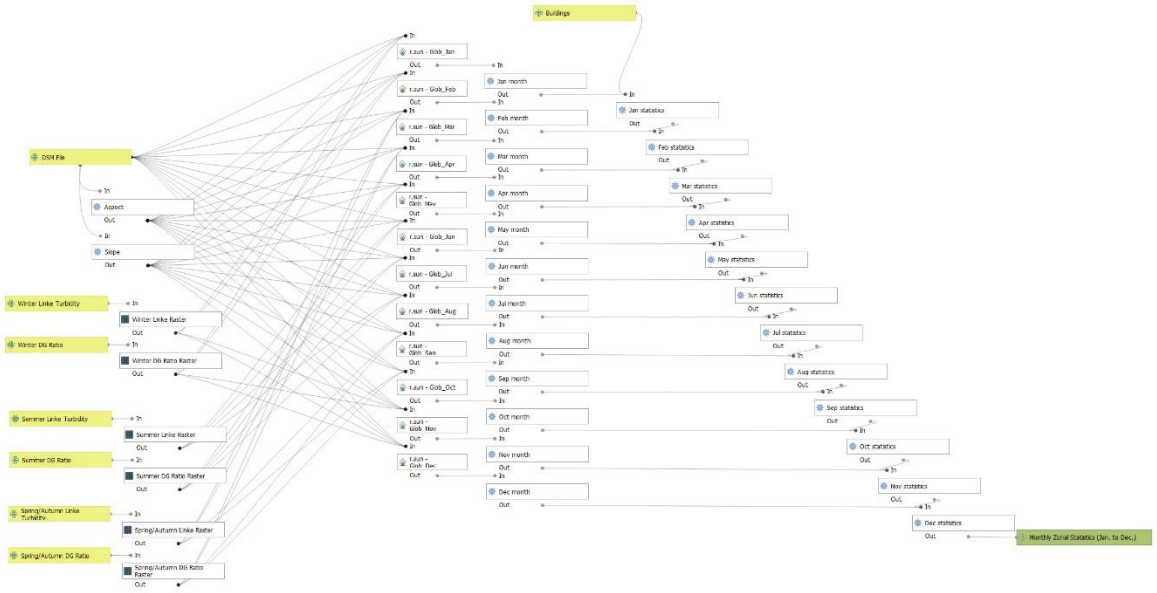

Figure 71 - Composite function for the solar radiation estimation with seasonal input aggregation

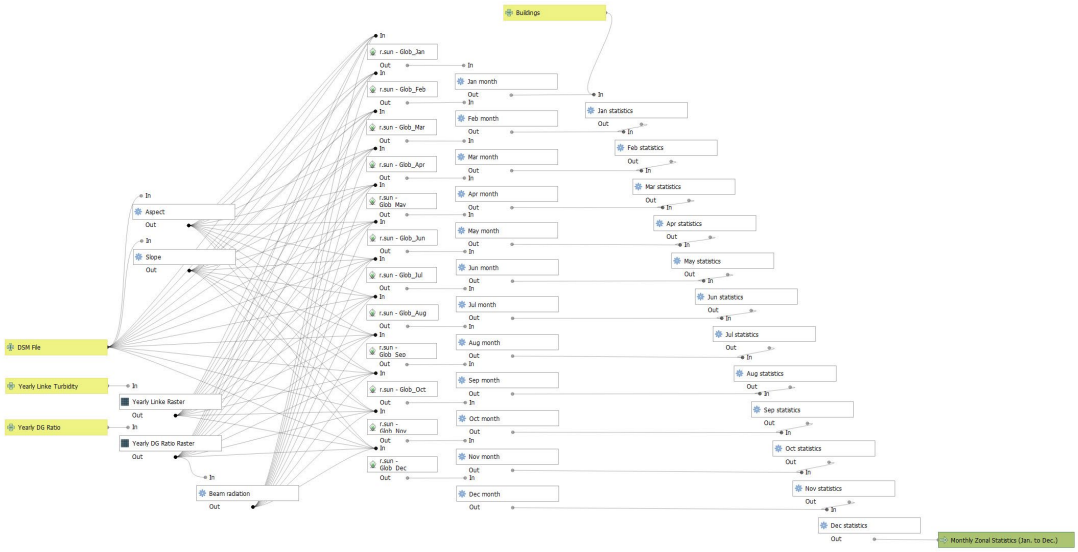

Figure 72 - Composite function for the solar radiation estimation with yearly input aggregation

Twelve distinct parameters for the T_L factor, each of which corresponds to a particular month, are required for the monthly model. Additionally, twelve distinct parameters for the DG ratio are required, each of which corresponds to a different month. By employing three distinct parameters for the T_L factor and the DG ratio, the seasonal model makes this process more straightforward. These parameters are as follows:

- one for the summer months
- one for the winter months
- one for the spring and fall months

A single number is used for both the T_L factor and the DG ratio in the yearly model, which is relevant to all months. To prepare a raster file for the r.sun.insoltime algorithm, the Create Constant Raster Layer tool is utilized to generate the T_L Factor and DG ratio raster files. This simplification makes the procedure faster and more efficient.

The model determines the values of aspect and slope by using the Elevation model its input. The automatic calculation of solar radiation is made by the input values provided by the user and the results obtained from the algorithms in the model.

For the buildings in the area under study, the global radiation (irradiance/irradiation) outputs of these models are computed using the Zonal Statistics tool, within the model, which contain the minimum, maximum, and median values of the monthly solar radiation. The measuring unit of the outcomes are in Wh/m^2y. In order to facilitate analysis, the user has the ability to select the format of the output, which is offered by the QGIS software.

```python
from qgis.core import QgsProcessing
from qgis.core import QgsProcessingAlgorithm
from qgis.core import QgsProcessingMultiStepFeedback
from qgis.core import QgsProcessingParameterVectorLayer
from qgis.core import QgsProcessingParameterRasterLayer
from qgis.core import QgsProcessingParameterNumber
from qgis.core import QgsProcessingParameterFeatureSink
import processing


class YearlyIrradiationNewWithInputNumber(QgsProcessingAlgorithm):

    def initAlgorithm(self, config=None):
        self.addParameter(QgsProcessingParameterVectorLayer('buildings', 'Buildings', defaultValue=None))
        self.addParameter(QgsProcessingParameterRasterLayer('dsm_file', 'DSM File', defaultValue=None))
        self.addParameter(QgsProcessingParameterNumber('yearly_dg_ratio', 'Yearly DG Ratio', type=QgsProcessingParameterNumber.Double, defaultValue=None))
        self.addParameter(QgsProcessingParameterNumber('yearly_linke_turbidity', 'Yearly Linke Turbidity', type=QgsProcessingParameterNumber.Double, defaultValue=None))
        self.addParameter(QgsProcessingParameterFeatureSink('MonthlyZonalStatisticsJanToDec', 'Monthly Zonal Statistics (Jan. to Dec.)', type=QgsProcessing.TypeVectorAny

    def processAlgorithm(self, parameters, context, model_feedback):···

    def name(self):···

    def displayName(self):···

    def group(self):···

    def groupId(self):···

    def createInstance(self):
        return YearlyIrradiationNewWithInputNumber()
```

Figure 73 - Python script extracted from QGIS for the solar radiation estimation with yearly input aggregation

Regarding the Python script provided by the QGIS (Figure 73), to detail the technical implementation of the model, a Python class designed as a QGIS processing algorithm, plays a crucial role. This class, inheriting from QgsProcessingAlgorithm in the QGIS core library, is tailored to compute yearly irradiation statistics using various inputs such as building vector layers, DSM raster files, yearly DG ratio, and yearly Linke turbidity. It leverages components from the QGIS core and processing modules, including:

- QgsProcessingParameterVectorLayer
- QgsProcessingParameterRasterLayer
- QgsProcessingParameterNumber

Using the Graphical Modeler tool in QGIS to automate the process of estimating solar radiation is a significant progress in comparison to the typical manual strategies. This tool provides a flexible and efficient solution for accurate solar radiation assessment by adjusting to a broad variety of input parameter categories through the utilization of custom models.

4.5 - Critical Assessment of the Findings

This study has explored how different input parameters —yearly, seasonal, and monthly—affect solar irradiation estimates in the QGIS software for four distinct buildings, shedding light on their potential for solar energy production. Beyond simply looking at median values, it has also examined the variability in solar irradiation results across the buildings.

The results produced by the r.sun.insoltime tool in QGIS are described in detail in section 4.3 -. In this stage, in order to better describe the variety of outcomes that can occur, visual representations of the fluctuations in minimum, median, and maximum monthly values throughout the year under yearly, seasonal, and monthly parameters are provided in Figures 74 to 76; additionally, Figure 77 is included that overlays these values in a single visualization for easier comparison.

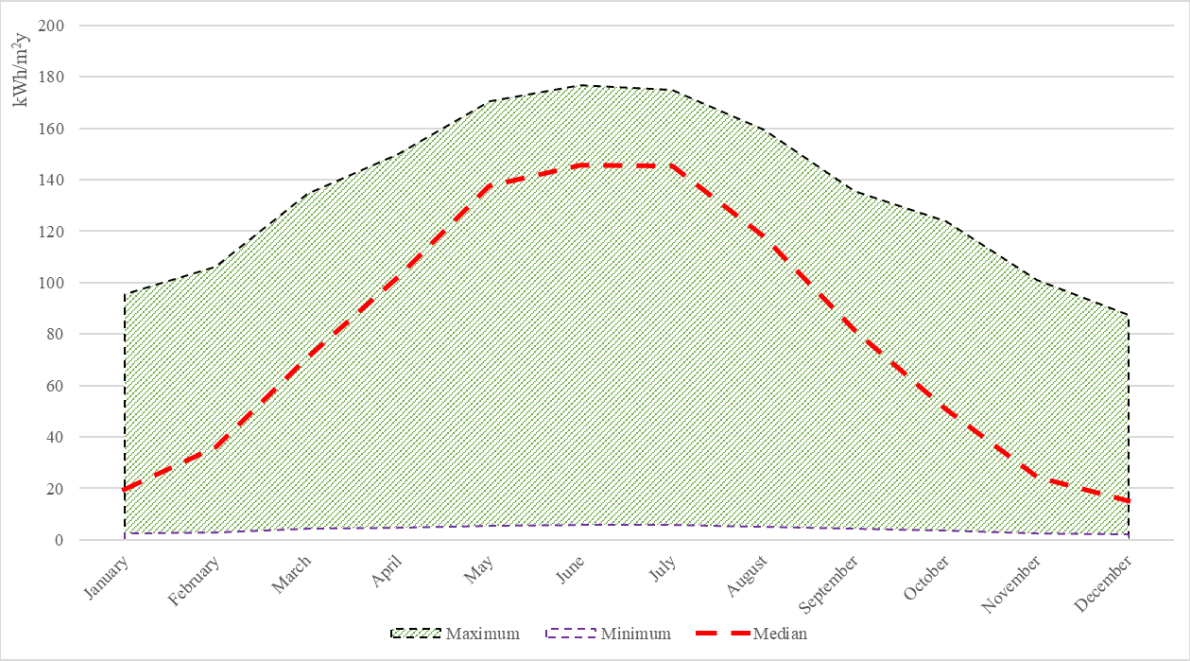

Figure 74 - Range between averages of minimum and maximum values for each month compared to the median with yearly inputs for all buildings

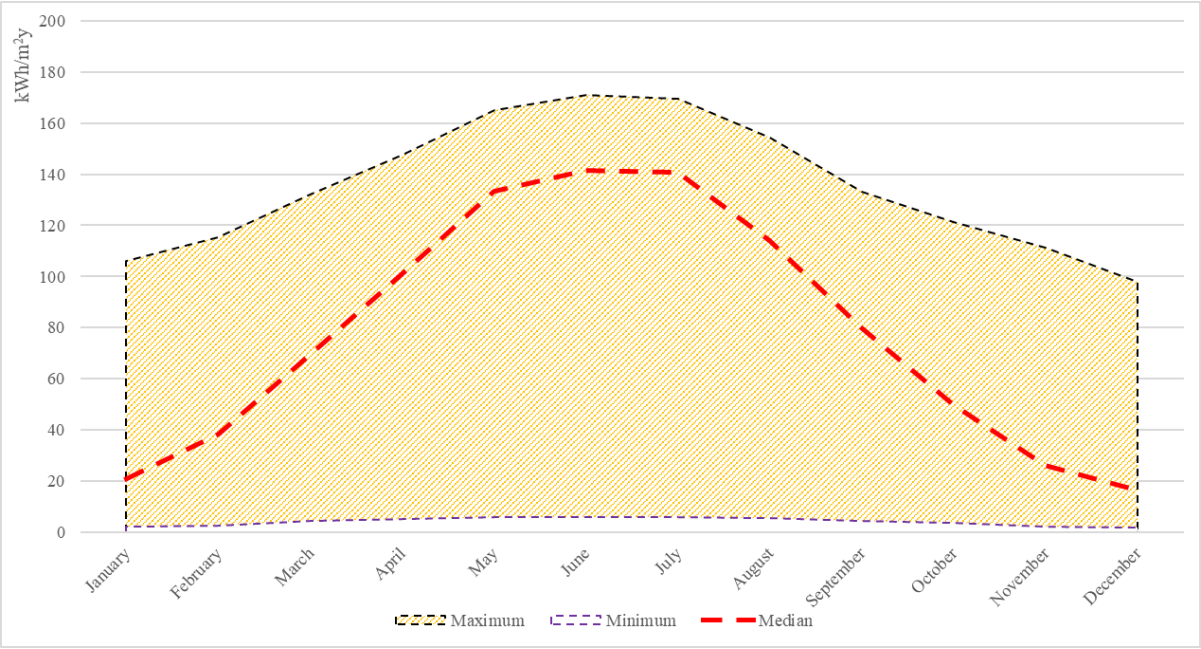

Figure 75 - Range between averages of minimum and maximum values for each month compared to the median with seasonal inputs for all buildings

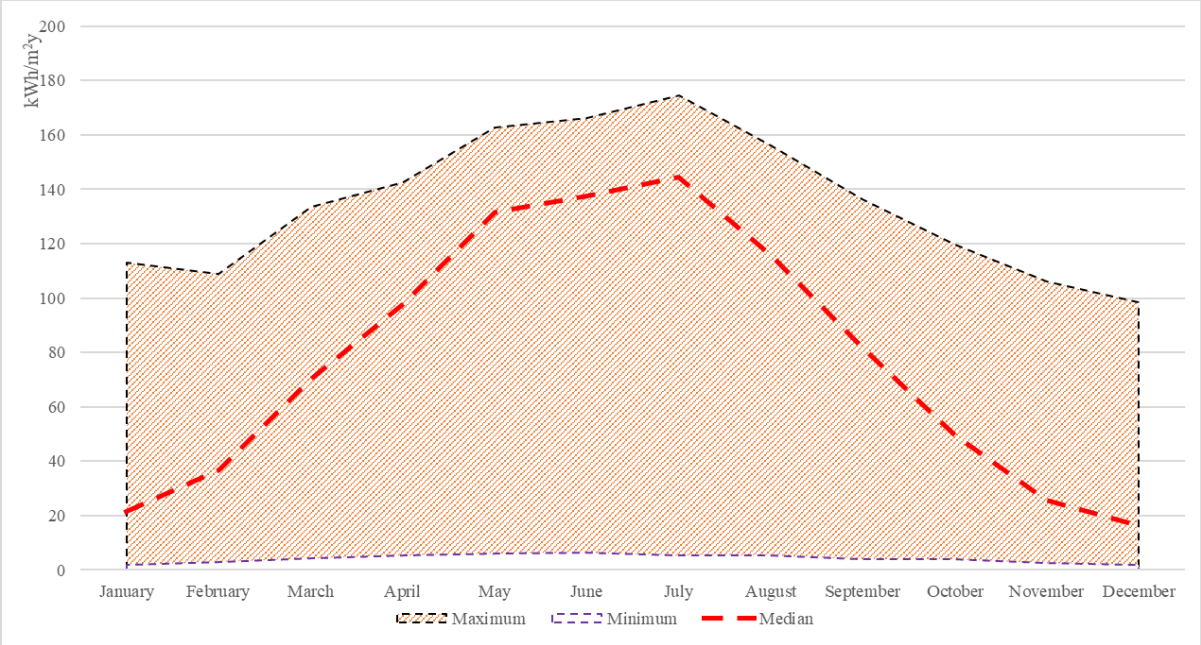

Figure 76 - Range between averages of minimum and maximum values for each month compared to the median with monthly inputs for all buildings

According to Figures 74 to 76, the average minimum and maximum solar irradiation outcomes for all four buildings vary across different timescales.

Regarding yearly parameters (Figure 74), the average of minimum outcomes ranges from 2,100 kWh/m² to 5,670 kWh/m², and the average of maximum results ranges from 8.7 kWh/m² to 176.5 kWh/m². Concerning seasonal parameters (Figure 75), the average of minimum results ranges from 1.9 kWh/m² to 6.1 kWh/m², and the average of maximum results ranges from 9.8 kWh/m² to 170.9 kWh/m². Lastly, for monthly parameters (Figure 76), the average of minimum outcomes ranges from 1.8 kWh/m² to 6.5 kWh/m², and the average of maximum outcomes ranges from 98.5 kWh/m² to 166.1 kWh/m².

In general, the near-null minimum obtained values are mainly due to shadow-casting elements such as chimneys and dormers, which limit incident radiation. Conversely, maximum values exceed 100 kWh/m² in all months except December. Despite these variations, the overall distribution of values mirrors that of the median, with the highest increase in March, the most notable decrease in September, and a peak in July.

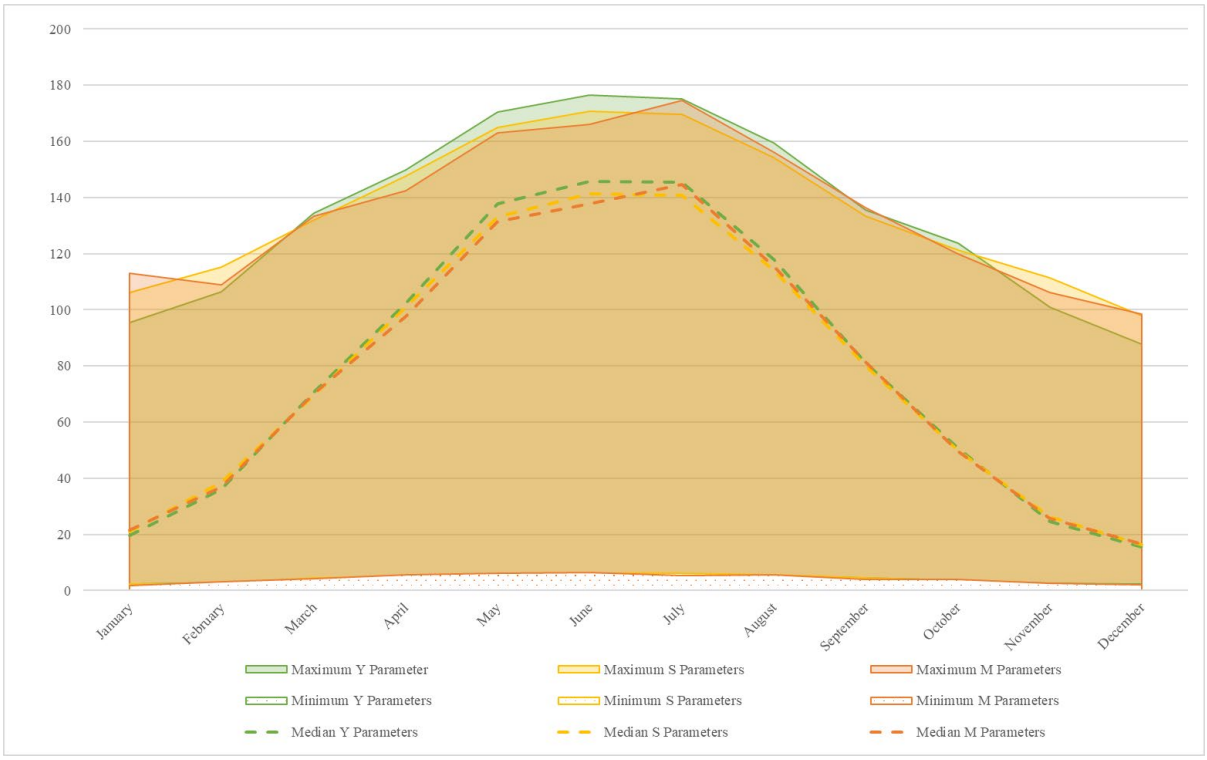

Figure 77 - Comparison of minimum, median, and maximum monthly solar irradiation for all building, concidering yearly, seasonal, and monthly parameters

These findings suggest that using minimum and maximum values for calculating average solar radiation is flawed and less accurate than using median values. The median values provide a more reliable measure, as indicated by the small percentage differences when comparing outcomes using different parameters. Specifically, the percentage difference between outcomes using seasonal and monthly parameters, for median monthly solar irradiation outcomes is always less than 5%, with an average difference of +2.1%. For yearly and monthly parameters, the difference is always less than 10%, averaging +3.66%.

When examining yearly solar irradiation, the differences in median values also remain minimal. The percentage difference between seasonal and monthly parameters averages +0.3%, while the difference between yearly and monthly parameters averages +2.0%. These observations, detailed in Section 4.3.2 -, underscore the importance of using median values for a more accurate and consistent assessment of solar irradiation outcomes.

Chapter 5 - Conclusion and Future Developments

Based on the findings of this study, several key insights have emerged, highlighting the complexities and differences in solar radiation analysis and its application in urban environments.

The research utilized a GIS-based approach to estimate solar radiation on an urban scale and evaluate the capabilities of GIS tools. As mentioned by Anselmo and Ferrara [41], due to the common use of tools embedded in QGIS and ArcGIS for solar radiation estimation, this study aimed to choose between the r.sun.insoltime tool in QGIS and the ASR tool in ArcGIS Pro. The ASR tool offers notable flexibility with customizable viewshed algorithms and diffuse model types, catering to diverse analytical needs. In contrast, the r.sun.insoltime tool is particularly adept for large-scale assessments due to its efficient processing of slope and orientation maps, allowing it to work faster than ArcGIS. Additionally, QGIS uses raster inputs for factors such as the Linke turbidity (T_L) factor and DG, enhancing the accuracy of solar radiation distribution evaluations. By using the same parameters for both tools and comparing the results, the study found that the trend correlation of the parameters and outcomes in r.sun.insoltime was more logically expected, making it the chosen tool for this study [Section 3.1 -].

Regarding the first objective, which aimed to identify the best input parameters for solar radiation estimation in the urban area of Turin, data were collected from trusted sources. These included an accurate DSM file with a resolution of 0.5m provided by the SDG11 Lab, monthly T_L factor values from seven sources, monthly DG ratio values from four sources, and Global Horizontal Irradiance (GHI) from one source. The complexity of solar radiation modeling underscores the necessity of considering multiple data sources in solar energy assessments and climate studies, crucial for accurate solar energy production and environmental monitoring in the region
A general trend was observed where winter months exhibited lower T_L values compared to summer months. However, the DG ratio values did not show a recognizable trend. The monthly data were then aggregated into seasonal intervals—winter (November to February), summer (May to August), spring/autumn (September, October, March, and April)—and yearly periods, showing the average value across all months [Section 4.2 -].

For the second objective, the collected data were organized into a series of plans as input parameters to be tested. The parameters were sorted in ascending order by DG ratio and then by T_L factor, resulting in 28 distinct plans for each temporal category (monthly, seasonal, and yearly), totaling 84 plans [Section 4.3.1 -].
Each plan produced 12 monthly values, totaling 1008 monthly outcomes. By aggregating the monthly outcomes, yearly solar radiation estimation was provided. A general pattern emerged where an increase in the T_L factor and the DG ratio led to a decrease in estimated solar radiation, and shifted the trend line downward. Yearly results for the four buildings under study showed that using yearly and seasonal parameters as inputs provided higher median solar radiation estimations compared to monthly parameters, with yearly parameters showing +0.30% and seasonal parameters showing +0.28% higher median outcomes. Comparing plan 01 and plan 28, which included the lowest and highest values for DG ratio and T_L factor respectively, plan 01 provided +34.4% higher outcomes on average. Building 2 consistently showed the highest solar irradiation, highlighting the importance of building orientation [Section 4.3.2 -].
Monthly solar radiation estimation results demonstrated that solar radiation received by the buildings increased from January, peaked in the summer months, and decreased until December. Similar to yearly

results, the monthly outcomes showed a decreasing trend from plan 01 to plan 28. Median values were considered the best representation of the outcomes due to potential obstructions and shadows on rooftops.
Moreover, observed trends in solar radiation levels across different months aligned with seasonal variations, informing decision-making processes related to solar energy production and environmental monitoring. The analyses revealed that variations in solar irradiation levels across different plans emphasized the importance of selecting appropriate input parameters for accurate estimation. This consistency highlighted the influence of geographical and architectural factors on solar irradiation outcomes, indicating how different buildings can have optimal months for solar energy collection due to their unique orientations, designs, or surrounding environmental factors [Section 4.3.3 -].

Following the third objective, Python programming was used to automate the procedure. The Graphical Modeler tool in QGIS was utilized due to its easy and understandable interface, creating three models for solar radiation estimation with monthly, seasonal, and yearly parameters. These models used digital elevation data and building-specific information to generate monthly median, maximum, and minimum solar radiation values [Section 4.4 -].

Overall, while using monthly values could generate more accurate results, the significant discovery is that using aggregated seasonal values as the input configuration offers the best trade-off between efficiency and precision. This approach simplifies the model—requiring only a quarter of the parameters needed for monthly inputs—while maintaining a high level of precision, with an average overestimation of +0.16% for yearly solar radiation estimation and +2.1% for monthly solar radiation estimation for the four buildings under study [Section 4.5 -].

Regarding automation, QGIS provides the Python script of the automated procedure, making it possible to use available data from online sources or real-time data from sensors or measuring instruments. Methods to extract data from online sources include using APIs, such as the PVGIS API, which allows for direct access to solar radiation data by specifying parameters like location, time range, and panel orientation. These parameters could be defined in a suitable format to be used for the automated algorithm, preparing real-time solar irradiation data in an urban context.

Future studies should examine daily variations to better understand and improve solar energy system sizing. Increasing the temporal resolution of the analysis is also crucial. Instead of just using aggregated values, examining monthly and daily productivity variations will provide more accurate data for defining the size of solar energy systems. Accurate albedo estimation should be incorporated into future research to account for the reflectance of urban surfaces. This would allow for more precise calculations of global solar radiation, especially in areas with reflective materials.

Additionally, exploring the differences in solar radiation estimates when using coarser Digital Surface Models (DSMs) with ground sampling distances of 1m or 5m compared to finer resolutions will help determine the optimal DSM resolution for accurate assessments. Extracting roof pitches from LiDAR point clouds or DSMs could also enhance the accuracy of solar potential estimation. This would help identify buildings with optimal orientations for solar energy production. Future research should focus on simulation accuracy by comparing the optimized simulation methodology with real-world data, acquiring data from existing systems or installing dedicated panels for validation.

Lastly, integrating three-dimensional data on roof pitches into the calculation model could improve the estimation of photovoltaic (PV) potential, going beyond the standard area calculation used in the current

study. Moreover, using Artificial Intelligence (AI) and Machine Learning (ML) algorithms, it would be possible to provide future scenarios of solar irradiation. AI and ML can analyze historical solar radiation data, weather patterns, and other relevant factors to predict future solar radiation levels more accurately. By addressing these areas, future research can improve the precision, accuracy, and applicability of solar radiation estimation models, contributing to more efficient and effective solar energy production and environmental monitoring.

Chapter 6 - Bibliography

[1] U. Leopold, C. Braun and P. Pinheiro, "An interoperable digital twin to simulate Spatio-temporal photovoltaic power output and grid congestion at neighbourhood and city levels in Luxembourg," *The International Archives of the Photogrammetry, Remote Sensing and Spatial Information Sciences,* Vols. XLVIII-4/W7-2023, pp. 95-100, 26 June 2023.

[2] Council of the European Union, "Council Directive 93/76/EEC of 13 September 1993 to limit carbon dioxide emissions by improving energy efficiency (SAVE)," *Official Journal of European Communities,* vol. L 237, pp. 28-30, 13 September 1993.

[3] European Commission, "The European Green Deal," European Commission, Brussels, 2019.

[4] European Parliament, "Directive 2010/31/EU of the European Parliament and of the Council of 19 May 2010 on the energy performance of buildings (recast)," *Official Journal of the European Union,* vol. L 153, pp. 13-35, 18 June 2010.

[5] European Parliament, "Directive 2012/27/EU of the European Parliament and of the Council of 25 October 2012 on energy efficiency, amending Directives 2009/125/EC and 2010/30/EU and repealing Directives 2004/8/EC and 2006/32/EC Text with EEA relevance," *Official Journal of the European Union,* vol. L 315, pp. 1-56, 14 November 2012.

[6] United Nations, "Global impact of war in Ukraine: Energy crisis," UN Global Crisis Response Group on Food, Energy and Finance, 02 August 2022. [Online]. Available: https://news.un.org/pages/wp-content/uploads/2022/08/GCRG_3rd-Brief_Aug3_2022_FINAL.pdf. [Accessed 28 October 2023].

[7] J. K. Kazak, J. Chodkowska-Miszczuk, G. Chrobak, M. Mrówczyńska and S. Martinát, "Renewable energy creditors versus renewable energy debtors: Seeking a pattern in a sustainable energy transition during the climate crisis," *The Anthropocene Review,* vol. 10, no. 3, p. 750–770, 13 January 2023.

[8] European Commission, "REPowerEU Plan," European Commission, Brussels, 2022.

[9] European Commission, "EU Solar Energy Strategy," European Commission, Brussels, 2022.

[10] European Parliament, "Amending Directive (EU) 2018/2001, Regulation (EU) 2018/1999 and Directive 98/70/EC as regards the promotion of energy from renewable sources, and repealing Council Directive (EU) 2015/652," *Official Journal of the European Union,* vol. L, pp. 1-77, 2023.

[11] Directorate-General for Energy, "European Green Deal: Energy Efficiency Directive adopted, helping make the EU 'Fit for 55'," 25 July 2023. [Online]. Available: https://energy.ec.europa.eu/news/european-green-deal-energy-efficiency-directive-adopted-helping-make-eu-fit-55-2023-07-25_en#:~:text=The%20recast%20directive%20further%20strengthens,public%20sector%20as%20a%20whole.. [Accessed 16 May 2024].

[12] European Parliament, "Directive 2009/28/EC of the European and of the Council of 23 April 2009 on the promotion of the use of energy from renewable sources and amending and subsequently repealing Directives 2001/77/EC and 2003/30/EC," *Official Journal of the European Union,* vol. L 140, pp. 16-62, 23 April 2009.

[13] European Commission, "Communication from the Commission to the European Parliament, the Council, the European Economic and Social Committee and the Committee of the Regions," European Commission, Brussels, 2022.

[14] European Commission, "Proposal for a DIRECTIVE OF THE EUROPEAN PARLIAMENT AND OF THE COUNCIL on the energy performance of buildings (recast)," European Commission, Brussels, 2021.

[15] European Parliament, "Directive 2009/29/EC of the European parliament and of the council of 23 April 2009 amending directive 2003/87/EC so as to improve and extend the greenhouse gas emission allowance trading scheme of the community," *Official Journal of the European Union,* vol. L 140, pp. 63-87, 2009.

[16] European Commission, "2030 Climate Target Plan," European Commission, Brussels, 2020.

[17] United Nations, "Transforming our world: the 2030 Agenda for Sustainable Development," United Nations, 2015.

[18] P. D'Orazio and P. Löwenstein, "Mobilising investments in renewable energy in Germany: which role for public investment banks?," *Journal of Sustainable Finance & Investment,* vol. 12, no. 2, pp. 451-474 , 17 June 2020.

[19] M. R. Di Nucci and A. Prontera, "The Italian energy transition in a multilevel system: between reinforcing dynamics and institutional constraints," *Zeitschrift für Politikwissenschaft,* vol. 33, no. 2, pp. 181-204, 23 December 2021.

[20] L. Esposito and G. Romagnoli, "Overview of policy and market dynamics for the deployment of renewable energy sources in Italy: Current status and future prospects," *Heliyon,* vol. 9, no. 7, p. e17406, 26 June 2023.

[21] European Commission, "European Commission," 2023. [Online]. Available: https://eu-mayors.ec.europa.eu/en/action_plan_list. [Accessed 16 February 2024].

[22] Y. Zhou, D. Wilmink, M. Zeman, O. Isabella and H. Ziar, "A geographic information system-based large scale visibility assessment tool for multi-criteria photovoltaic planning on urban building roofs," *Renewable and Sustainable Energy Reviews,* vol. 188, p. 113885, December 2023.

[23] Environmental Systems Research Institute, "Understanding GIS--The Arc/Info method," Environmental Systems Research INC., Redlands, CA, 1992.

[24] X. Liao, R. Zhu, M. S. Wong, J. Heo, P. W. Chan and C. Y. T. Kwok, "Fast and accurate estimation of solar irradiation on building rooftops in Hong Kong: A machine learning-based parameterization approach," *Renewable Energy,* vol. 216, p. 119034, 2023.

[25] M. Massano, E. Macii, A. Lanzini, E. Patti and L. Bottaccioli, "A GIS Open-Data Co-Simulation Platform for Photovoltaic Integration in Residential Urban Areas," *Engineering,* vol. 26, pp. 198-213, July 2023.

[26] G. Mutani, A. Vodano and M. Pastorelli, "Photovoltaic solar systems for smart bus shelters in the urban environment of turin (Italy)," in *International Telecommunications Energy Conference (INTELEC)*, Broadbeach, QLD, Australia, 2017.

[27] K. Mainzer , S. Killinger, R. McKenna and W. Fichtner, "Assessment of rooftop photovoltaic potentials at the urban level using publicly available geodata and image recognition techniques," *Solar Energy,* vol. 155, pp. 561-573, 2017.

[28] G. H. Brundtland, "Report of the World Commission on Environment and Development: Our Common Future," United Nations, Oslo, 1987.

[29] K. Khan and C. w. Su, "Does technology innovation complement the renewable energy transition?," *Environmental Science and Pollution Research,* vol. 30, no. 2023, p. 30144–30154, 24 November 2022.

[30] J.-B. Geng and Q. Ji, "Technological innovation and renewable energy development: evidence based on patent counts," *International Journal of Global Environmental,* vol. 15, no. 3, pp. 217-234, 2016.

[31] Z.-X. He, S.-C. Xu, Q.-B. Li and B. Zhao, "Factors that influence renewable energy technological innovation in China: A dynamic panel approach," *Sustainability ,* vol. 10, no. 1, p. 124, 2018.

[32] P. Kristoffer, L. Robert and P. Sö, "The innovation effects of renewable energy policies and their interaction: the case of solar photovoltaics," *Environmental Economics and Policy Studies,* vol. 21, pp. 217-254, 2019.

[33] A. Shivakumar, A. Dobbins, U. Fahl and A. Singh, "Drivers of renewable energy deployment in the EU: An analysis of past trends and projections," *Energy Strategy Reviews,* vol. 26, p. 100402, 2019.

[34] F. Xie, Y. Liu, F. Guan and N. Wang, "How to coordinate the relationship between renewable energy consumption and green economic development: from the perspective of technological advancement," *Environmental Sciences Europe,* vol. 32, pp. 1-15, 2020.

[35] C.-W. Su, K. Khan, M. Umar and W. Zhang, "Does renewable energy redefine geopolitical risks?," *Energy Policy,* vol. 158, p. 112566, 2021.

[36] M. S. Salvarli and H. Salvarli, "For sustainable development: Future trends in renewable energy and enabling technologies," in *Renewable energy-resources, challenges and applications*, M. Al Qubeissi, A. El-kharouf and H. S. Soyhan, Eds., London, IntechOpen, 2020, pp. 3-17.

[37] Z. Liu, X. Liu, H. Zhang and . D. Yan, "Integrated physical approach to assessing urban-scale building photovoltaic potential at high spatiotemporal resolution," *Journal of Cleaner Production,* vol. 388, p. 135979, 2023.

[38] S. Freitas , C. Catita, P. Redweik and M. C. Brito, "Modelling solar potential in the urban environment: State-of-the-art review," *Renewable and Sustainable Energy Reviews,* vol. 41, pp. 915-931, 2015.

[39] M. Horváth, D. Kassai-Szoó and T. Csoknyai, "Solar energy potential of roofs on urban level based on building typology," *Energy and Buildings,* vol. 111, pp. 278-289, 2016.

[40] L. R. Rodríguez, E. Duminil, J. S. Ramos and U. Eicker, "Assessment of the photovoltaic potential at urban level based on 3D city models: A case study and new methodological approach," *Solar Energy,* vol. 146, pp. 264-275, 2017.

[41] S. Anselmo and M. Ferrara, "Trends and Evolution of the GIS-Based Photovoltaic Potential Calculation," *Energies,* vol. 16, no. 23, p. 7760, 24 November 2023.

[42] E. Negri, L. Fumagalli and M. Macchi, "A review of the roles of digital twin in CPS-based production systems," *Procedia manufacturing,* vol. 11, pp. 939-948, 2017.

[43] M. Shafto, M. Conroy, R. Doyle, E. Glaessgen, C. Kemp, J. LeMoigne and L. Wang, "Draft modeling, simulation, information technology & processing roadmap," *Technology area,* vol. 11, pp. 1-32, 2010.

[44] A. Sharma, E. Kosasih, J. Zhang, A. Brintrup and A. Calinescu, "Digital Twins: State of the art theory and practice, challenges, and open research questions," *Journal of Industrial Information Integration,* vol. 30, p. 100383, 2022.

[45] J. Lee, E. Lapira, B. Bagheri and H.-a. Kao, "Recent advances and trends in predictive manufacturing systems in big data environment," *Manufacturing letters,* vol. 1, no. 1, pp. 38-41, 2013.

[46] W. Yu, P. Patros, B. Young, E. Klinac and T. G. Walmsley, "Energy digital twin technology for industrial energy management: Classification, challenges and future," *Renewable and Sustainable Energy Reviews,* vol. 161, p. 112407, 2022.

[47] M. Grieves, "Digital Twin: Manufacturing Excellence through Virtual Factory Replication," *White paper,* vol. 1, pp. 1-7, 2014.

[48] F. Tao, B. Xiao, Q. Qi, J. Cheng and P. Ji, "Digital twin modeling," *Journal of Manufacturing Systems,* vol. 64, pp. 372-389, 2022.

[49] I. Jeddoub, G.-A. Nys and R. Billen, "Digital Twins for cities: Analyzing the gap between concepts and current implementations with a specific focus on data integration," *International Journal of Applied Earth Observation and Geoinformation,* vol. 122, p. 103440, 2023.

[50] E. Glaessgen and D. Stargel, "The Digital Twin Paradigm for Future NASA and U.S. Air Force Vehicles," in *53rd AIAA/ASME/ASCE/AHS/ASC Structures, Structural Dynamics and Materials Conference*, Honolulu, Hawaii, 2012.

[51] C. Ghenai, L. A. Husein, M. Al Nahlawi, A. K. Hamid and M. Bettayeb, "Recent trends of digital twin technologies in the energy sector: A comprehensive review," *Sustainable Energy Technologies and Assessments,* vol. 54, no. December, p. 102837, 2022.

[52] Y.-Y. Hong and R. A. Pula, "Diagnosis of PV faults using digital twin and convolutional mixer with LoRa notification system," *Energy Reports,* vol. 9, pp. 1963-1976, December 2023.

[53] M. Charitonidou, "Urban scale digital twins in data-driven society: Challenging digital universalism in urban planning decision-making," *International Journal of Architectural Computing,* vol. 20, no. 2, pp. 238-253, 10 January 2022.

[54] A. Francisco, N. Mohammadi and J. E. Taylor, "Smart City Digital Twin–Enabled Energy Management: Toward Real-Time Urban Building Energy Benchmarking," *Journal of Management in Engineering,* vol. 36, no. 2, pp. 1-11, 2019.

[55] X. Pan, D. Mavrokapnidis, H. T. Ly, N. Mohammadi and J. E. Taylor, "Assessing and Forecasting Collective Urban Heat Exposure with Smart City Digital Twins," *Scientific Report,* vol. 14, no. 9653, pp. 1-14, 2024.

[56] F. F. Ahmad, C. Ghenai and M. Bettayeb, "Maximum power point tracking and photovoltaic energy harvesting for Internet of Things: A comprehensive review," *Sustainable Energy Technol Assess,* vol. 47, p. 101430, 2021.

[57] M. Singh, J. Jiao, M. Klobasa and R. Frietsch, "Making Energy-transition headway: A Data driven assessment of German energy startups," *Sustainable Energy Technologies and Assessments,* vol. 47, p. 101322, 2021.

[58] S. I. Kaitouni, J. Pfafferott, A. Jamil, M. Ahachad and J. Brigui, "A holistic digital workflow methodology to shifting towards net zero energy urban residential buildings in a semi-arid climate," *Solar Energy,* vol. 263, p. 111959, 2023.

[59] S. I. Kaitouni, I. A. Abdelmoula, N. Es-sakali, M. O. Mghazli, H. Er-retby, Z. Zoubir, F. El Mansouri, M. Ahachad and J. Brigui, "Implementing a Digital Twin-based fault detection and diagnosis approach for optimal operation and maintenance of urban distributed solar photovoltaics," *Renewable Energy Focus,* vol. 48, p. 100530, 2024.

[60] L. Lüer, I. M. Peters, A. S. Smith, E. Dorschky, B. M. Eskofier, F. Liers, M. Sjarov, M. Brossog, D. M. Guldi, A. Maier and C. J. Brabec, ""A digital twin to overcome long-time challenges in photovoltaics.," *Joule,* vol. 8, no. 2, pp. 295-311, 2024.

[61] J. Yu, Z. Wang, A. Majumdar and R. Rajagopal, "DeepSolar: A Machine Learning Framework to Efficiently Construct a Solar Deployment Database in the United States," *Joule,* vol. 2, no. 12, p. 10.1016/j.joule.2018.11.021, 2018.

[62] W. Hu, K. Bradbury, J. M. Malof, B. Li, B. Huang, A. Streltsov, K. S. Fujita and B. Hoen, "What you get is not always what you see—pitfalls in solar array assessment using overhead imagery," *Applied Energy,* vol. 327, p. 120143, 2022.

[63] Z. Wang, Z. Wang, A. Majumdar and R. Rajagopal, "Identify Solar Panels in Low Resolution Satellite Imagery with Siamese Architecture and Cross-Correlation," in *33rd Conference on Neural Information Processing Systems (NeurIPS 2019),* , Vancouver, Canada, 2019.

[64] S. Salamanca, P. Merchán and I. García, "On the detection of solar panels by image processing techniques," in *25th Mediterranean Conference on Control and Automation (MED)*, Valletta, Malta, 2017.

[65] B. B. Kausika, D. Nijmeijer, I. Reimerink, P. Brouwer and V. Liem, "GeoAI for detection of solar photovoltaic installations in the Netherlands," *Energy and AI,* vol. 6, no. December, p. 100111, 2021.

[66] A. Cardoso, D. Jurado-Rodríguez, A. López, M. I. Ramos and J. M. Jurado, "Automated detection and tracking of photovoltaic modules from 3D remote sensing data," *Applied Energy,* vol. 367, no. August, p. 123242, 2024.

[67] R. Rotar, N. Vârtaci, M. Bălaș, F. Oprițoiu and M. Vlăduțiu, "Digital Twin Architecture for an Automated PV System with Self-Testing Capabilities," in *29 th International Symposium for Design and Technology in Electronic Packaging (SIITME)*, Craiova, Romania, 2023.

[68] International Energy Agence (IEA), "Energy and Climate Change - World Energy Outlook Special Report," IEA Publications, Paris, 2015.

[69] International Energy Agency (IEA), "Next Generation Wind and Solar Power From Cost to Value," IEA Publications, Paris, 2016.

[70] J. L. Sawin, F. Sverrisson, K. Seyboth, R. Adib, H. E. Murdock, C. Lins, I. Edwards, M. Hullin, L. H. Nguyen, S. S. Prillianto, K. Satzinger, F. Appavou, A. Brown, I. Chernyakhovskiy, J. Logan, M. Milligan, O. Zinaman, B. Epp, L. Huber, L. Lyons, T. Nowak, P. Otte, J. Skeen, B. Sovacool, B. Witkamp, E. Musolino, A. Brown, L. E. Williamson, L. Ashworth and L. Mastny, "Renewables 2017 Global Status Report," International Nuclear Information System (INIS) Publications, Paris, 2017.

[71] A. A. A. Gassar and S. H. Cha, "Review of geographic information systems-based rooftop solar photovoltaic potential estimation approaches at urban scales," *Applied Energy,* vol. 291, p. 116817, 1 June 2021.

[72] N. D. Jackson and T. Gunda, "Evaluation of extreme weather impacts on utility-scale photovoltaic plant performance in the United States," *Applied Energy,* vol. 302, p. 117508, 15 November 2021.

[73] A. Walch, R. Castello, N. Mohajeri and J.-L. Scartezzini, "Big data mining for the estimation of hourly rooftop photovoltaic potential and its uncertainty," *Applied Energy,* vol. 262, no. March, p. 114404, 2020.

[74] F. Antonanzas-Torres, R. Urraca, J. Polo, O. Perpiñán-Lamigueiro and R. Escobar, "Clear sky solar irradiance models: A review of seventy models," *Renewable and Sustainable Energy Reviews,* vol. 107, no. June, pp. 374-387, 2019.

[75] M. B. d. Souza, É. A. Tonolo, R. L. Yang, G. M. Tiepolo and J. U. Junior, "Determination of Diffused Irradiation from Horizontal Global Irradiation - Study for the City of Curitiba," *Brazilian Archives of Biology and Technology,* vol. 62, p. e19190014, 2019.

[76] L. k. Kumar, A. K. Skidmore and E. Knowles, "Modelling topographic variation in solar radiation in a GIS environment," *International Journal of Geographical Information Science,* vol. 11, no. 5, pp. 475-497, 1997.

[77] C. Ratti and P. Richens, "Raster Analysis of Urban Form," *Environment and Planning B: Planning and Design,* vol. 31, no. 2, pp. 297-309, 2004.

[78] J. Hofierka and M. Šúri, "The solar radiation model for Open source GIS: implementation and applications," in *Open source GIS-GRASS users conference*, Trento, Italy, 2002.

[79] F. Lindberg, C. Grimmond, A. Gabey, B. Huang, C. W. Kent, T. Sun, N. E. Theeuwes, L. Jarvi, H. C. Ward, I. Capel-Timms, Y. Chang, P. Jonsson, N. Krave, D. Liu, D. Meyer, K. F. G. Olofson, J. Tan, D. Wastberg, L. Xue and Z. Zhang, "Urban Multi-scale Environmental Predictor (UMEP): An integrated tool for city-based climate services," *Environmental Modelling & Software,* vol. 99, pp. 70-87, 2018.

[80] J. G. Corripio, "Package 'insol' (version 1.1.1)," 2015.

[81] P. Fu and P. M. Rich, "Design and implementation of the Solar Analyst: an ArcView extension for modeling solar radiation at landscape scales," in *Nineteenth annual ESRI user conference*, San Diego, USA, 1999.

[82] M. Dorman, E. Erell, A. Vulkan and I. Kloog, "shadow: R Package for Geometric Shadow Calculations in an Urban Environment," *The R Journal,* vol. 11, no. 01, pp. 1-22, 2019.

[83] M. Haklay and P. Weber, "OpenStreetMap: User-Generated Street Maps," *IEEE Pervasive Computing,* vol. 7, no. 4, pp. 12-18, 2008.

[84] G. Gröger and L. Plümer, "CityGML – Interoperable semantic 3D city models," *ISPRS Journal of Photogrammetry and Remote Sensing,* vol. 71, pp. 12-33, July 2012.

[85] F. Biljecki, H. Ledoux and J. Stoter, "An improved LOD specification for 3D building models," *Computers, Environment and Urban Systems,* vol. 59, pp. 25-37, September 2016.

[86] J. Amanatides and A. Woo, "A fast voxel traversal algorithm for ray tracing," *Eurographics,* vol. 87, no. 3, pp. 3-10, 1987.

[87] R. P. Gupta, "Digital Elevation Model (Chapter 8)," in *Remote Sensing Geology*, Berlin, Springer, 2017, p. 101–106.

[88] Q. Zhou, "Digital elevation model and digital surface model," *International Encyclopedia of Geography: People, the Earth, Environment and Technology,* pp. 1-17, 2017.

[89] Z. Li, C. Zhu and C. Gold, Digital terrain modeling: principles and methodology, CRC Press ed., Boca Raton: Taylor & Francis Group, 2004.

[90] L. Croneborg, K. Saito, M. Matera, D. McKeown and J. v. Aardt, DIGITAL ELEVATION MODELSA - Guidance Note on how Digital Elevation Models are created and used – includes key definitions, sample Termsof Reference and how best to plan a DEM-mission, NW Washington: International Bank for Reconstruction and Development, 2015.

[91] P. A. Burrough and R. A. McDonnell, Principles of Geographical Information Systems., First ed., OXford: Oxford University Press, 1998.

[92] J. A. Thompson, J. C. Bell and C. A. Butler, "Digital elevation model resolution: effects on terrain attribute calculation and quantitative soil-landscape modeling," *Geoderma,* vol. 100, no. 1-2, pp. 67-89, 2001.

[93] J. C. Guarneri and R. C. Weih Jr., "Comparing Methods for Interpolation to Improve Raster Digital Elevation Models," *Journal of the Arkansas Academy of Science,* vol. 66, no. Article 16, pp. 77-81, 2012.

[94] M. Over, "File:DTM DSM.png," 21 January 2011. [Online]. Available: https://commons.wikimedia.org/wiki/File:DTM_DSM.png. [Accessed 16 March 2024].

[95] V. Adjiski and D. Serafimovski, "GIS- and AHP-based Decision Systems for Evaluating Optimal Locations of Photovoltaic Power Plants: Case Study of Republic of North Macedonia," *Geomatics and Environmental Engineering,* vol. 18, no. 1, pp. 51-82, 19 January 2024.

[96] K. Zakšek, T. Podobnikar and K. Oštir, "Solar radiation modelling," *Computers & Geosciences,* vol. 31, no. 2, pp. 233-240, 2005.

[97] J. Kleissl , Solar energy forecasting and resource assessment, San Diego, California: Academic Press, 2013.

[98] J. A. Duffie and W. A. Beckman, Solar engineering of thermal processes, Hoboken, New Jersey : John Wiley & Sons, 2013.

[99] S. Milan, "KuaFu: exploring the Sun—Earth connection," *Astronomy & Geophysics,* vol. 53, no. 4, p. 4.21–4.24, 2012.

[100] M. Šúri and J. Hofierka, "A new GIS-based solar radiation model and its application to photovoltaic assessments," *Transactions in GIS,* vol. 8, no. 2, pp. 175-190, 2004.

[101] J. Mikulović and Ž. Đurišić, "Models for the Calculation of Diffuse Radiation on Solar Collectors," *International Journal of Electrical Engineering and Computing,* vol. 4, no. 1, pp. 10-17, 2020.

[102] J. Fan, L. Wu, F. Zhang, H. Cai, X. Ma and H. Bai, "Evaluation and development of empirical models for estimating daily and monthly mean daily diffuse horizontal solar radiation for different climatic regions of China," *Renewable and Sustainable Energy Reviews,* vol. 105, pp. 168-186, 2019.

[103] T. Muneer, "Solar radiation model for Europe," *Building Services Engineering Research and Technology,* vol. 11, no. 4, pp. 153-163, 1990.

[104] Joint Research Centre (JRC) Team, "PVGIS data sources & calculation methods," 23 July 2014. [Online]. Available: https://joint-research-centre.ec.europa.eu/photovoltaic-geographical-information-system-pvgis/getting-started-pvgis/pvgis-data-sources-calculation-methods_en. [Accessed 10 November 2023].

[105] Clean Power Research L.L.C., "SolarAnywhere," 2021. [Online]. Available: https://www.solaranywhere.com/support/data-fields/definitions/. [Accessed 06 June 2024].

[106] WMO (World Meteorological Organization), "Meteorological aspects of the utilization of solar radiation as an energy source," WMO-No. 557, Geneva, Switzerland, 1981.

[107] F. Kasten, "Linke turbidity factor based on improved values of the integral Rayleigh optical thickness," *Solar Energy,* vol. 56, p. 239–244, 1996.

[108] L. Diabate, J. Remund and L. Wald, "Linke turbidity factors for several sites in Africa," *Solar Energy,* vol. 75, no. 2, pp. 111-119, 2003.

[109] M. Chaâbane, M. Masmoudi and K. Medhioub, "Determination of Linke turbidity factor from solar radiation measurement in northern Tunisia," *Renewable Energy,* vol. 29, no. 13, pp. 2065-2076, 2004.

[110] J. A. Coakley, "Reflectance and albedo, surface," *Encyclopedia of atmospheric sciences,* pp. 1914-1923, 2003.

[111] Q. Wang, Y. Chen, T. Fung, Z. Li, Y. Huang, M. M. F. Wong and X. Lu, "Effect of land surface parameters on meteorology and ozone air quality simulations in the Great Bay Area, China," *Atmospheric Environment,* vol. 315, p. 120146, 15 December 2023.

[112] M. A. D. G. A. M. G. M. F. B. C. A. N. a. F. R. Cardinali, "Glass beads retro-reflective coating for building application: albedo assessment in urban canyon configurations," in *38th UIT Heat Transfer International Conference (UIT 2021)*, Gaeta, Italy, 2022.

[113] S. Konopacki, H. Akbari, M. Pomerantz, S. Gabersek and L. Gartland, "Cooling energy savings potential of light-colored roofs for residential and commercial buildings in 11 US metropolitan areas," Lawrence Berkeley National Lab. (LBNL), Berkeley, CA, 1997.

[114] US EPA (US Environmental Protection Agency), Cooling Our Communities a Guidebook On Tree Planting And Light-colored Surfacing, H. Akbari, S. Davis, S. Dorsano, J. Huang and S. Winnett, Eds., Washington, D.C.: Lawrence Berkeley Lab., 1992.

[115] P. Ziemba and M. Szaja, "Fuzzy Decision-Making Model for Solar Photovoltaic Panel Evaluation," *Energies,* vol. 16, no. 13, p. 5161, July 2023.

[116] H. Zou, G. Dai, A. C. Wang, X. Li, S. L. Zhang, W. Ding, L. Zhang, Y. Zhang and Z. L. Wang, "Alternating Current Photovoltaic Effect," *Advanced Materials,* vol. 32, no. 11, p. 1907249, 2020.

[117] M. Rahman, M. Hasanuzzaman and N. Rahim, "Effects of various parameters on PV-module power and efficiency," *Energy Conversion and Management,* vol. 103, pp. 348-358, 2015.

[118] P. Gagnon, R. Margolis, J. Melius, C. Phillips and R. Elmore, "Rooftop Solar Photovoltaic Technical Potential in the United States. A Detailed Assessment," National Renewable Energy Laboratory (NREL), Golden, 2016.

[119] P. Denholm and R. Margolis, "Supply Curves for Rooftop Solar PV-Generated Electricity for the United States," National Renewable Energy Laboratory (NREL), Golden, 2008.

[120] C. Campoverde, M. Koeva, C. Persello, K. Maslov, W. Jiao and D. Petrova-Antonova, "Automatic Building Roof Plane Extraction in Urban Environments for 3D City Modelling Using Remote Sensing Data," *Remote Sensing,* vol. 16, no. 8, p. 1389, 14 April 2024.

[121] A. M. Martín, J. Domínguez and J. Amador, "Applying LIDAR datasets and GIS based model to evaluate solar potential over roofs: a review." 3, no. 3 (2015).," *AIMS Energy,* vol. 3, no. 3, pp. 326-343, 2015.

[122] R. Singh and R. Banerjee, "Estimation of rooftop solar photovoltaic potential of a city," *Solar Energy,* vol. 115, pp. 589-602, 2015.

[123] J. A. Jakubiec and C. F. Reinhart, "A method for predicting city-wide electricity gains from photovoltaic panels based on LiDAR and GIS data combined with hourly Daysim simulations," *Solar Energy,* vol. 93, pp. 127-143, 2013.

[124] Y. Huang, Z. Chen, B. Wu, L. Chen, W. Mao, F. Zhao, J. Wu, J. Wu and B. Yu, "Estimating Roof Solar Energy Potential in the Downtown Area Using a GPU-Accelerated Solar Radiation Model and Airborne LiDAR Data," *Remote Sensing,* vol. 7, no. 9, pp. 17212-17233, 2015.

[125] F. Vecchi and U. Berardi, "Solar analysis for an urban context from GIS to block-scale evaluations," *Energy Policy,* vol. 184, p. 113884, 2024.

[126] M. Neteler and H. Mitasova, Open source GIS: a GRASS GIS approach. Vol. 689. Springer Science & Business Media, 2002, 1 ed., New York, NY: Springer, 2004.

[127] K. Scharmer and J. Greif, The European Solar Radiation Atlas, 2 ed., Paris, France: Ecoles des Mines de Paris, 2000.

[128] S. L. Smith, D. A. Holland and P. A. Longley, "The effect of changing grid size in the creation of laser scanner digital surface models," in *7th International Conferenceon on GeoComputation*, Southampton, UK, 2003.

[129] F. Mancini, M. Dubbini, M. Gattelli, F. Stecchi, S. Fabbri and G. Gabbianelli, "Using unmanned aerial vehicles (UAV) for high-resolution reconstruction of topography: The structure from motion approach on coastal environments," *Remote sensing,* vol. 5, no. 12, pp. 6880-6898, 2013.

[130] F. Nex and F. Remondino, "UAV for 3D mapping applications: a review.","*Applied geomatics,* vol. 6, pp. 1-15, 2014.

[131] C. H. Hugenholtz, K. Whitehead, O. W. Brown, T. E. Barchyn, B. J. Moorman, A. LeClair, K. Riddell and T. Hamilton, "Geomorphological mapping with a small unmanned aircraft system (sUAS): Feature detection and accuracy assessment of a photogrammetrically-derived digital terrain model," *Geomorphology ,* vol. 194, pp. 16-24, 2013.

[132] European Commission, "PVGIS 5.2," 1 March 2022. [Online]. Available: https://joint-research-centre.ec.europa.eu/photovoltaic-geographical-information-system-pvgis/pvgis-releases/pvgis-52_en. [Accessed 10 May 2024].

[133] U. Pfeifroth, S. Kothe, R. Müller, J. Trentmann, R. Hollmann, P. Fuchs and M. Werscheck, "Surface Radiation Data Set - Heliosat (SARAH) - Edition 2," Satellite Application Facility on Climate Monitoring (CM SAF), 2017.

[134] European Commission, "SARAH-2 Solar Radiation Data," 2021. [Online]. Available: https://joint-research-centre.ec.europa.eu/photovoltaic-geographical-information-system-pvgis/pvgis-data-download/sarah-2-solar-radiation-data_en. [Accessed 24 May 2024].

[135] SoDa, "Solar Energy Services for Professionals," 2022. [Online]. Available: https://www.soda-pro.com/home. [Accessed 15 February 2024].

[136] SoDa, "HELIOCLIM," 2022. [Online]. Available: https://www.soda-pro.com/help/helioclim/introduction. [Accessed 25 May 2024].

[137] SoDa, "LINKE TURBIDITY (TL) FACTOR WORLDWIDE, 2010 TL maps and webservice," 2022. [Online]. Available: https://www.soda-pro.com/help/general-knowledge/linke-turbidity-factor. [Accessed 15 February 2024].

[138] J. Remund, S. Müller, M. Schmutz, D. Barsotti, P. Graf and R. Cattin, "Handbook part I: Software," in *Meteonorm 8 Irradiation data for every place on Earth*, vol. 8.2, Bern, Meteotest AG, 2023, pp. 1-81.

[139] J. Remund, S. Müller, M. Schmutz, D. Barsotti, P. Graf and R. Cattin, "Handbook part II: Theory," in *Meteonorm 8 Irradiation data for every place on Earth*, vol. 8.2, Bern, Meteotest AG, 2023, pp. 1-81.

[140] G. V. Fracastoro, Y. Yang, G. Coppa and M. Simonetti, "Atmospheric turbidity measurements in Torino: A comparison between 1975 and 2010," in *30th ISES Biennial Solar World Congress*, Kassel (Germany), 2011.

[141] J. Hofierka, M. Suri and T. Huld, "r.sun - Solar irradiance and irradiation model," 2007. [Online]. Available: https://grass.osgeo.org/grass83/manuals/r.sun.html. [Accessed 3 November 2023].

[142] S. A. Klein, "Calculation of monthly average insolation on tilted surfaces," *Solar Energy,* vol. 19, no. 4, pp. 325-329, 1977.

[143] SoDa, "LINKE TURBIDITY (TL) FACTOR WORLDWIDE, 2010 TL maps and webservice," 2022. [Online]. Available: https://www.soda-pro.com/help/general-knowledge/linke-turbidity-factor. [Accessed 15 February 2024].

[144] Y. A. Eltbaakh, M. Ruslan, M. Alghoul, M. Othman, K. Sopian and T. Razykov, "Solar attenuation by aerosols: An overview," *Renewable and Sustainable Energy Reviews,* vol. 16, no. 6, pp. 4264-4276, 2012.

[145] J. Remund, L. Wald, M. Lefèvre, T. Ranchin and J. H. Page, "Worldwide Linke turbidity information," in *ISES Solar World Congress*, Göteborg, Sweden, 2003.

[146] J. Page, "Radiation Data," in *Solar Energy Conversion II - Selected Lectures from the 1980 International Symposium on Solar Energy Utilization*, A. Janzen and R. Swartman, Eds., London, Ontario, Canada, 1981, p. 23–35.